Synthesis and Characterization of Multifunctional Metal Oxide Nanoparticles

Dissertation

Zur Erlangung des Grades
"Doktor der Naturwissenschaften"
im Promotionsfach Chemie

am Fachbereich Chemie, Pharmazie und Geowissenschaften
der Johannes Gutenberg-Universität, Mainz

Vorgelegt von:
Dorothea Gömpel
(geboren in Fulda)

JOHANNES GUTENBERG UNIVERSITÄT MAINZ

JG|U

Mainz, 2015

Dekan:	Prof. Dr. [redacted]
1. Berichtserstatter:	Prof. Dr. [redacted]
2. Berichtserstatter:	Prof. Dr. [redacted]
Tag der mündlichen Prüfung:	XX.XX.XXXX

Die vorliegende Arbeit wurde von Januar 2012 bis August 2015 unter Leitung von Herrn Prof. Dr. [redacted] am Institut für Anorganische und Analytische Chemie der Johannes Gutenberg-Universität Mainz erstellt.

Acknowledgements

First of all, I would like to thank my supervisor Prof. Dr. [redacted] for giving me the opportunity to work on an interesting research project and the freedom in my work.

I want to express my gratitude to Dr. [redacted] for his guidance and advice, proof reading and good ideas.

I would like to thank [redacted] for a peaceful cohabitation in one fumehood, measuring BET samples for me and proof reading my thesis.

Further, I want to thank [redacted] for the PXRD measurments and Dr. [redacted] for the RFA measurements as well as the helpful discussions and help concerning PXRD.

I want to acknowledge [redacted], Dr. [redacted] and Dr. [redacted] for the HRTEM and electron diffraction measurements.

Moreover, I would like to thank [redacted] and [redacted] for the catalytic measurements of the vanadium oxide nanoparticles.

I would like to thank [redacted] for the cytotoxicity-assays and cell staining experiments and Dr. [redacted] for the CT and MRI measurements.

Furthermore, many thanks to Dr. [redacted], who measured ICP-MS of the nanoparticles, as well as [redacted] and Dr. [redacted] for the zeta-potential measurements.

I also would like to thank Dr. [redacted] for his help with the Raman measurements. I am grateful for the XPS measurements performed by Dr. [redacted].

Furthermore, I want to thank the whole [redacted] research group for a pleasant work climate, interesting scientific discussions and fun time during coffee breaks, group outings, barbeques...

Thanks, Schwesterherz, for proof reading my dissertation and generally being you (most of the time).

Last but not least, I want to thank my family and my fiance [redacted] for their loving support during my studies and my thesis.

Abstract

This thesis is a contribution to the rapidly evolving area of research, manipulating materials at the nanoscale, called nanotechnology. It focuses on the design and synthesis of transition metal oxide nanoparticles and characterizing them using various methods involving like X-ray spectroscopy and microscopy. The interest in the synthesis of nanoparticles stems due to the fact that nanparticles show enhanced applications in various fields ranging from catalysis to nanomedicine because of their size dependent properties and their high surface-to-volume ratio. Several novel synthetic protocols for tantalum and vanadium oxide nanoparticles with different morphologies and compositions were developed. In addition, the influence of the reaction parameters like precursors concentrations, surfactants, solvent, temperature etc. on the morphology of the nanoparticles were investigated systematically.

In particular, a solvo-/hydrothermal method was established to get vanadium oxide nanoparticles with different morphologies ranging from rods, sheets to hierarchically structured urchin-like particles. The influence of the solvent on the nanoparticle morphology was thoroughly investigated. As vanadium is present in the active center of several enzymes including peroxidase, vanadium oxide nanoparticles were tested for their role as a peroxidase mimicking using 2,2´-azino-bis(3-ethylbenzothiazoline-6-sulphonic acid) (ABTS) as a substrate in the presence of H_2O_2. The catalytic activity was related to the surface area and structure of the nanoparticles. All investigated vanadium(IV) oxides showed peroxidase-like activity, however, whereas urchin-shaped nanoparticles had the highest activity due to their high surface area.

In addition, nanosized Ta_2O_5 rods and $MTaO_3$ cubes (M =Na, K, Rb) were synthesized hydrothermally especially exploring the influence of the pH on their morphology as well as on crystallinity. Low and neutral pH values favored rod-shaped tantalum oxide nanoparticles. High base concentrations resulted in cube-shaped tantalate nanoparticles with a pyrochlore structure. The pyrochlore structure is characterized by a tunnel structural motive that allowed a complete ion exchange of the alkali metal ions for H^+ while retaining their morphology. Those nanoparticles showed promising photocatalytic properties.

Furthermore, mesoporous materials are highly desirable with their high surface areas due to their porous structure. On this account, spherical mesoporous tantalum oxide (mTa_2O_5) nanoparticles with high surface areas and a narrow pore size distribution were synthesized using a template free approach utilizing self-assembly process. The heat treatment of the mTa_2O_5 allowed to expand the pores as well as to crystallize

the nanoparticles. Furthermore, palladium nanoparticles were grown onto the mTa_2O_5 in a sonochemical reaction. The palladium nanoparticles are linked to the surface of the mTa_2O_5 *via* amine groups exploiting the Pearson hardness matching. For amine functionalization the mTa_2O_5 surface was coated with an amine bearing silane, 3-aminopropyltriethoxysilane (APTES).
Tantalum oxide nanoparticles can also be employed as contrast agents for X-ray computed tomography. In order to expand the contrast enhancement to magnetic resonance imaging (MRI) the mTa_2O_5 nanoparticles were doped with varying concentrations of paramagnetic ions, namely Gd^{3+}. For biocompability and water solubility the mTa_2O_5:Gd nanoparticles were functionalized with methoxy(polyethyleneoxy)propyltrimethoxy silane PEG-TES and APTES whereas the latter enabled the introduction of further functionalities like dyes. It was confirmed that the mTa_2O_5:Gd can simultaneously act as MRI and CT contrast agents, whereby the best MRI contrast enhancement was realized for low Gd^{3+} percentages.

Zusammenfassung

Diese Dissertation ist ein Beitrag zum ständig wachsenden Forschungsgebiet Materialien auf Nanoebene zu beeinflussen, der Nanotechnik. Der Fokus liegt dabei auf dem Design und der Synthese von Übergangsmetalloxidnanopartikeln und deren Charakterisierung mit einer Vielzahl an Methoden wie Röntgendiffraktion und Mikroskopie. Das Interesse an Nanopartikeln basiert auf deren vielfältigen Anwendungsgebieten von der Katalyse bis zur Nanomedizin, aufgrund ihrer größenabhängigen Eigenschaften sowie des großen Oberflächen-zu-Volumen Verhältnisses. Mehrere neue Synthesevorschriften für Tantal- und Vanadiumoxidnanopartikel mit unterschiedlichen Morphologien und Zusammensetzungen wurden entwickelt. Darüber hinaus wurde der Einfluss verschiedener Reaktionsparameter wie Precursorkonzentrationen, Surfaktanten, Lösungsmittel, Temperatur usw. auf die Morphologie der Nanopartikel systematisch untersucht.
Im Speziellen wurde eine solvo-/hydrothermale Methode etabliert, die es erlaubt Vanadiumoxidnanopartikel unterschiedlicher Morphologie von Stäbchen und Plättchen bis zu hierarchisch strukturierten seeigelförmigen Partikeln zu erhalten. Der Einfluss des Lösungsmittels auf die Form wurde gründlich untersucht. Da Vanadium im aktiven Zentrum von Enzymen wie Peroxidasen verbreitet ist, wurde die Rolle der Vanadiumoxidnanopartikel als als Peroxidasemimetika mit 2,2´-Azino-bis(3-ethylbenzothiazolin-6-sulphonsäure) (ABTS) als Substrat in der Gegenwart von H_2O_2 getestet. Die katalytische Aktivität wurde mit der Oberfläche und Morphologie der Partikel in Verbindung

gesetzt. Es zeigte sich, dass alle untersuchten Vanadium(IV)oxide Peroxidasereaktionen katalysieren, wobei die seeigelförmigen Partikel die höchste Aktivität besitzen, da diese die größte Oberfläche haben.
Darüber hinaus wurden nanometergroße Ta_2O_5-Stäbchen und $MTaO_3$ (M=Na, K, Rb)-Würfel hydrothermal synthetisiert, wobei insbesondere der Einfluss des pH-Wertes auf die Morphologie sowie die Kristallinität untersucht wurde. Niedrige und neutrale pH-Werte führten zu stäbchenförmigen Tantaloxidnanopartikeln. Bei hohen Basenkonzentrationen wurden würfelförmige Tantalatnanopartikel mit einer Pyrochlorstruktur erhalten. Der Pyrochlor zeichnet sich durch eine tunnelförmiges Strukturmotiv aus, welches einen vollständigen Ionenaustausch von Alkalimetallionen durch H^+ unter Erhalt der Morphologie erlaubte. Die untersuchten Nanopartikel haben vielversprechende photokatalytische Eigenschaften.
Mesoporöse Materialien sind von großem Interesse, da sie aufgrund ihrer porenförmigen Struktur über eine große Oberfläche verfügen. Aus diesem Grund wurden kugelförmige mesoporöse Tantaloxidnanopartikel (mTa_2O_5) mit einer großen Oberfläche und einer engen Porengrößenverteilung templatfrei unter Ausnutzung eines Selbstorganisations (self-assembly)-Prozesses synthetisiert. Durch das Tempern der mTa_2O_5 Nanpartikel erweiterten sich deren Poren und die Nanopartikel kristallisierten. Anschließend wurden Palladiumnanopartikel mit einer Ultraschallsynthese auf den mTa_2O_5 angebracht. Dabei wurden die Palladiumnanopartikel über Amingruppen an die Oberfläche der mTa_2O_5 unter Ausnutzung der ähnlichen Pearsonhärte aufwachsen gelassen. Für die Aminfunktionalierung wurde ein Amin mit einer Silangruppe, namentlich 3-Aminopropyltriethoxysilan (APTES), kovalent an die Tantaloxidoberfläche gebunden.
Tantaloxidnanopartikel können darüber hinaus als Kontrastmittel für die Computertomographie genutzt werden. Um diese Nanopartikel auch als Magnetresonanztomographie (Magnetic Resonance Imaging, MRI) einsetzen zu können, wurden die mTa_2O_5 mit verschiedenen Konzentrationen paramagnetischer Ionen, oder genauer Gd^{3+}, dotiert. Zwecks Biokompabilität und Wasserlöslichkeit wurden die mTa_2O_5:Gd mit Methoxy(polyethylenoxy)propyltrimethoxysilan (PEG-TES) und Aminopropyltriethoxysilan (APTES) funktionalisiert, während letzteres auch dafür genutzt wurde weitere Funktionalitäten wie Farbstoffe anzubinden. Es konnte gezeigt werden, dass mTa_2O_5 simultan als MRI- und CT-Kontrastmittel verwendet werden kann, wobei die beste MRI-Kontrastverstärkung bei niedrigen Gd^{3+}-Konzentrationen auftrat.

Contents

Acknowledgements iv

Abstract vii

Zusammenfassung viii

List of figures xix

List of tables xxi

List of Abbreviations xxiii

1. Introduction 1

2. Synthesis of non-porous and mesoporous nanoparticles 5

2.1. Introduction 5
2.2. General considerations 5
2.3. Synthesis methods of metal oxide nanoparticles 8
2.3.1. Microemulsions 8
2.3.2. Thermal decomposition 8
2.3.3. Solvothermal methods 9
2.4. Synthesis of non-siliceous mesoporous metal oxide nanoparticles 11
2.4.1. Soft-templating method 11
2.4.2. Hard-templating method 13

3. Synthesis and catalytic performance of vanadium oxide nanoparticles 15
3.1. Abstract . . . 15
3.2. Introduction . . . 15
3.3. Experimental Section . . . 18
3.4. Results and Discussion . . . 20
3.4.1. Influence of the solvent composition . . . 20
3.4.2. Influence of the type of alcohol used . . . 27
3.4.3. Rods, Sheets and Urchins . . . 28
3.4.4. Peroxidase activity . . . 31
3.5. Conclusions . . . 33

4. Synthesis of crystalline tantalum oxide and tantalate nanoparticles and their photocatalytic behavior 41
4.1. Abstract . . . 41
4.2. Introduction . . . 41
4.3. Experimental section . . . 43
4.4. Results and Discussion . . . 45
4.4.1. Influence of the pH value . . . 45
4.4.2. Influence of the base (counter cation) at pH=7 and pH=12 . . . 49
4.4.3. Ion exchange in the tantalates and heat treatment . . . 52
4.4.4. Photocatalytic activity . . . 57
4.5. Conclusions . . . 58

5. Synthesis of mesoporous tantalum oxide and loading with palladium nanoparticles 59
5.1. Abstract . . . 59
5.2. Introduction . . . 59
5.3. Experimental . . . 61
5.4. Results and Discussion . . . 64
5.4.1. Synthesis of mesoporous tantalum oxide . . . 65
5.4.2. Structural characterization . . . 69
5.4.3. Functionalization with palladium Nanoparticles . . . 75
5.5. Conclusions . . . 80

6. Gadolinium doped mesoporous tantalum oxide nanoparticles as multimodal contrast agent 83
6.1. Abstract . . . 83

6.2. Introduction 83
6.3. Experimental 87
6.4. Results and Discussion 91
6.4.1. Structural characterization of Gadolinium doped mesoporous tantalum oxide 92
6.4.2. Surface functionalization and biocompatability 96
6.4.3. Drug release 101
6.4.4. Application as multimodal contrast agent 102
6.5. Conclusion 105

7. Conclusion and Outlook **107**

Appendix **111**

A. Appendix **111**
A.1. Supporting Information 111
A.2. List of publications 121

Bibliography **121**

List of Figures

2.1. Schematic LaMer diagram for nanoparticle growth 6
2.2. TEM images of Fe_3O_4 nanoparticles synthesized *via* thermal decompostion of Fe(Oleate)$_3$ with different sizes 9
2.3. ErOOH and Er_2O_3 micro- and nanostructures obtained from a solvothermal route with different sizes, shapes and phases as a function of the reaction temperature and the decanoid acid (DA)/erbium molar ratio. . 10
2.4. Schematic illustration of the soft-template approach for the synthesis of mesoporous metal oxides. 12
2.5. Examples for mesoporous metal oxide spheres synthesized by a soft-template approach 13
2.6. Schematic illustration of the single steps during hard-templating (nanocasting) to obtain mesoporous materials. 14

3.1. TEM micrographs of the reaction products with different water:ethanol ratios. 21
3.2. Schematic representation of the morphological relation between the sheets and urchins. 22
3.3. X-ray diffraction patterns of the reaction products with different water:ethanol ratios. 24
3.4. TEM micrographs of the VO_x nano-urchin formation at different reaction temperatures, namely a) 423 K and b) 473 K. 25
3.5. TEM images of the VO_x nano-urchin formation in dependence on the amount of Pluronic F127 used. a) 0 mg and b)1000 mg of Pluronic F127. 25

3.6. TEM micrographs of the VO_x urchins heated with 2 K/min to a) 453 K and b) 723 K for 3 h each. c) X-ray diffraction pattern of the urchins heated to 453 and 723 K, respectively, and tic marks of V_2O_5 at the bottom. 34
3.7. TEM micrographs of the VO_x nanoparticles with different alcohols. . . . 35
3.8. Schematic illustration of the gradual morphology change of the VO_x nanoparticles from urchin-like to sheets obtained with alcohols having different chain lengths. 35
3.9. X-ray diffractogramms of the reaction products obtained with different alcohols as solvents. 36
3.10. IR spectra of the VO_2 nanorods, VO_x nano-sheets and urchins. 36
3.11. Normalized Raman spectra of the VO_2 rods (black), VO_x nano-sheets (red) and nano-urchins (green). 37
3.12. a) TEM EDX and b) darkfield image c) and d) electron diffraction pattern and d) darkfield image showing radiation damage of the VO_x nano-sheets. 38
3.13. XPS data of the VO_2 nanorods (black), VO_x nano-sheets (red) and nano-urchins (green). 39
3.14. Chemical structure of ABTS and its oxidation products and their emission maxima that occur during the ABTS oxidation with H_2O_2. 39
3.15. a) Steady-state kinetic assay of VO_x urchin, sheets and VO_2 rods compared to bulk V_2O_5 by variation of the nanoparticle concentration. b) UV-VIS spectra of ABTS with H_2O_2 in acetate buffer after incubation with VO_x urchins, sheets and VO_2 40
3.16. Steady-state kinetic assay of VO_x urchin, sheets and VO_2 rods compared to bulk V_2O_5 by variation of the NP concentration normalized to the surface area. 40

4.1. (a-g) TEM micrographs of the tanalum oxide nanoparticles at different pH values. a) pH=3 b) pH=4 c) pH=7 d) pH=8 e) pH=9 f) pH=12 and g) pH=13. h) shows the pH values of the reaction mixtures before (and after) the hydrothermal treatment based on the NaOH concentration. . 46
4.2. X-ray diffraction patterns and corresponding Rietveld fits of the products prepared at different pH values 48
4.3. X-ray diffraction patterns and corresponding Rietveld fits of $MTaO_3$ (M=Na, K, Rb) nanocubes at pH=12 50
4.4. EDX of the tanalum oxide rods obtained with 5 mM RbOH. 51

4.5. TEM micrographs of the nanoparticles yielded with different bases at different pH values. a) pH=7 with KOH and b) RbOH as applied base and c) KOH at pH=12 and d) RbOH at the same pH. 52
4.6. a) HRTEM image of the cubes with 0.1 M RbOH and corresponding FFT. c) HRTEM micrograph of the Ta_2O_5 nanorods synthesized with 5 mM RbOH and associated d) FFT of the nanorods. 53
4.7. TEM images of a) the tantalate nanoparticles after acid treatment, b) heat treated cubes after 12 h at 923 K, and c) annealed nanorods after 12 h at 1023 K. 54
4.8. X-ray diffraction patterns and corresponding Rietveld fits of (i) tantalum oxide rods after annealing at 1123 K for 12 h, (ii) cubes after annealing at 1023 K for 12 h, and (iii) tantalates after and (iv) before acid treatment. 55
4.9. a) HRTEM image of the heat treated rods (12 h, 1123 K) with b) the corresponding FFT pattern. c) HRTEM micrograph of the heat-treated cubes (12 h, 1023 K) synthesized with 0.1 M KOH and the corresponding FFT pattern in d). 56
4.10. UV-VIS spectra of the tantalum oxide samples after UV light irradiation and corresponding digital photographs. 57

5.1. Schematic representation of the synthesis and heat treatment of mTa_2O_5 and their subsequent amine-functionalization and decoration with palladium nanoparticles. 64
5.2. TEM images of the synthesis with 0.5 mL a) HCl b) acetic acid c) only with water d) 0.5 mL and e) 19 mL NH_3 and f) 0.5 g NaOH. 65
5.3. TEM images of the mTa_2O_5 nanoparticles in dependence on the Pluronic amount. a) 600 mg b) 100 mg and c) 0 mg Pluronic F127. 66
5.4. TEM images of the mTa_2O_5 nanoparticlesin dependence of the water temperature. Water temperature in a) 279 K b) 298 K and c) 318 K. . . 68
5.5. TEM micrographs of the mTa_2O_5 a) as synthesized and after b) 1 h c) 3 h and 6 h at 923 K. 69
5.6. TEM micrograph of the mTa_2O_5 heat treated at 1123 K for 6 h. 70
5.7. HRTEM micrographs of as synthesized and annealed (6 h, 923 K) mTa_2O_5 nanoparticles and correspondings SAED patterns 71
5.8. X-ray diffraction patterns and corresponding Rietveld fits of the (i) as synthesized mTa_2O_5 and heat treated mTa_2O_5 for (ii)1 h, (iii) 3 h and (iv) 6 h at 923 K. Bottom: tic marks of Ta_2O_5. 72

5.9. a) N_2 soprtion isotherms and b) BJH desorption pore-size distributions of the mTa_2O_5 as synthesized and heat treated at 923 K for 1, 3 and 6 h. 73
5.10. Schematic illustration of the decrease in surface area (darker blue) and increase in pore size (green) upon heat treatment of the mTa_2O_5 nanoparticles. 74
5.11. Simplified scheme of the silanisation reaction of APTES on the mTa_2O_5 nanoparticle surface. 76
5.12. IR spectra of the as synthesized mTa_2O_5 (black), the amine functionalized mTa_2O_5 (red) and the Pd@mTa_2O_5 (green) nanoparticles. 77
5.13. TEM micrographs of the a) and b) the as synthesized Pd@mTa_2O_5 nanoparticles and the c) and d) heat treated (6 h, 923 K) Pd@mTa_2O_5 . 78
5.14. X-ray diffraction patterns and corresponding Rietveld fits of the Pd@mTa_2O_5 with (i) as synthesized mTa_2O_5 and (ii) annealed mTa_2O_5 nanoparticles. 79
5.15. N_2 sorption isotherm (black) and BJH desorption pore-size distributions (red) of Pd@mTa_2O_5 nanocomposite. 80

6.1. Schematic illustration of the synthesis of the mTa_2O_5:Gd and their subsequent functionalization. 91
6.2. TEM micrographs of the mTa_2O_5:Gd with different nominal Gd amounts. 92
6.3. Left: STEM image of mTa_2O_5:Gd with 1% of Gd and on the right: corresponding EDX line scan. 94
6.4. XRD pattern of the as synthesized mTa_2O_5:Gd nanoparticles with a nominal amount of 6% Gd. 95
6.5. N_2 soprtion isotherm (black) and BJH desorption pore-size distributions (red) of mTa_2O_5:Gd with a nominal Gd amount of 6%. 96
6.6. a) IR spectra of the mTa_2O_5:Gd and mTa_2O_5:Gd-PEG-TES nanoparticles. b) UV-VIS spectra of mTa_2O_5:Gd-PEG-TES and mTa_2O_5:Gd-FITC-PEG nanoparticles in water. 97
6.7. Cytotoxicity-assay of the mTa_2O_5:Gd-PEG-FITC NP performed with different nominal Gadolinium amounts (between 0% and 25% Gd). The HeLa cells were grown overnight before they were incubated with the NP for 24 h. 99
6.8. Confocal laser scanning images of HeLa cells stained with Alexa Fluor® 555 Phalloidin incubated with a) 25 μg/mL, b) 50 μg/mL and c)100 μg/mL mTa_2O_5:Gd-PEG-FITC for 24 h. 100

6.9. Release profile of diclofenac (see inset) from mTa_2O_5-NH_2 nanoparticles in PBS buffer at ambient temperature. 101
6.10. a) CT contrast of mTa_2O_5:Gd-PEG-APTES in dependence on the Ta concentration b) T_1 measurement of the mTa_2O_5:Gd-PEG-APTES with the relaxivity r_1 in dependence on the Gadolinium concentration c) images of the T_1 contrast of mTa_2O_5-PEG-APTES (left) and mTa_2O_5:Gd-PEG-APTES (right) in dependence on the concentration. 103

A.1. IR spectra of the $VO(acac)_2$ (black) precursor used in the synthesise of the VO_x nanourchins (red). 111
A.2. Multipoint BET of the VO_2 rods and VO_x urchins and sheets. 113
A.3. Histograms of the $NaTaO_3$ nanorods synthesized at pH=12 (left) and pH=13 (right) 113
A.4. Histograms of the $KTaO_3$ (left) and $RbTaO_3$ nanoparticles synthesized at pH=12. 114
A.5. X-ray diffraction patterns of the Tantalum oxide rods with 5 mM NaOH, KOH, RbOH (from bottom to top) respectively. 114
A.6. UV-VIS spectra of the samples with RhB after stirring in the dark for 18 min and centrifugation of the nanoparticles 116
A.7. Confocal laser scanning microscope image of HeLa cells stained with Alexa Fluor® 555 Phalloidin without nanoparticles. 118
A.8. T_1 relaxivity plots for mTa_2O_5:Gd nanoparticles with different Gd concentrations. 119

List of Tables

5.1. Structural parameters of the mTa_2O_5 in dependence on the time of heat treatment at 923 K 74

6.1. Composition and structural parameters of the mTa_2O_5:Gd nanoparticles in dependence on the Gd concentration. 95
6.2. Relaxivity r_1 of the mTa_2O_5:Gd nanoparticles with different Gd amounts. 104

A.1. Measurement and refinement parameters of the X-ray diffraction patterns of the products prepared at different pH-values. 112
A.2. Measurement and refinement parameters of the X-ray diffraction patterns of the cube-shaped nanoparticles with different bases 115
A.3. XRF data of the cube-shaped $MTaO_3$ (M=Na, K, Rb) before and after treatment with 2 M HCl for 30 min. 116
A.4. Measurement and refinement parameters of the X-ray diffraction pattern of the acid treated (2 M HCl) cube-shape nanoparticles and the heat treated rods and cube-shaped nanoparticles. 117
A.5. Measurement and refinement parameters of the X-ray diffraction patterns of heat treated mTa_2O_5 for 6 h at 923 K 118

List of Abbreviations

μ	mass attenuation coefficient
ABTS	2,2´-azino-bis(3- ethylbenzo-thiazoline-6-sulfonic acid
APTES	3-Aminopropyltriethoxysilane
BET	Brunauer-Emmett-Teller (determination of surface area)
BJH	Barrett-Joyner-Halenda (Calculation of pore size and volume)
BSA	Bovine serum albumin
BzOH	Benzyl alcohol
CT	Computed tomography
CTAB	Cetyl trimethylammonium bromide
Diclofenac	2-[2-(2,6-Dichlorophenylamino)phenyl]acetic acid
EDX	Energy dispersive X-ray
EISA	Evaporation induced self-assembly
FFT	Fast fourier transform
FITC	Fluorescein 5(6)-isothiocyanate
FT-IR	Fourier-transformed infrared

HRTEM	High resolution transmission electron microscopy
HU	Hounsfield units
ICP-MS	Inductively coupled plasma mass spectrometry
MRI	Magnetic resonance imaging
mTa_2O_5	Mesoporous tantalum oxide
NBD	4-Chloro-7-nitrobenzofurazon
NP	Nanoparticle
PBS	Phosphate buffered saline
PEG	Poly(ethylene glycol)
PEG-TES	Methoxy(polyethyleneoxy)propyltrimethoxy silane
RES	Reticuloendothelial system
RhB	Rhodamine B
S_{BET}	BET surface area
SAED	Selected Area Electron Diffraction
TEM	Transmission electron microscopy
XPS	X-ray photoelectron spectroscopy
XRF	X-ray fluorescence

1 Introduction

Nanomaterials are an integral part of our life as they are added to everyday consumables like toothpaste, sun-screen or band-aids.[1] Still, the possible applications of nanoparticles expand on a broad range of different fields such as catalysis,[2,3] biotechnology,[4,5] electronics,[6] medicine[7,8] and energy.[9,10] These applications mostly stem from the unique physical properties of nanoparticles. Due to their size between 1-100 nm (at least in one dimension), their properties are between that of molecules and bulk materials. Moreover, size-dependent effects come into play at this length scale that are either related to the large fraction of surface atoms or quantum-size effects.[11] Hence this size dependence inspired the synthesis of a wide range of nanoparticles with different compositions and sizes.

Nowadays the toolbox in nanoparticle synthesis is not only limited to composition and size control but it expands to morphology control, recombination of diverse materials into even complex structures, hybrid materials and (self-)assembly of nanoparticles facilitating new functionalities.[12–15] Next to size-dependent effects, many nanoparticle properties, e.g. magnetic[16] and catalytic properties,[15,17] are dependent on various factors and their interplay. Therefore not only the size but the shape of nanoparticles can influence their properties which opened a new avenue for further tailoring the properties of nanoparticles.[18] As a consequence, various different morphologies have been synthesized with progressively complex shapes e.g. rods, cubes, stars, plates, tetrahedrons and many more.[19–21]

One of the current challenges is the tailor synthesis of nanoparticles that suit the intended applications precisely and open even more avenues for new applications. For catalysis there are several key features governing the catalytic activity of nanomaterials like surface area, composition, defects and shape. As the catalysis occurs at the

surface, it is one of the major challenges to synthesize stable nanoparticles with high surface areas. In one approach, high surface materials are achieved with mesoporous nanoparticles characterized by their pores between 2 and 50 nm, that contribute to the overall surface area.[22] As a consequence, the surface area of mesoporous particles exceeds even those of small nanoparticles with high surface-to-volume ratio while they are more stable. Therefore mesoporous materials are readily applied in catalytic applications.[23–25] However, the synthesis of metal oxide mesoporous nanoparticles, other than silica, remains a challenge due to the high reactivity of their precursors[26,27] that often leads to bulk materials instead of mesoporous nanoparticles. Hence great efforts are put in the development of synthetic routes for mesoporous transition metal nanoparticles.
Moreover, the surface area of nanoparticles is a function of their shape as different morphologies have varying surface-to-volume ratios.[28,29] This is why high surface areas can be realized in nanoparticles with high surface-to-volume ratios. Additionally, the shape itself features in the catalytic activity of nanoparticles because different facets and active sites with different activity are exposed.[30,31] Therefore the synthesis of nanoparticles with different shapes is desirable.
Another highly evolving field is the nano-biotechnology or nanomedicine. Nanomaterials have been investigated for their potential applications in biomedical imaging, diagnostics and therapy.[8,32–34] As their size is comparable to many biological structures like enzymes they can be transported via bloodstream and internalized in cells.[35] Nanoparticle surfaces can be functionalized to assure biocompability and achieve targeted delivery through moieties capable of recognizing miscellaneous complementary biomolecules.[36–38] The intrinsic physical and chemical properties of inorganic nanomaterials contribute the contrast for common biomedical imaging such as X-ray computed tomography (CT) and magnetic resonance imaging (MRI). Each imaging modalitiy has its own intrinsic strengths and limitations. As a consequence, different imaging methods are combined to circumvent their complement weaknesses and exploit their full capacity which is also referred to as multimodal imaging.[39,40] However, the requirements for contrast enhancement differ for every imaging method. For example, nanoparticles containing elements with high atomic numbers can provide a CT contrast enhancement whereas magnetic particles generate a MRI contrast and different concentrations of contrast agents are used.[41–44] Therefore much effort has been put in the design of nanomaterials that simultaneously fulfill the contrast enhancement requirements of various imaging techniques.
This doctoral thesis is a contribution to the ever growing field of nanoparticle synthesis with a focus on group five porous and non-porous metal oxide nanoparticles together

with their morphology control. Further the particles are screened for catalytic and medical applications.

- First the theoretical background for the nanoparticle synthesis is given in **chapter 2**. The LaMer model is presented as a simple model that is used to explain the formation of monodisperse (same size) nanoparticles by separating the nucleation and growth of the particles. Further typical syntheses for non-porous and porous nanoparticles are surveyed together with the advantages as well as drawbacks of each method. For non-porous nanoparticles microemulsion, thermal decomposition and hydrothermal synthesis are elucidated as examples for the best size and morphology control. Hard- and soft-templating methods are explained that lead to mesoporous nanomaterials.

- In **chapter 3** the synthesis of VO_2(B) nanorods as well as VO_x nano-urchins and -sheets is described using a solvothermal method. This chapter demonstrates the influence of the solvent and solvent composition on the particle morphology for solvothermal reactions. The morphology ranges from rods in water, over sheets in EtOH/H_2O to nano-urchins in pure ethanol. Applying alcohols with longer chains as solvent and surfactant, the morphology of the nanoparticles changes from urchins to sheets. The catalytic activity of VO_2(B) rods, VO_x urchins and sheets is evaluated for peroxidase mimicked reactions. Moreover, the surface area of these nanoparticles is related to their surface area.

- **Chapter 4** presents a new hydrothermal synthesis for Ta_2O_5 nanorods, $MTaO_3$ (M=Na, K, Rb, H) and Ta_2O_5 cube-shaped nanoparticles. The influence of pH value as well as of the counter cation of the used base on particles morphology and composition is investigated. The $MTaO_3$ (M=Na, K, Rb) nanoparticles exhibit a pyrochlore structure which makes them prone to ion exchange. This is exploited when the alkali ions are exchanged for protons to gain cubic Ta_2O_5 nanocrystals upon heat treatment. Additionally the photocatalytic activity of the nanoparticles is investigated which was tested by the degradation of Rhodamine B.

- **Chapter 5** describes the synthesis of mTa_2O_5 nanoparticles and their subsequent decoration with palladium nanoparticles. At first the synthesis parameters of mTa_2O_5 are established in terms of temperature, template concentration and solvent. Additionally, the formation mechanism of the mTa_2O_5 nanoparticles is revealed to be a self-assembly mechanism. Upon heat treatment the mTa_2O_5 nanoparticles crystallize while the pore-sizes expand from 3.7 to 8.1 nm. The

mTa_2O_5 nanoparticles are functionalized with amine groups *via* surface silanization with an aminosilane for further functionalization. Palladium nanoparticles are formed *in situ* and attached to the mTa_2O_5 *via* coordination to the amine groups to yield Pd@mTa_2O_5.

- In **chapter 6** the mTa_2O_5 nanoparticles introduced in chapter 5 are doped with various amounts of gadolinium to yield mTa_2O_5:Gd nanoparticles. The mTa_2O_5:Gd nanoparticles are investigated as multimodal imaging agents for fluorescence imaging, CT and MRI. For this the nanoparticles are biofunctionalized with PEG groups and their biocompability is confirmed by cytotoxicity assays. For imaging purpose the mTa_2O_5 nanoparticles are further functionalized with dye molecules which makes them observable in fluorescence imaging. This is demonstrated by fluoresence images of cells incorporated with dye functionalized mTa_2O_5. The CT as well as the MRI contrast of the mTa_2O_5:Gd are demonstrated. Furthermore the mTa_2O_5 nanoparticles are tested for drug delivery by observing the release of diclofenac.

- Finally, **chapter 7** summarizes and concludes the findings of this doctorate work in the chapters 3 to 6. In addition, it gives an outlook to future projects.

2 Synthesis of non-porous and mesoporous nanoparticles

2.1. Introduction

For the last three decades, there has been a tremendous effort to synthesize nanoparticles with defined composition, size and shape.[45] Nanoparticles are defined by their dimension between 1 and 100 nm in at least one dimension. The interest in nanoparticle synthesis originates from their unique physical properties as compared to their bulk counterparts and molecular species.[19] Additionally, the exact size as well as the shape of nanoparticles influences their properties, too.[15,18]
In principle, there are two different approaches to obtain nanomaterials. On the one hand the starting materials are bulk materials that are physically scaled down. On the other hand molecular species are assembled until they are in the nanometer size regime. The former is called "'top down", whereas the latter is named "bottom up".[14,46–48] For industrial purposes the top down methods are preferred as they are easily upscalable and cheap. Yet they lack in size and shape control which is essential for many applications. In contrast, monodisperse and shape controlled nanoparticles can be synthesized with colloidal solution bottom up methods. One major drawback, however, is the small nanoparticle output and high effort necessary in this kind of synthesis.[14,46] Since the properties of nanoparticles can be highly dependent on their size and shape only bottom up methods will be considered in the following.

2.2. General considerations

Up to today the growth mechanism of nanoparticles is not completely elucidated. Albeit different theories are proposed to explain the nucleation and growth of nanoparticles.

Classically the formation of nanoparticles is described by the LaMer model with subsequent Ostwald ripening.[19,49,50] In the 1940´s LaMer and Dinegar proposed this mechanism based on micrometer sulfur sols that is also applicable for many other nanomaterials. The key point of this model is a short nucleation burst followed by a slow growth step meanwhile no further nucleation occurs. According to LaMer the generation of nanoparticles is divided in three distinct phases as depicted in Figure 2.1. At first the concentration of monomers, which are defined as minimal building blocks

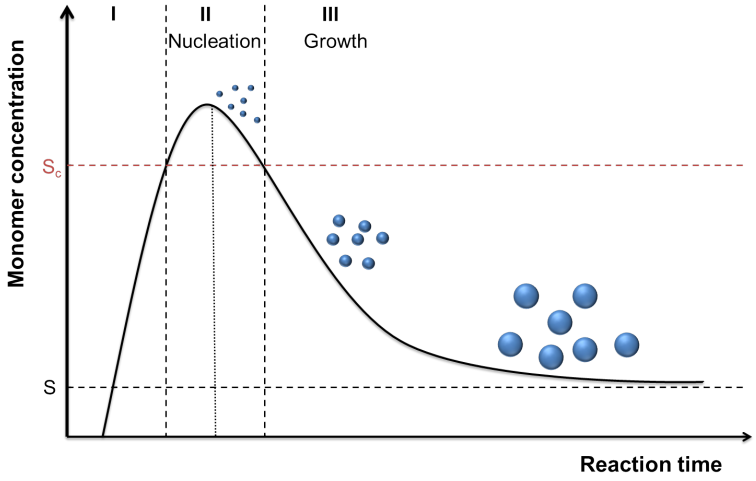

Figure 2.1.: Schematic LaMer diagram featuring the three reaction phases that include nucleation and growth that have to be separated for monodisperse nanoparticle formation. S symbolizes supersaturation and S_c critical supersaturation.

of a nanoparticle, increases rapidly. This continues beyond supersaturation (S). The concentration, however, can exceed supersaturation due to the energy barrier of homogeneous nucleation that is given by the Gibbs free energy (ΔG). As the nucleus is regarded as a sphere with the radius r, the Gibbs free energy can be expressed as:

$$\Delta G_S = 4\pi r^2 \gamma + \frac{4}{3}\pi r^3 \Delta G_v \tag{2.1}$$

Here γ is the surface free energy per unit area and ΔG_v is the change of free lattice energy, when the crystallites are formed. Since ΔG_v is always negative and γ always positive, ΔG_S has a maximum at the critical radius r_c that can be expressed as:

$$r_c = \frac{-2\gamma}{\Delta G_v} = \frac{2\gamma V_m}{RT \ln S} \tag{2.2}$$

ΔG_v is also given by $\Delta G_S = (-RT \ln S)/V_m$, with R as gas constant, T as temperature and V_m as the molar volume of the bulk crystal. The critical radius marks the threshold for stable nucleus, for $r \leq r_c$ the nuclei dissolve again whereas for $r \geq r_c$ the nuclei can grow. In phase II the concentration rises beyond the critical supersaturation S_c. Above this point, the energy barrier for stable nucleus formation is exceeded. This energy ΔG_{S_c} can be determined when the value for r_c (see equation 2.2) is pluged in equation 2.1:

$$\Delta G_{S_c} = \frac{16\pi\gamma^3}{3(\Delta G_v)^2} = \frac{16\pi\gamma^3 V_m^2}{3(RT \ln S)^2} \tag{2.3}$$

At this point, there is a nucleation burst where a great number of nuclei is formed simultaneously. The rate of nucleation ($\mathrm{d}N/\mathrm{d}t$) can be estimated with the Arrhenius equation:

$$\frac{\mathrm{d}N}{\mathrm{d}t} = A \exp\left[-\frac{\Delta G_{S_c}}{k_B T}\right] = A \exp\left[\frac{16\pi\gamma^3 V_m^2}{3(k_B T)^3 (\ln S)^2}\right] \tag{2.4}$$

Herein, N is the number of nuclei, A is a pre-exponential factor and k_B is the Boltzmann constant. As many nuclei form, the concentration of free monomers in the solution reduces significantly. After this point, the monomer concentration drops rapidly below the critical supersaturation. Hence no more nucleation can occur. In the third phase, the nuclei grow slowly which is controlled by diffusion of monomers in solution. Since all nuclei were virtually formed at the same time all nanoparticles have identical growth histories leading to a narrow size distribution. This concept also illustrates the importance of separate nucleation and growth, because otherwise the growth history would be different and the sizes would vary.

It should be noted, that this theory was developed for microparticle systems, where the values for V_m and γ resemble the used bulk values better than nanomaterials whereas they can differ more for nanoparticles.[51] In addition, for nanoparticles their high surface-to-volume ratio has to be considered. The high ratio of surface atoms accompanies a high surface energy. This is the driving force for uncontrolled growth and particle agglomeration. Commonly surfactant molecules are used to stabilize the nanoparticles in solution. Typically these molecules have a functional group that can attach to the nanoparticle surface and a long hydrocarbon chain for steric stabilization.[14,45]

2.3. Synthesis methods of metal oxide nanoparticles

There are many different colloidal synthesis methods for the fabrication of metal oxide nanoparticles such as microemulsions, thermal decomposition of organometallic precursors, solvothermal reactions, spray-pyrolysis, co-precipitation and sol-gel.[52–54] The following section will focus on thermal decompostion, microemulsions and hydro-/solvothermal synthesis which allow the highest degree in size as well as shape control.

2.3.1. Microemulsions

In a microemulsion synthesis the formation of nanoparticles takes place in micelles which act as "nanoreactors". As opposed to conventional emulsions, microemulsions are thermodynamically stable solutions. They consist of two initially immiscible liquids stabilized by a surfactant. In case of a reverse microemulsion or water-in-oil emulsion the majority phase consists of an organic solvent, like cyclohexane, while water is dispersed in nanometer-sized (1-20 nm) droplets.[55,56] The size of the reverse micelle, and therefore also the size of the synthesized nanoparticles, is determined by the ratio of water relative to the surfactant (or co-surfactant).[15,57,58] While most nanoparticles from microemulsions are spherical other shapes such as rods can be obtained as well especially at high surfactant concentrations.[59,60] A wide variety of metal oxide nanoparticles can be synthesized with microemulsions among them are TaO_x,[61] TiO_2,[62] CeO_2.[59] One of the major drawbacks of this method is the low yield when compared to the reaction volume.

2.3.2. Thermal decomposition

Various inorganic nanoparticles can be synthesized through thermal decomposition of organometallic precursors in organic high boiling solvents in the presence of stabilizing capping agents. Those nanoparticles can be highly monodisperse with controlled morphology. The key to monodisperse nanoparticles is to ensure a short burst of nucleation (see the LaMer model in chapter 2.2). In practice this burst of nucleation is either achieved by hot injection, where a thermally instable precuror, e.g. metal carbonyls,[63] is rapidly injected into the hot reaction mixture. Alternatively the reaction mixture is heated with the precursor in a controlled manner.[46,47,51]
One well known example of a heat up synthesis is the thermolysis of iron(III) oleate to form monodisperse Fe_3O_4 nanoparticles reported by Park et al..[64] The size of the Fe_3O_4 nanoparticles is changed by varying the amount of oleic acid, which acts as

capping agent. Furthermore, the nanoparticle size increases with the boiling point of the solvent as depicted in Figure 2.2.[65] Additionally cubic nanoparticles are obtained when sodium oleate is added to the reaction. This synthesis was also adapted for other metal oxides like MnO,[66] where manganese(II) oleate was used. Thermal decomposition is a

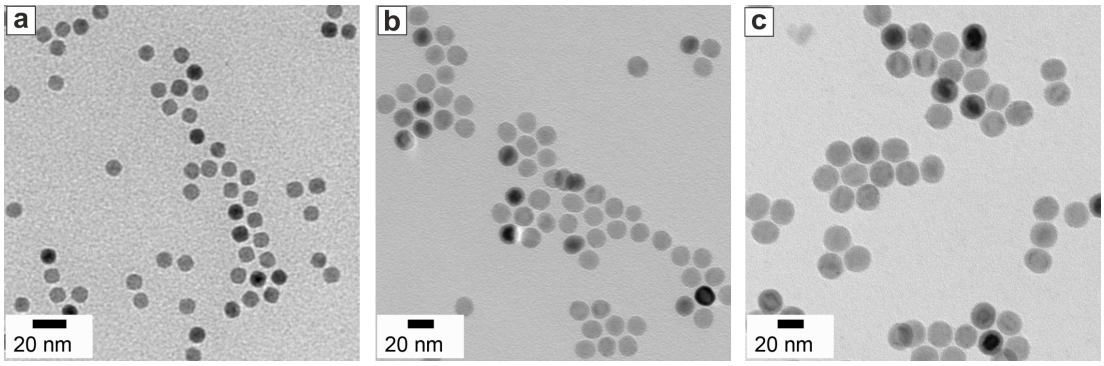

Figure 2.2.: TEM images of Fe_3O_4 nanoparticles synthesized *via* thermal decompostion of $Fe(Oleate)_3$ with different sizes a) 8 nm b) 15 nm and c) 20 nm by variation of the used solvent. The solvent is a) 1-octadecene b) 1-octadecene:tri-*n*-octylamine 1:1 and c) tri-*n*-octylamine.

versatile method for nanoparticle synthesis, as there are many parameters that influence the size and morphology such as heating rate, capping agents, precursors and solvents. One of the disadvantages of thermal decomposition is the low yield of those reactions (typically around 10 mg) that cannot be upscaled in most cases. Furthermore nanoparticles synthesized by thermal decomposition are not dispersible in water due to the unpolar capping agents like oleic acid, 1,2-hexadecanediol or oleylamine.[64,66,67] Therefore an additional step is required for water solubility. Mostly the unpolar ligands are replaced by polar, water soluble ligands in a ligand exchange reaction.[68]

2.3.3. Solvothermal methods

Solvothermal/hydrothermal methods have been applied in the synthesis of a large variety of nanomaterials. They take advantage of elevated reaction temperatures above the standard boiling point of the respective solvent which increases the solubility and reactivity of the precursors considerably. On that account, the reaction mixture is placed in a sealed teflon vessel in an autoclave for high-pressure reactions. With water as a solvent solvothermal reactions are also referred to as hydrothermal. The composition, size and shape of the nanoparticles are typically controlled by: reaction time, temperature, pressure, pH, reactant concentrations and the applied capping

agents. This variety of reaction parameters gauges the versatility of solvothermal methods. As an example, Figure 2.3 illustrates how the reaction conditions can be altered to tune the composition as well as shape and size of the reaction products. At temperatures below 160°C monoclinic ErOOH microspheres are obtained whereas cubic Er_2O_3 wrinkled microspheres and flowers are procured above 160°C. When the decanoid

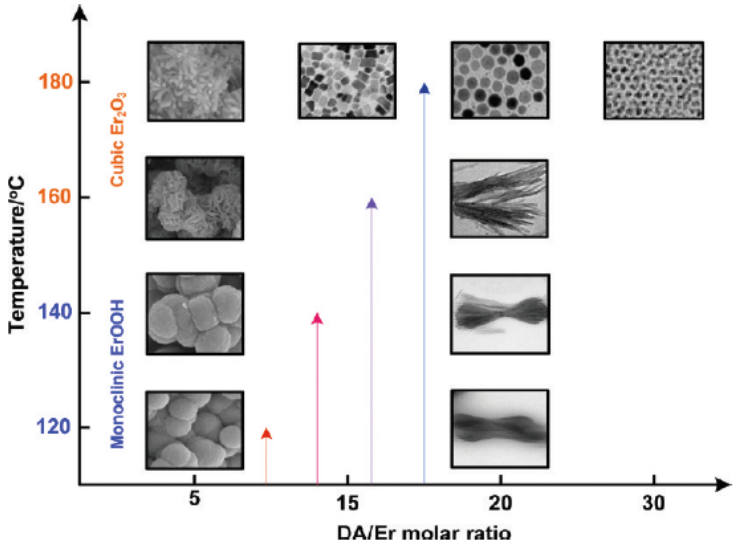

Figure 2.3.: ErOOH and Er_2O_3 micro- and nanostructures obtained from a solvothermal route with different sizes, shapes and phases as a function of the reaction temperature and the decanoid acid (DA)/erbium molar ratio. Reproduced from Nguyen et al..[20]

acid (DA)/erbium molar ratio is altered at higher temperatures the product morphology changes from microflowers over dog-bone nanoparticles to nanospheres with increasing DA amount compared to the erbium precursor.

Frequently water is used as a solvent like in the example previously discussed. In most cases it is not necessary to run hydrothermal reactions above the critical point (374°C, 22.1 MPa). But under supercritical conditions, the physical properties of water change considerably, e.g. the solubility of unpolar molecules increases distinctly. This provides different reaction opportunities that are readily used.[69] Nevertheless, many reactions are carried out under non-aqueous conditions as the hydrolysis rates are often high in water. Especially for doped metal oxides and ternary oxides it is hard to match the reactivity of different precursors. One commonly used solvent is benzyl alcohol (BzOH) which acts as solvent and surfactant at the same time.[70–72] Compared to other solvents the "benzyl alcohol" route has the advantage that the reaction mechanism is relatively

well investigated and it is possible to synthesize complex oxides as well.[72,73]
One of the advantages of solvothermal synthesis is that most of the obtained products are crystalline. Compared to thermal decomposition solvothermal methods can be upscaled more easily up to gram amounts. Additionally, nanomaterials can either be soluble in polar or unpolar solvents depending on the capping agent used during synthesis.

2.4. Synthesis of non-siliceous mesoporous metal oxide nanoparticles

Mesoporous materials are characterized by pores in the size range between 2-50 nm according to IUPAC.[22] They possess many attractive properties like a high surface area (up to 1000 m^2/g for mesoporous silica), tunable pore sizes in various shapes and structures.[26,74–76] This makes mesoporous materials suitable for a wide range of applications such as catalysis, drug delivery, lithium ion batteries, solar cells, gas sensors and adsorption.[2,23,24,32,77–81]
Mesoporous silica is the prototype for other mesoporous materials since it has been discovered in the early 1990s.[82,83] There are, however, significant differences between the synthesis of mesoporous silica and other metal oxides especially transition metal oxides. The hydrolysis and condensation of silica precursors can be well controlled whereas the hydrolysis of transition metals is faster and their chemistry is more versatile.[24,84] Furthermore the obtained mesoporous silica is stable while other oxides can be susceptible to various reactions like hydrolysis, redox reactions or phase transitions. Hence the focus of this chapter will be on non-siliceous mesoporous metal oxides.

2.4.1. Soft-templating method

As soft-templating with surfactants or block copolymers is the typical synthesis route for mesoporous silica, it is also adapted for other mesoporous oxides. The general idea of the soft-templating method is that the used template assembles into mesostructured micelles. Those micelles are the negative template for the mesoporous oxide. Typically soft templates are surfactants such as alkylamines and cetyl trimethylammonium bromide (CTAB)[75,85–87] or coblock polymers[88] like Pluronic.[89–91]
Figure 2.4 illustrates the typical steps for the soft-templating approach. Either the surfactants and the inorganic precursors assemble together to form a mesostructured phase or it is already organized in a so called liquid crystal mesophase and the inorganic precursors are impregnated later.[92,94] Then the precursors transform into mesostruc-

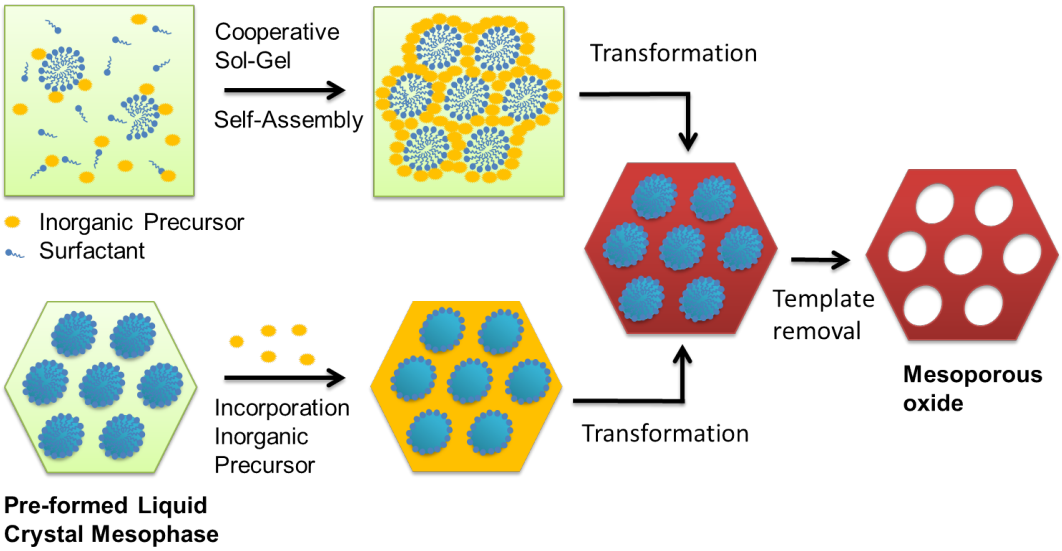

Figure 2.4.: Schematic illustration of the soft-template method for mesoporous oxides *via* two different synthetic approaches. Top: cooperative self-assembly assisted by surfactants. Bottom: "true" liquid-crystal templating process.[92,93]

tured composites mostly by a hydrolysis-condensation reaction. In the last step the template has to be removed to obtain mesoporous oxides with an open pore structure. In this step the samples are either heat-treated or the templating agent is washed out with a suitable solvent. In practice soft-templating is often realized *via* an aqueous solution synthesis or evaporation induced self-assembly (EISA).[90,96–98] For the former the key factor of the synthesis is the control over the hydrolysis and condensation ratio. To do so the interactions between the inorganic precursor and the surfactant need to be strong like a coulomb interaction. Furthermore, chelating ligands like acetylacetone can be added to slow the hydrolysis rate down which is called "ligand assisted".[99] In case of EISA the used non-aqueous solvents possess a relative low polarity for a controlled hydrolysis. During the reaction the volatile solvent evaporates and the surfactants form liquid-crystal mesophase with the inorganic precursors amidst them.[26]
As an example, Figure 2.5 presents some SEM and TEM images of mesoporos metal oxide spheres synthesized by a soft-template approach.[95] In this case TiO_2, Al_2O_3 and ZrO_2 were synthesized by a combined EISA and aerosol-spray process. The pores can clearly be observed as areas of lower constrast in the TEM images.

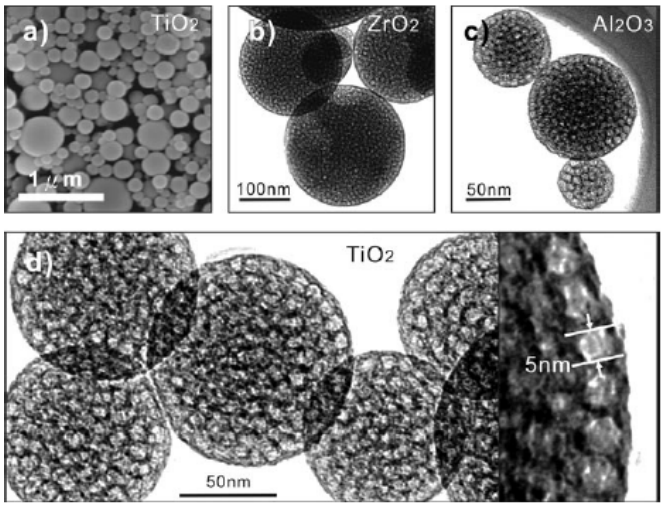

Figure 2.5.: Examples for mesoporous metal oxide spheres synthesized by a soft-template approach. a) SEM image of mesoporous TiO_2. TEM images of b) mesoporous ZrO_2 c) Al_2O_3 and d) TiO_2 where the inset magnifies the pores. Taken from Tsung et al..[95]

2.4.2. Hard-templating method

The main difference between soft- and hard-templating methods is the choice in templates.[100] Hard templates are solids with a rigid structure in contrast to soft templates like polymers. Typical hard templates for mesoporous materials are mesoporous silica[21,78,101,102] and carbon.[74,103–105] Further hard templates like alumina membranes[106] and carbon tubes[107,108] can be used to obtain other morphologies like rods that will not be discussed in this section. Hard-templating, which is also called nanocasting, can be used to obtain mesoporous materials that are not accessible *via* soft-templating.[27] Furthermore, nanocasting often leads to crystalline mesoporous products whereas soft-templating is mostly limited to amorphous products. hard templates can be subjected to higher temperatures and still stabilize the mesopores.
Basically every hard template synthesis consists of four different steps that are depicted in Figure 2.6. In a first step a suitable mesoporous template has to be supplied. The mesoporous structure of the product depends on the pore structure of the chosen template as the hard template acts as a mold. This allows to determine the mesostructure of the product through the choice in template.[24] In order to obtain mesoporous materials, the pores of the template need to be interconnected, because the former voids will make up the new product. At times it is possible to reproduce the morphology of the template as well.[109]

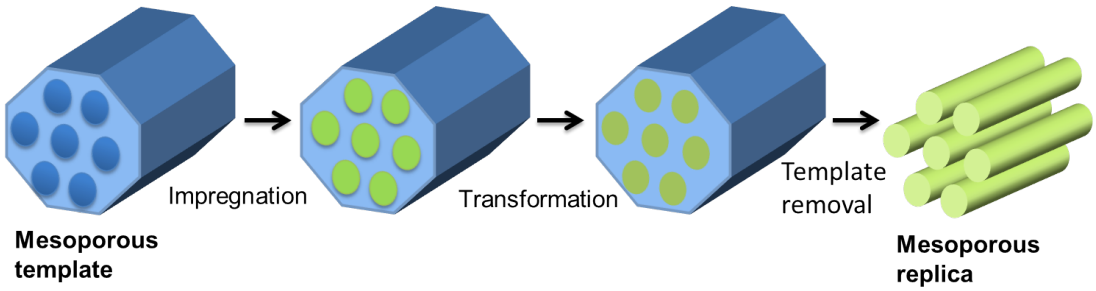

Figure 2.6.: Schematic illustration of the single steps during hard-templating (nanocasting) to obtain mesoporous materials.

Secondly, the precursors are impregnated into the template. In the mostly used wet impregnation approach the liquid precursor, either as a melt or dissolved in a solvent, gets into the pores by capillary forces. As the solvent evaporates it does so faster outside of the templates forcing the remaining liquid into the pores.[110] Full impregnation, however, is not easily achieved due to limited wetting of the surfaces.[111] An incomplete filling may lead to a structural instability in the product.[21] Another requirement is that the precursor does not react with the template, as this would destroy the integrity of the structure. In the next step the precursor transforms into the product. This can either happen by calcination like in most cases or any other chemical reaction. For example, when mesoporous silica is used as template direct calcination in air is possible whereas inert gas has to be used for oxygen sensitive materials or carbon templates.[103,104] During the final step the template gets removed. For this the reactivity of both the template and the product has to be considered. When a silica framework was utilized it can either be dissolved in HF[102,112] or NaOH.[21] In case of a carbon-template it can be burned away in air.[74]

One major drawback of the nanocasting method is that the synthesis is rather cumbersome and costly. Especially, as the template has to synthesized prior to the reaction itself. Moreover, the removal of the templates is arduous and limits the choice in materials.[24]

3

Synthesis and catalytic performance of vanadium oxide nanoparticles

3.1. Abstract

Vanadium oxides nanoparticles are promising catalysts and enzyme mimetics as vanadium is present in many enzymes. Vanadium(IV) oxide nanoparticles, however, have not been investigated as such. Here we describe a hydro-/solvothermal method to obtain VO_2(B) nanorods as well as VO_x nano-urchins and sheets. On that account it was examined how the water:ethanol ratio influences the morphology and composition. At high water concentrations, rod-shaped VO_2 nanoparticles formed whereas high ethanol amounts led to VO_x sheets and pure ethanol yielded VO_x nano-urchins. Additionally, alcohols with different chain lengths were used as solvent and surfactant. The morphology of the nanoparticles changed from urchin-like to sheets with increasing chain length due to steric hinderance. The catalytic activity of the vanadium oxide nanoparticles was assessed for the peroxidase activity in the oxidation of 2,2´-azino-bis(3-ethylbenzothiazoline-6-sulphonic acid) (ABTS). All vanadium(IV) oxide nanoparticles showed promising peroxidase activity which was the highest for the VO_x nano-urchins. The surface area of the VO_2 nanorods and VO_x nano-urchins and sheets was determined with BET. Subsequently, the catalytic activity of the vanadium oxide nanoparticles was related to their surface area.

3.2. Introduction

Vanadium oxide nanoparticles have garnered great interest over the last years, as they have versatile applications in catalysis,[113–115] as thermochromic/elctrochromic/electro-

optic devices,[116,117] electrodes for lithium/sodium ion batteries,[118–120] gas sensors,[121] supercapacitors[122] and electrochemistry.[123] Recently nanoparticles have also been investigated as enzyme mimics due to their similar sizes, reactivity and same metals as in the active centers of enzymes.[124,125] Compared to enzymes nanoparticles have the advantage of longer half life time, lower cost and higher chemical stability.[126] Among nanopmaterials Fe_3O_4[127] and Au[128] nanoparticles show promising enzyme mimetic properties. Another likely candidate for enzyme mimetic behavior are vanadium-based nanoparticles. Vanadium is in the active center of many enzymes like peroxidases, haloperoxidases and nitrogenases.[129–132] This is due to the fact that vanadium can readily change between different oxidation states. Thus vanadium can participate in redox-reactions. André et al.[113] successfully demonstrated, V_2O_5 nanowires exhibit halo- and peroxidase activity. Yet, the catalytic activity of other vanadium oxides has not been examined. Well known for many applications[114,133] VO_2 nanoparticles hold promise to act as enzyme mimetics as well.

Generally, there are many parameters that factor in the catalysis of nanoparticles such as structure, surface area, shape/morphology, wetting of the surfaces and interface interactions.[28,31,134–137] This myriad of factors complicates the systematic study of nanoparticle systems. However, one of the key parameters in catalysis is the accessible surface area that is always cited for the high reactivity of nanoparticles, as the catalysis occurs on the surface of the particles.[28] Despite this fact, the actual surface area of the nanoparticles is rarely determined. In most cases the catalytic activity is plotted over the concentration disregarding that only the surface atoms are available for the reactions. Therefore it is worthwhile to directly correlate the actual surface area of nanoparticles with their catalytic properties to determine the impact of the surface area.

There are several reported methods for the synthesis of VO_2 as well as for other vanadium oxide nanoparticles. The most common way to synthesize vanadium oxide nanoparticles are hydrothermal and solvothermal routes[138–141] (see also chapter 2). Solvothermal synthesis are versatile as they have many tunable experimental parameters such as temperature, solvent, precursor, capping agents[142] which can all determine the shape of the synthesized nanoparticles. In particular, the choice of solvent controls the reactivity, solubility and diffusion of the precursors.[143] In binary mixed solvents these factors can be tuned accurately which leads to different morphologies when the volume ratio of the solvents is varied.[144] Thereby vanadium oxide nanoparticles with different shapes e.g. spheres,[138,145] rods,[146–149] sheets[141,150] and urchin/flower-like[151–154] can be obtained. The most promising structures in terms of high surface areas are the sheets and urchin-like particles. In many cases, however, the size of those particles exceed

several hundreds of nanometers leading to a relatively small surface area. Thus it is a major challenge to synthesize urchins in the nanometer regime. As a consequence a synthesis of nanometer-sized urchins and sheets is highly desirable to increase the surface area. For this purpose the reactivity has to be finely adjusted to avoid uncontrolled growth to larger particles.
This chapter describes the synthesis of VO_2(B) nanorods and VO_x nano-urchins and sheets *via* a versatile solvo-/hydrothermal route. On that account the influence of the solvent composition is systematically investigated in regard of the nanoparticle morphology and phase. The solvent composition, namely the water:ethanol ratio, has a pronounced effect on the particle morphology. The morphology changes from rods over sheets to urchins with an increasing ethanol amount. Additionally alcohols with varying chain lengths are employed as solvent capping agents. The parameters of the VO_x nano-urchin formation are investigated more closely in the terms of temperature and Pluronic F127 concentrations. The VO_x nano-urchins are heat treated to obtain V_2O_5 nanoparticles with different morphologies. Furthermore the catalytic activity of the VO_2(B) nanorods and VO_x urchins and sheets is studied using 2,2´-azino-bis(3-ethylbenzothiazoline-6-sulphonic acid) (ABTS) as model substrate for the peroxidase activity. Revealing all investigated vanadium oxide nanoparticles possess a peroxidase-like activity. Then the surface area of the sheet, rods and urchin-shaped vanadium oxide nanoparticles is determined using BET which reveals a pronounced effect of the surface area on the catalytic activity.

3.3. Experimental Section

Materials All starting marterials were used without further purification or treatment. Pluronic F-127, Vanadyl acetylacetonate (98%, $VO(acac)_2$), ethanol (p.a.), 1-propanol (p.a.) and 1-octanol (≥99%) were purchased from Sigma Aldrich. Benzyl alcohol (BzOH, 99%) and 1-dodecanol (98%) were obtained from Acros Organics. The used tert-butanol (99%) was purchased from abcr.

Synthesis

Synthesis of VO_2(B) nanorods In a typical synthesis 150 mg of Pluronic were dissolved in 5 mL of ethanol before 140 mg of $VO(acac)_2$ were added and stirred for 3 h. The solution was poured into 20 mL water in a 50 mL Teflon-lined autoclave and kept at 453 K for 24 h. The product was separated by centrifugation (15 min, 9000 rpm) and further purified by washing with 15 mL ethanol. Then the nanoparticles were precipitated by centrifugation, dried in a vacuum oven at 313 K for 12 h. The product was stored at ambient temperature.

Synthesis of VO_x sheets After 150 mg of Pluronic F127 were dissolved in 24.7 mL of ethanol, 140 mg of $VO(acac)_2$ were added and the solution was stirred for 4 h. Then 0.3 mL of water were added and the solution was transferred into a 50 mL Teflon-lined autoclave and kept at 453 K for 1 d. When the content was cooled to ambient temperature the product was centrifuged (15 min, 9000 rpm). In a final washing step 15 mL of ethanol were added to the nanoparticles and the product was collected by centrifugation (15 min, 9000 rpm). Subsequently, the product was dried in a vacuum oven (313 K) for 10 h.

Synthesis of VO_x urchins Typically, 150 mg of Pluronic F-127 were dissolved in 25 mL of ethanol prior to the addition of 140 mg of $VO(acac)_2$. After stirring for 4 h the solution was given into a 50 mL Teflon-lined autoclave and heated to 453 K for 24 h. The obtained product was precipitated by centrifugation (9000 rpm, 15 min) and washed with 15 mL ethanol once before the particles were precipitated again by centrifugation (15 min, 9000 rpm). For storage the nanoparticles were dried in a vacuum oven (12 h, 313 K) and stored at ambient temperature.

Synthesis with dodecanol Pluronic F127 (150 mg) were dispersed in 25 mL of dodecanol (25 mL) in a water bath at 313 K. Then 140 mg of $VO(acac)_2$ were added and the

solution was stirred for 4 h at the same temperature. Subsequently the reaction mixture was transferred into a 50 mL Teflon-lined autoclave and heated to 453 K for 24 h. The brown product was precipitated by centrifugation (9000 rpm, 10 min) and washed with 15 mL of ethanol.

Heat treatment of the VO_x urchins The dried VO_x were heated to 453 K in a corundum boat with a heating rate of 2 K/min. This temperature was kept for 4 h before the sample was allowed to cool down at a rate of 2 K/min.

Materials characterization

TEM, HRTEM, EDX Nanoparticles were characterized by transmission electron microscopy (TEM) using a Philips EM420 instrument with an acceleration voltage of 120 kV. Alternatively a Zeiss LEO 906e was used. For sample preparation a dilute ethanolic suspension of the nanoparticles was deposited on a carbon coated copper grid. High resolution (HR) TEM images, and energy dispersive X-ray (EDX) spectroscopy images were acquired on a FEI Tecnai F30 S-Twin microscope with a 300 kV field emission gun.

X-ray Diffraction X-ray diffraction patterns were recorded with a Bruker AXS D8 Discover diffractometer equipped with a HiStar detector using graphite monochromatized Cu Kα radiation. Samples were glued on top of glass using a VP/VA copolymer (vinylpyrrolidone/vinylacetate) solution in isopropanol. Crystalline phases were identified according to the PDF-2 database using Bruker AXS EVA.[155]

X-ray Photoelectron Spectroscopy The samples were measured with an ESCA from PREVAC equipped with an SCIENTA R4000 X-ray photoelectron spectrometer using Mg Kα radiation (330 W, 15 kV, 22 mA).

Infrared and Raman Spectroscopy Fourier-transformed infrared (FT-IR) spectra were measured on a Bruker Tensor 27 spectrometer. The samples were prepared in a KBr pellet. Raman spectra were recorded using a Horiba Jobin Yvon LabRAM HR 800 spectrometer equipped with a CCD-detector. Further the Raman spectrometer was coupled to an Olympus BX41 optical microscope applying 50x magnification with a slit width of 100 μm. A HeNe laser with a wavelength of 632.8 nm and a spotsize of 2×2 μm was employed for excitation.

N_2 sorption experiments Nitrogen sorption experiments were performed using a Quantachrome autosorb 6B instrument using N_2 as the adsorbate at 77 K. The multipoint Brunauer-Emmett-Teller (BET) method was used to determine the specific surface area. Before analysis the samples were dried in a vacuum oven at 313 K for 12 h.

Peroxidase activity The peroxidase activity of the VO_2 nanorods, VO_x nano-urchins and sheets as well as bulk V_2O_5 was determined spectrophotometrically using 2,2´-azino-bis(3-ethylbenzothiazoline-6-sulphonic acid) (ABTS) as an electron donator by measuring the formation of the radical ABTS cation at 405 nm (ϵ_{420nm}=36.8 mM^{-1} cm^{-1})[156] on a Cary 5G UV-IS-NIR spectrophotometer (Varian Inc., Palo Alto, CA, USA) after hydrogen peroxide (H_2O_2) addition.[113] Typically, the peroxidase activity was measured in Milli-Q water by varying the concentration of the analyte (0-5 μg/mL) and keeping the concentrations of ABTS (0.5 mM) and H_2O_2 (0.2 mM) constant for 120 s at 298±2 K. The slight background reactions between the nanomaterials and ABTS as well as H_2O_2 and ABTS were determined and subtracted from the obtained reaction rates. Mean values of the initial ABTS oxidation rates of three traces were used in the calculations.

3.4. Results and Discussion

3.4.1. Influence of the solvent composition

There are many reaction parameters that influence the shape, phase and composition of nanoparticles in solvothermal reactions (see chapter 2.3.3). Here we elaborate the influence of the used solvent or solvent composition, respectively,[15,143] on the morphology of vanadium oxide nanoparticles. It has been reported that the solvent plays a crucial role in the shape evolution of nanoparticles.[141,157] Therefore, different mixtures of water and ethanol were employed to synthesize vanadium oxide nanoparticles while the other parameters (reaction time, temperature, amount of Pluronic and precursor concentration) were kept constant.

Morphology The morphology in dependence of the solvent composition is monitored using TEM as shown in Figure 3.1. The water:ethanol ratio was varied systematically between pure water and pure ethanol. Figure 3.1a depicts the nanoparticles obtained in pure water. There are nanorods with a highly polydispers aspect ratio. The length of the rods alters between 150 nm and several microns whereas the width is between 20 nm and 200 nm. When a water:ethanol ratio between 4:1 (20 mL:5 mL) (Figure 3.1b)

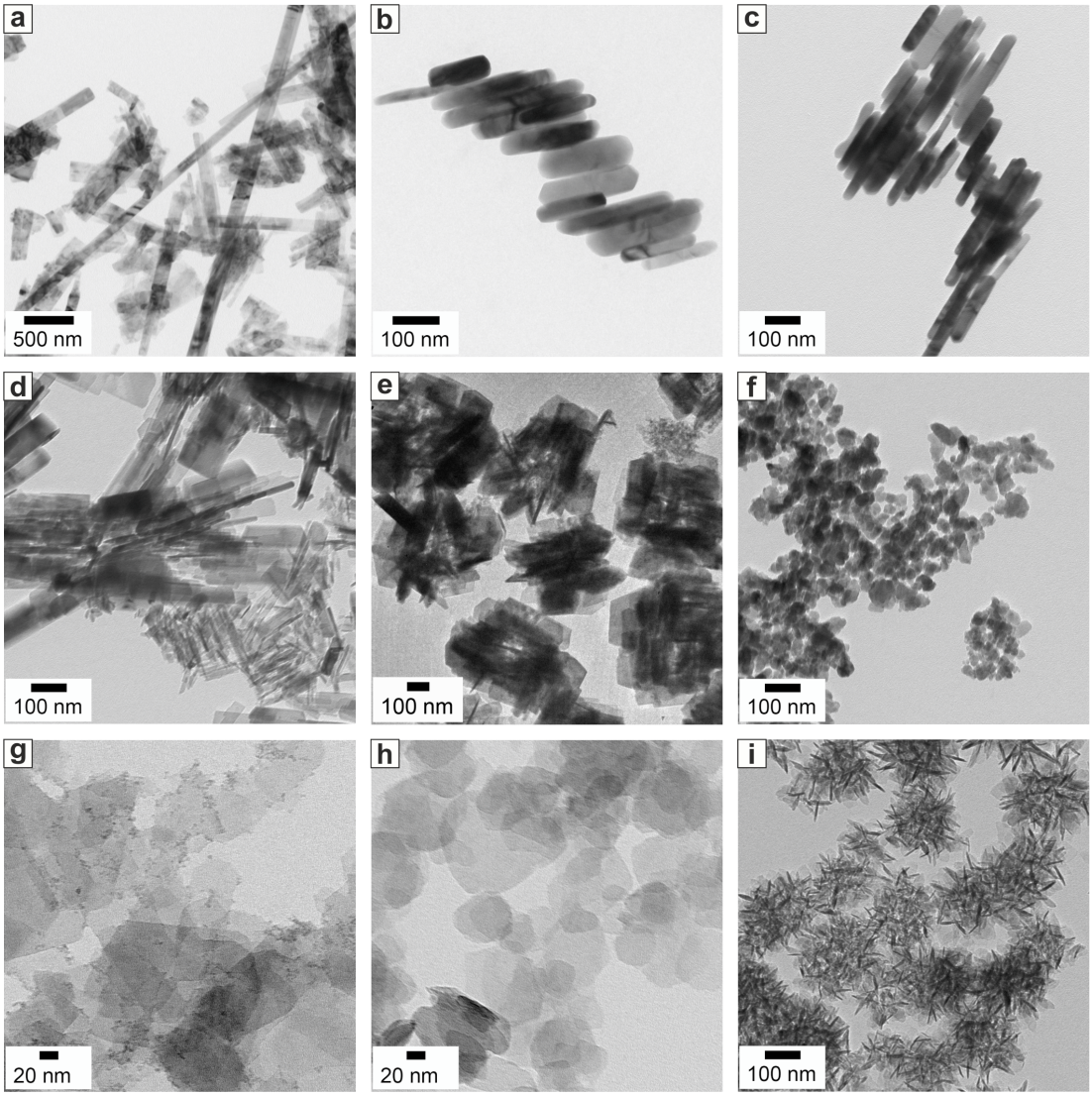

Figure 3.1.: TEM micrographs of the reaction products with different water:ethanol ratios. a) 25 mL:0 mL b) 20 mL:5 mL c) 15 mL:10 mL d) 10 mL:15 mL e) 5 mL:20 mL f) 2.5 mL:22.5 mL g) 0.5 mL:24.5 mL h) 0.3 mL:24.7 mL and i) 0 mL:25 mL water:ethanol.

and 3:2 (15 mL:10 mL) (Figure 3.1c) is used nanorods are formed as well. Those rods, however, are distinctly smaller and less polydispers than the ones in pure water. The width of the rods is in the range between 20 nm and 80 nm and the length between 100 nm and 220 nm. There is no discernable difference in the nanorod morphology for mixtures between a 4:1 and 3:2 water:ethanol ratio. The particles remain rod shaped with an increasing ethanol concentration. Albeit the polydispersity rises again as is demonstrated for a water:ethanol ratio of 2:3 in Figure 3.1d. In contrast the rods agglomerate into disordered bundles for a 1:5 ratio which is depicted in Figure 3.1e. At a water:ethanol ratio of 1:9 the nanoparticles are no longer rod shaped but more isotropic although without a distinct shape (see Figure 3.1f). A significant morphology change occurs at high ethanol (above water:ethanol 1:49) concentrations. In that case plate- or sheet-like nanoparticles with a narrow size distribution are obtained which are shown in Figure 3.1h and Figure 3.1g. For the latter there are some remnant small nanoparticles reminiscent of the morphology gained with a 1:9 water:ethanol ratio (see Figure 3.1f). The dimension of those plates is about 50-70 nm in both cases. The thickness of the sheets can be determined from plates that are accidentally vertically oriented on the grid. It is about 5 nm. Figure 3.1 displays the nanoparticles synthesized in pure ethanol. They exhibit a morphology like a sea urchin. The size of the urchins is around 200 nm. The structure of the sea urchin shaped nanoparticles can be derived from the sheets which is illustrated in Figure 3.2. Basically, a single urchin consists of

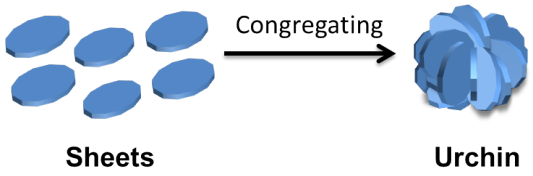

Figure 3.2.: Schematic representation of the morphological relation between the sheets and urchins.

multiple sheets that coalesce together disorderly. The driving force for this process might be the different colloidal stability of the sheets depending on the solvent. Additionally, the sheets that build up the nano-urchins seem to be smaller than the free standing ones which facilitates congregation.
In summary, three distinct morphologies, rods, sheets and urchins, can be synthesized by varying the water:ethanol ratio. Therefore, the solvent composition is a powerful tool to affect the shape of vanadium oxide nanoparticles.

Crystallinity Figure 3.3 summarizes the X-ray diffraction patterns of the products prepared with different water:ethanol ratios. X-ray diffraction patterns of the products prepared with water, and water:ethanol ratios between 5:1 and 1:4 exhibit the reflections of VO_2(B) (JCPDS 812392) see Figure 3.3 a-e. Some reflections have significantly sharper reflection profiles than others. This points to anisotropic crystallite sizes as the reflections become sharper with increasing crystallite size according to Scherrer´s formula. Anisotropic crystallite sizes are in good agreement with the rod-shaped morphology of the nanoparticles as depicted in Figure 3.1a-e where the reflections along the length of the rods are expected to be sharper. Further for the rods obtained in pure water as a solvent the reflections in the (00l) direction are weak. For the product with a water:ethanol ratio of 1:9 (see Figure 3.3f) the profiles of the X-ray diffraction pattern are distinctly broader and less pronounced than for VO_2(B) in Figure 3.3a-e. The main reflex, however, comes nearly at the same 2Θ value as VO_2(B) suggesting the product is VO_2(B) as well albeit with very poor crystallinity. The X-ray diffraction patterns of products with high amounts of ethanol, above a water:ethanol ratio of 1:49 (see Figure 3.3g-i), share the same reflections, except for the one at 15.7° 2Θ which is not present in the sample with pure ethanol. The matching reflections make it highly likely that those products share the same main crystalline phase, although the exhibited reflections are distinctly broad and weak. The broad reflections, however, fit to the morphology observed in the TEM images as shown in Figure 3.1g-i. Those samples consist of nanostructures with thin layers that either form sheets or urchins. It is typical for layered structures to have very broad reflections that merge into each other making it hard to allocate individual reflections. In addition, the overall crystallinity of the samples is weak leading to a high background. Therefore it is not possible to assign the crystalline phase of the products due to poor crystallinity of the sample and layered morphology. To conclude the change of the underlying motif in morphology observed using TEM from rods to layered structures is accompanied by different crystalline phases from VO_2(B) for the rods to a presumably layered structure.

Reaction parameters of the urchin formation

As the urchin-like VO_x nanoparticles have the most intriguing morphology of the synthesized nanoparticles, the reaction parameters of the nano-urchin formation are examined further in terms of temperature and influence of Pluronic F127.
The influence of the reaction temperature on the VO_x urchin formation is investigated using TEM. Figure 3.4 shows the reaction products obtained at 423 K and 473 K in

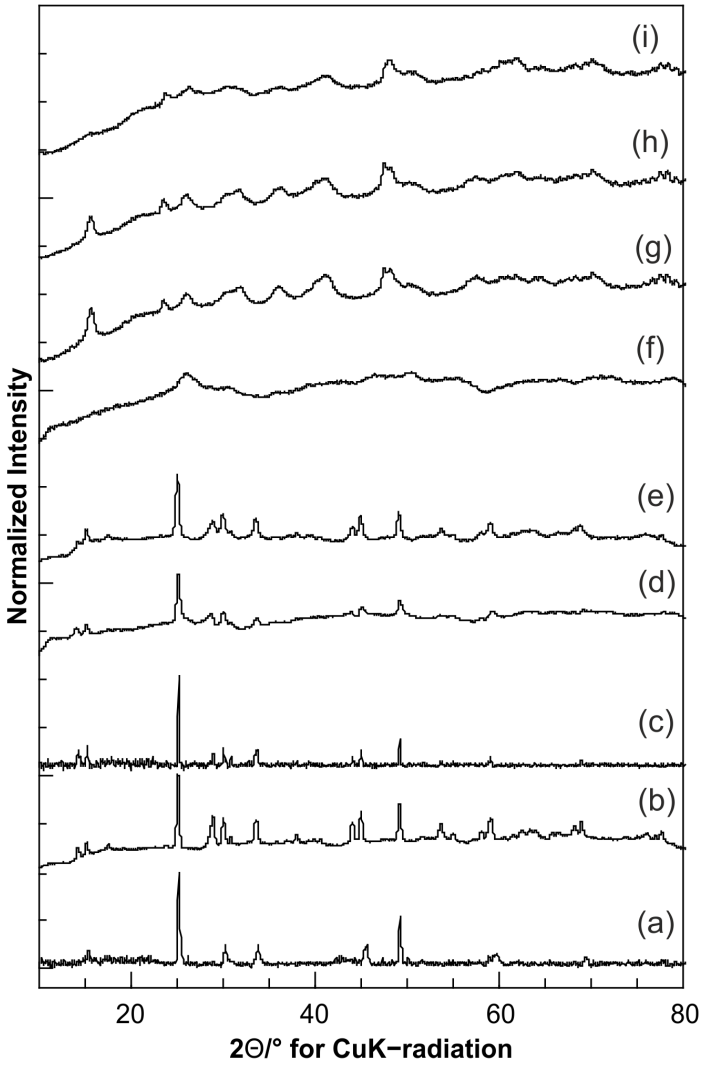

Figure 3.3.: X-ray diffraction patterns of the reaction products with different water:ethanol ratios. a) 25 mL:0 mL b) 20 mL:5 mL c) 15 mL:10 mL d) 10 mL:15 mL e) 5 mL:20 mL f) 2.5 mL:22.5 mL g) 0.5 mL:24.5 mL h) 0.3 mL:24.7 mL and i) 0 mL:25 mL water:ethanol.

Figure 3.4 a and b, respectively. The urchins synthesized at 453 K are depicted in Figure 3.1i. In all images VO_x urchins are in esse confirming temperatures as low as

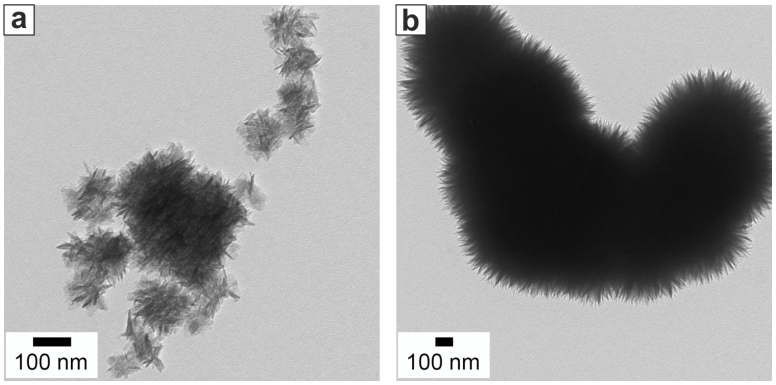

Figure 3.4.: TEM micrographs of the VO_x nano-urchin formation at different reaction temperatures, namely a) 423 K and b) 473 K.

423 K are sufficient for urchin formation. The size of the urchins, however, is dependent on the reaction temperature. At 423 K most of the urchins are small, below 100 nm, although there are also bigger agglomerates. The VO_x urchins enlarge with increasing temperature up to several microns and coalesce at 473 K due to a higher growth rate. On the other hand the spines/petals of the urchins nearly retain their size despite the temperature variation.

Moreover, the influence of the Pluronic F127 amount was determined with the aid of TEM. The products without and with 1000 mg of Pluronic F127 are depicted in Figure 3.5a and b. A TEM image of the urchins synthesized with 150 mg of Pluronic is displayed in Figure 3.1i. There are also flower-like nanoparticles with their typical petals

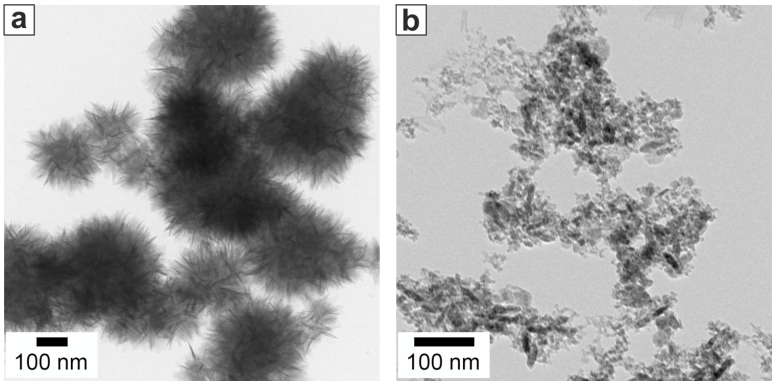

Figure 3.5.: TEM images of the VO_x nano-urchin formation in dependence on the amount of Pluronic F127 used. a) 0 mg and b)1000 mg of Pluronic F127.

without the aid of Pluronic. Yet, several nanoparticles tend to coalesce. This leads to multipod-shaped particles with petals. Thus Pluronic is not essential in the formation of the urchins but rather their stabilization against agglomeration. In contrast, very high concentrations of Pluronic F127 (1 g) disrupt the nano-urchin formation. Instead ill-defined particles without any particular morphology are obtained that are obviously smaller than the urchins.

Heat treatment of the urchins

There are several reasons to heat treat nanoparticles. For example, the crystallinity usually improves upon heat treatment which is desirable for weakly crystalline particles like the urchins. When the heating is done in air nanoparticles can be oxidized leading to other oxides either retaining or changing the morphology of the pristine particles.
The morphology change upon heat treatment is monitored with TEM as depicted in Figure 3.6a and b. After heating to 453 K for 3 h (heating rate 2 K/min) the morphology of the product resembles balls of paper (see Figure 3.6a). Basically, the petals of the as synthesized nano-urchins have started to roll up and sinter together retaining their approximate shape. The same morphology is obtained when the sample was heated to 523 and 623 K for 3 h. In contrast rod-shaped nanoparticles with a short aspect ratio are obtained when the sample is heated to 723 K for 3 h with a heating rate of 2 K/min. The X-ray diffraction patterns of the heat treated samples are illustrated in Figure 3.6c. Both products show the reflections typical for V_2O_5 (JCPDS: 01-0777-2418), see tic marks at the bottom of Figure 3.6c. The reflections are sharper and more pronounced for the product heated to 723 K which is typical for higher annealing temperatures. Further, the sharper reflections are in good agreement with the observed particle morphology as the rods are bigger than the product heated to 423 K. To conclude, the diffractograms confirm a phase transition of the VO_x urchins to V_2O_5 at temperatures as low as 423 K.

3.4.2. Influence of the type of alcohol used

The influence of the water:ethanol ratio on the morphology is discussed in chapter 3.4.1. When ethanol is used as a solvent nano-urchins are obtained. In a next step the effect of different alcohols will be investigated as the chain length and bulkiness of the solvent molecules often plays a crucial role in particle morphology.[15,70,158] To determine the influence of the chain length linear alcohols are used which are ethanol, propanol, octanol and dodecanol. Tert-butanol was applied as a typical example of a bulky alcohol as was BzOH which is commonly used in the synthesis of various nanoparticles[71,159]

Morphology Figure 3.7 presents the TEM images of the vanadium oxide nanoparticles synthesized with different alcohols. As demonstrated before nanoflowers with many disordered petals are obtained (see Figure 3.7 a). When propanol is used as solvent the reaction also yields nanoflowers as depicted in Figure 3.7. These nanoflowers, however, are smaller and have fewer petals than the ones with ethanol. Further, the whole nanoparticles are smaller. Going to even longer alcohols such as octanol and dodecanol there are no nanoflowers as illustrated in Figure 3.7c and Figure 3.7d, respectively. Instead, sheets (around 100 nm) are formed for octanol, whereas crumpled sheets are obtained in dodecanol. The structural evolution of the nanoparticles with increasing chain length of the alcohols is schematically illustrated in Figure 3.8. With growing chain length of the alcohols the steric hinderance gets more pronounced. With the alcohols attached to the nanoplates formed during the reaction limit how close two petals can get. Therefore there are less petals for propanol compared to ethanol as a solvent. For the longest alcohols the chain length is long enough to completely avoid congregation of the plates. This steric hindrance leads to isolated plates in case of octanol and dodecanol .The different petal sizes may be attributed to distinct reactivity of the $VO(acac)_2$ in different alcohols. For comparison alcohols with different sterics the bulky tert-butanol and BzOH were used as solvents as well. The obtained nanomaterials are depicted in Figure 3.7f and e respectively. When tert-butanol is used rod-shaped nanoparticles form that agglomerate into microparticles. In case of BzOH rod-shaped nanoparticles are obtained as well. The length of the rods is polydisperse. In contrast to the rods with tert-butanol the amount of agglomeration is lower. These results show that the sterics of the solvent plays a crucial role in nanoparticle morphology. Depending on the alcohol either two- or one-dimensional nanobuilding blocks make up the obtained nanomaterials.

Crystallinity For further characterization X-ray diffractograms are recorded from the products obtained with different alcohols as solvents. The X-ray patterns are summarized in Figure 3.9. The X-ray patterns of the products obtained with ethanol, propanol and octanol exhibit the same broad reflections which can be seen in Figure 3.9a-c. As discussed in chapter 3.4.1 it is not possible to assign the crystalline phase of the products unambiguously due to the broad reflections and poor crystallinity. Nevertheless the products have the same phase which is in good agreement with their similar morphology depicted in Figure 3.7 a-c. In case of dedecanol the diffraction pattern is very broad with some weak reflections that deviate from the reflections observed for short-chain alcohols (see Figure 3.9 d). Here it is not possible to assign a definite crystal structure due to the weak crystallinity and broad reflections. Both, the X-ray diffraction patterns of the products synthesized with tert-butanol and BzOH exhibit no reflections and can be described as amorphous. Altogether all products are only weakly crystalline (or amorphous) independent of the used alcohol.
To conclude, the chain length of the alcohols influences the morphology of the nanoparticles from nano-urchins to sheets probably due to steric influences. This morphology change is not connected to a phase transition as the nanoparticles have the same phase (with exception for dodecanol). For bulky alcohols like BzOH and tert-butanol different shapes are obtained and no crystalline phase can be observed. Thus the solvent has a clear influence on the particles morphology if not crystallinity.

3.4.3. Rods, Sheets and Urchins

The following subsection concentrates on the further characterization of the VO_x urchins, sheets and VO_2 rods as those nanoparticles have the most promising morphologies. Therefore, these nanoparticles are characterized using FT-IR, Raman, EDX, HR-TEM and XPS measurements.

FT-IR measurements Figure 3.10 shows the FT-IR spectra of the VO_2 nanorods,VO_x sheets and urchin-like morphology. For the rods the IR spectrum shows the strong edge-sharing V-O stretching vibration at $548\,cm^{-1}$ and the weaker V-O-V bending vibration at $924\,cm^{-1}$.[138,160] The remaining bands are very weak and that might be due to some remaining ligands at the surface. The IR spectra of the nano-sheets as well as the urchins share all bands and their relative strength to each other - albeit some bands are slightly shifted. Thus the urchins and sheets are chemically very similar with reference to their IR spectra. The edge-sharing V-O stretching vibrations cause the

band at 516 cm^{-1} for the sheets and at 524 cm^{-1} for the nano-urchins. Additionally the band at 1050 cm^{-1} is probably due to V=O stretching vibration in the nano-urchins and nano-sheets.[161] The CH_2 symmetric and asymmetric stretching bands of alkyl moieties appear at 2876, 2925 and 2973 cm^{-1}. Further, the bands at 898 cm^{-1} and 852 cm^{-1} might be assigned to the C-CH_3 stretching vibration. Compared with the nanorods the nano-urchins and sheets have a higher degree of organic moieties. Although the exact structure of the urchins and sheets is unknown, it can be ruled out that the IR spectra of the urchins as well as the sheets resemble those of the precursor $VO(acac)_2$. Both spectra are lacking the strongest bands of $VO(acac)_2$ at 1533 cm^{-1} and 1560 cm^{-1} that can be assigned to the C=C and C=O stretching bands (see Figure A.1 as reference FT-IR spectrum of $VO(acac)_2$).[162]

Raman measurements Furthermore, the VO_2 nanorods as well as the VO_x urchins and sheets are also characterized utilizing Raman spectroscopy as depicted in Figure 3.11. For the nanorods the Raman spectrum shows peaks at 283 as well as at 406 cm^{-1} that can be assigned to the V=O bending vibration. The band at 477 cm^{-1} belongs to the V-O-V bending vibration. Further, the broad peak at 526 cm^{-1} corresponds to the stretching mode of triply coordinated V_3-O. The V_2-O band is located at 695 cm^{-1} whereas the V-O stretching band appears at 878 cm^{-1}. Additionally, there is another peak at 929 cm^{-1} which is attributed to V^{4+}=O.[163] The strong Raman peak at 995 cm^{-1} is caused by the V=O stretching mode with a terminal oxygen.[164,165] Thus the Raman data corroborates that the rods consist of VO_2. The different signal-to-noise ratios between urchins and sheets on one hand and rods on the other hand, is attributed to varying filters. The sheets and urchins decompose at the measuring conditions for rods. Therefore the beam intensity is diminished for the sheets and urchins when the same was done for the rods no peaks were observed. As the crystalline structure of the sheets as well as the urchins is unknown it is difficult to assign bands unambiguously. Both, urchins and sheets, exhibit their strongest band at the same wavenumber namely 855 cm^{-1}. This position is typical of V-O stretching. Additionally, a weak band appears at 366 cm^{-1} which is caused by V-O bending modes.[166] In good agreement with the XRD and IR data the Raman spectra suggest the sheets and urchins have the same structure as they have the same characteristic peaks. The difference in full width at half maximum of the VO_x urchins and sheets is due to their respective morphology. The urchins show a higher degree of disorder as the petals are randomly oriented which leads in turn to a peak broadening in the Raman spectrum.

EDX and Electron diffraction For further characterization of the nano-sheets the composition is investigated using EDX as depicted in Figure 3.12a. The EDX confirms the presence of vanadium, oxygen, carbon and copper in the sample. The copper signal originates from the copper grid on which the sample is measured. Additionally, the carbon signal might be partially caused by the carbon coating of the grid. The carbon signal partly stems from the organic moieties that act as capping agents for the nanoparticles as the FT-IR spectrum of the sheets indicate the presence of alkyl groups (see Figure 3.10). Therefore the sheets themselves consist of vanadium and oxygen whereas the carbon is likely from the ligands surrounding the nanoparticles. Figure 3.12b shows a darkfield image of the nano-sheets with a size between 50 and 70 nm. Here upended sheets with a thickness of 5 nm can be observed. Some electron diffraction pattern of the nanoplates can be seen in Figure 3.12c and d. Figure 3.12c thereby depicts the patterns in plate direction. The distances are 6.6 and 23.8 Å with extinctions along the short axis. A diffraction pattern from the side of a platelet can be seen in Figure 3.12 and shows distances of 14.7 Å. Overall the reflections are very broad and the crystallinity is very poor additionally. Unfortunately it was not possible to determine the cell parameters of the VO_x sheets with electron diffraction, especially since the crystallinity is poor and the material is beam-sensitive. The sheets decompose under the beam. There is either bubble formation or hole etching like in Figure 3.12e (in the red circle) prohibiting a structure determination with electron diffraction.

XPS measurements XPS spectra of the nanorods, urchins and sheets are recorded in order to determine the oxidation state of the vanadium oxide in the nanoparticles. They are depicted in Figure 3.13. For XPS spectra the peak position is dependent on the oxidation state of the compound. The rods, urchins and sheets exhibit the vanadium 2p peak at the same energy namely 516.4 eV. Further, the oxygen 1s peak concurs at 530 eV for all of them. The matching peak positions suggest that the rods, urchins and sheets have the same vanadium oxidation state. Since the crystalline phase of the rods is known to be VO_2 from XRD and Raman investigations (see Figure 3.11 and Figure 3.3) the investigated samples have a V^{4+} oxidation state ,accordingly. Further the obtained energies are in good agreement with the literature values where vanadium 2p is 516.9 eV and oxygen 1s comes at 530 eV according to Mendialdua et al..[167]

3.4.4. Peroxidase activity

Vanadium is in the active center of various enzymes like haloperoxidases or peroxidases which catalyze a two-electron oxidation in a substrate utilizing hydrogen peroxide.[113,129,130] Therefore, vanadium oxide nanoparticles are likely candidates for the catalysis of peroxidase reactions. One established method to determine peroxidase activity is whether particles catalyze the oxidation of ABTS with the aid of of H_2O_2. Figure 3.14 illustrates the chemical structure of ABTS and the reaction scheme of its oxidation. Upon oxidation a metastable radical cation (II) is formed fast which will be referred to as radical ABTS cation. Slowly the radical ABTS cation disproportionates yielding the initial ABTS as well as an azodication (III). ABTS possesses an adsorption maximum at 340 nm while the radical ABTS cation has its adsorption maximum at 405 nm[168,169] and 652 nm in the presence of H_2O_2 which allows to monitor the reaction by means of UV-VIS spectroscopy.
In order to gauge the influence of the nanoparticles on the ABTS oxidation, UV-VIS spectra of ABTS are recorded after incubation with the VO_2 rods, VO_x urchins and sheets and subsequent centrifugation. These spectra are depicted in Figure 3.15a in comparison to an ABTS blank. All UV-VIS spectra show the typical absorption band of ABTS at 340 nm as well as the absorption of the radical ABTS cation in the 405 nm range. While ABTS gets oxidized the absorption at 340 nm drops and increases around 405 nm (see arrows). The UV-VIS spectra of the ABTS blank and the VO_2(B) sample are close together. In contrast there is a higher amount of the radical ABTS cation when VO_2(B) is applied as the adsorption is discernibly higher around 410 nm. In contrast the samples with the nano-urchins and -sheets both show a significantly lower adsorption at 340 nm and a higher adsorption at 405 nm compared to the ABTS blank. For further quantification a steady-state kinetic assay of the VO_x urchins, sheets as well as the VO_2 rods is measured which is shown in Figure 3.15b. Bulk V_2O_5 is used as reference as it has a reported peroxidase activity.[113] Here the reaction velocity (V_0) is plotted over the nanoparticle concentration which is varied between 0 and 5 μg/mL while the ABTS and H_2O_2 concentrations are kept constant. For the determination of the reaction velocity the formation of the radical ABTS cation is monitored at 405 nm and is converted regarding the extinction coefficient and Lambert Beer´s law. The reaction velocity rises with increasing vanadium oxide concentration for all samples. This rise shows that the reaction velocity is dependent on the the vanadium oxide concentration confirming the catalytic activity of all samples. Bulk V_2O_5 has the lowest ascent followed by VO_2(B) where the slope is considerably higher which is in good agreement with the observed

UV-VIS spectra. The slope is steeper for both the urchins and sheets with the highest rate for the urchins.

The surface areas of the nanoparticles and bulk V_2O_5 were determined using a multi-point BET measurement in order to relate the observed catalytic activities with their surface areas. The BET data is summarized in Figure A.2 in the appendix. For VO_2(B) nanorods the surface area is measured to be $21.7\,m^2/g$ which is in the typical size regime for nanorods.[170] In contrast the surface area for the urchins and sheets are distinctly higher with 124.6 and $73.9\,m^2/g$, respectively. Here the thin sheets with a high surface-to-volume ratio are responsible for the high surface values. Especially the surface area of the VO_x urchins is remarkably high compared with the surface areas reported in the literature for most of the flower- and urchin-like particles. For example, Xu et al.[154] synthesized urchin-like V_2O_3 particles with a surface area of $48.57\,m^2/g$ and Pan et al.[153] produced flower-like V_2O_5 with $33.64\,m^2/g$ surface area. The disparity in surface area is caused by the different overall size of the particles which is in the nanometer regime for the VO_x urchins whereas the other ones have sizes in the micrometer regime. Another factor is the thickness of the 'petals', the thinner the petals the higher the surface area. Pang et al.[151] obtained flower-like V_4O_9 microparticles with a surface area of $107.9\,m^2/g$ due to thin layers of 2 nm that form the flowers. Typically for nanoparticles their surface areas are much higher than the value for bulk V_2O_5 which is $8.4\,m^2/g$.

Thus taking the surface areas into account the catalytic activity increases with the surface area. The nanoparticles with the highest surface area, urchins and sheets, exhibit the highest rates (see Figure 3.15) while those for the rods and bulk V_2O_5 with smaller surface areas are lower. For quantification the reaction velocity was normalized to the surface area and plotted against the nanoparticle concentration. These steady-state kinetics are depicted in Figure 3.16. Here in contrast the lowest rate belongs to the VO_x urchins followed by that of the sheets. The rate is higher for bulk V_2O_5 and topmost for VO_2(B) nanorods. This findings highlight the strong influence of the surface area of the nanoparticles. The urchins and sheets are not such good catalysts in reference to a given surface area but this is overcompensated by their high surface area which gives them the highest activity overall. It is not possible to pinpoint which other factors are responsible for the difference in the activity between urchins/sheets and rods. Further, the catalytic activity of VO_2(B) is promising for a given surface area as it even surpasses that of V_2O_5.

3.5. Conclusions

To summarize, a new hydro-/solvothermal synthesis was established which yielded vanadium oxide nanoparticles with various morphologies. The impact of the water:ethanol ratio was investigated in terms of composition and morphology. At high water concentrations VO_2(B) nanorods are obtained, that are highly polydispers in pure water and gives the best results at a water:ethanol ratio between 4:1 and 3:2. In contrast, VO_x nano-sheets evolve, when a water:ethanol ratio of 1:9 is employed. In pure ethanol, VO_x nano-urchins form that can be described as congregated sheets. The reaction conditions for the urchin-formation were more closely examined in terms of reaction temperature and Pluronic F127 concentration. In a seperate step, the urchins were subjected to annealing which lead to V_2O_5 crumbled spheres and rods. The nanorods, sheets and urchins were characterized with TEM, IR, Raman, XRD and XPS.
Additionally, the influence of the solvent was investigated. For this alcohols with different chain lengths were used. With increasing chain length the morphology changes from urchin-like to sheets. The morphology change is likely induced by the steric hinderance of longer-chained alcohols. In contrast with bulky alcohols (tert-butanol) and BzOH rod-shaped vanadium oxide nanoparticles were obtained that tend to agglomerate.
In order to assess the catalytic activity, the peroxidase activity was investigated for the VO_x nano-urchins, sheets and VO_2(B) rods by oxidation of ABTS. All vanadium(IV) oxide nanoparticles exhibit peroxidase activity that is higher than for bulk V_2O_5. The VO_x nano-urchins thereby have the highest absolute peroxidase activity closely followed by the VO_x nano-sheets. As the surface area of nanoparticles is one of the key factors in catalysis the surface area of the vanadium oxide nanoparticles was determined using BET. The VO_x urchins and sheets have high surface areas of 124.6 and 73.9 m^2/g, respectively. In contrast, the rods possess a lower surface area of 21.7 m^2/g. Those surface area values are in good agreement with the impact of the surface area on the catalytic activity as the nanoparticles with the highest surface area show the highest activity. Then the peroxidase activity was normalized to the surface area of the rods that is distinctly higher than the similar activity of the urchins and sheets. This result confirms the strong effect of the surface area.

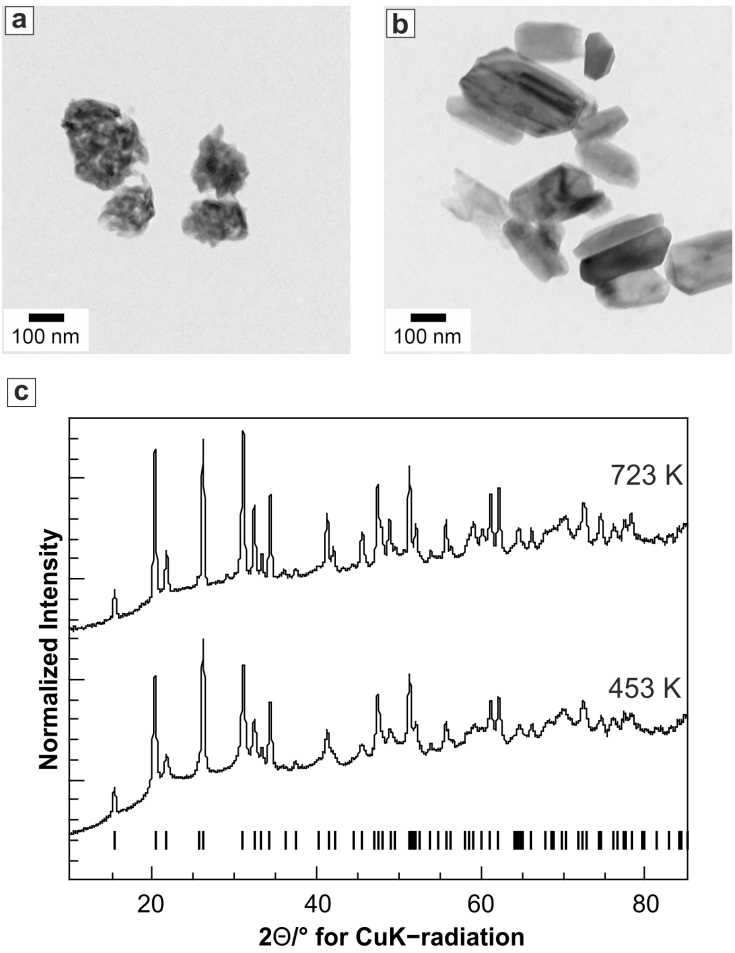

Figure 3.6.: TEM micrographs of the VO_x urchins heated with 2 K/min to a) 453 K and b) 723 K for 3 h each. c) X-ray diffraction pattern of the urchins heated to 453 and 723 K, respectively, and tic marks of V_2O_5 at the bottom.

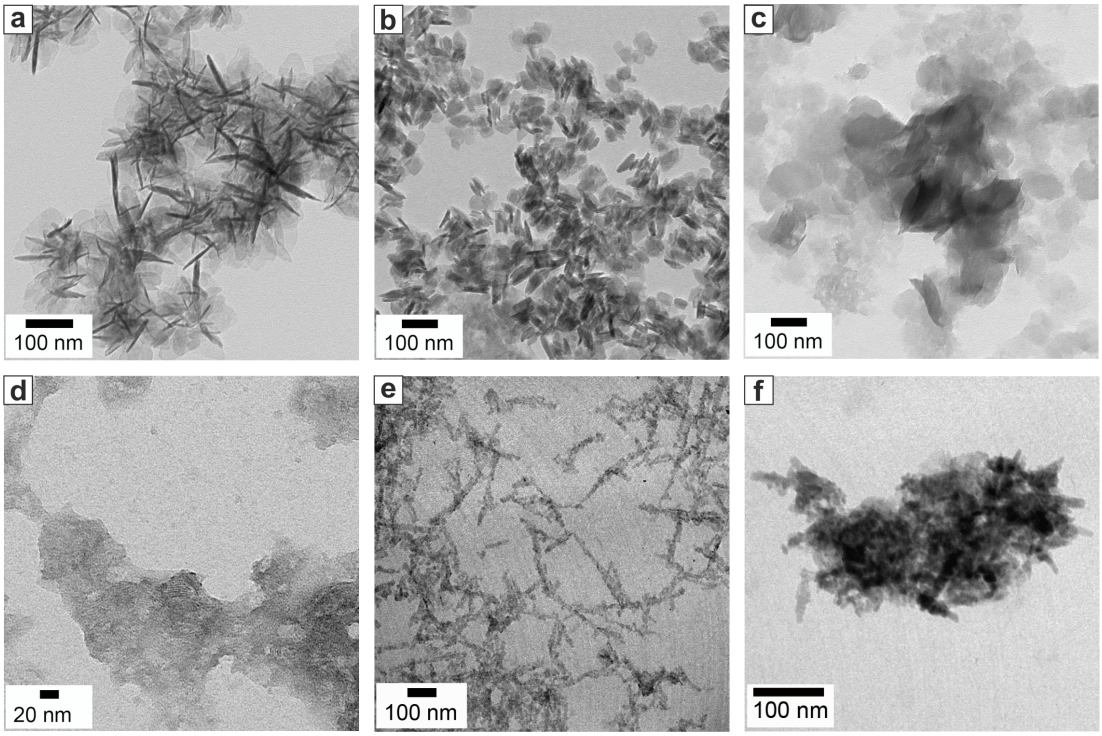

Figure 3.7.: TEM micrographs of the VO_x nanoparticles in dependence on the used solvent that is a) ethanol b) propanol c) octanol d) dodecanol e) BzOH f) tert-butanol.

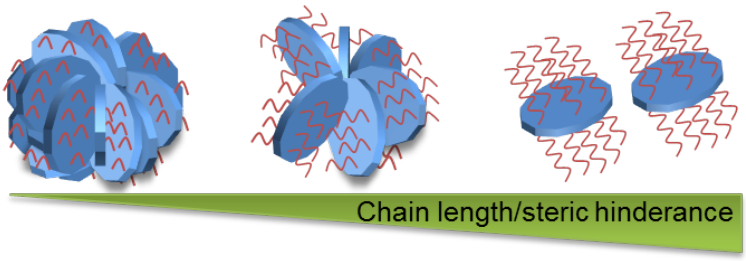

Figure 3.8.: Schematic illustration of the gradual morphology change of the VO_x nanoparticles from urchin-like to sheets obtained with alcohols having different chain lengths.

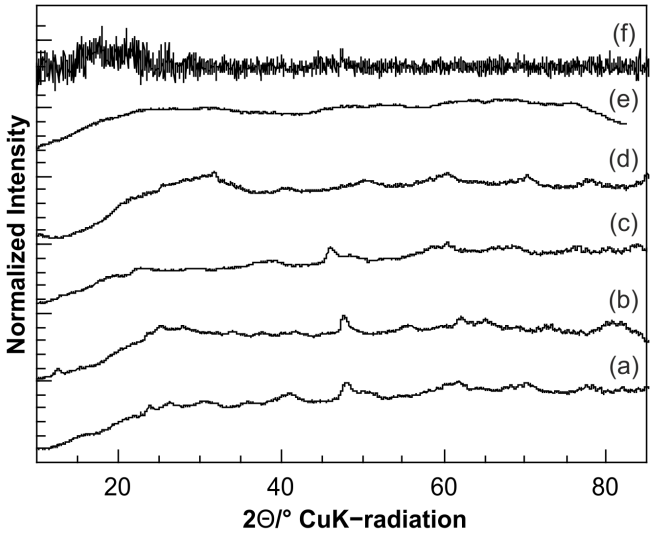

Figure 3.9.: X-ray diffractogramms of the reaction products obtained with different alcohols as solvents. a) Ethanol b) propanol c) octanol d) dodecanol e) BzOH and f) tert-butanol.

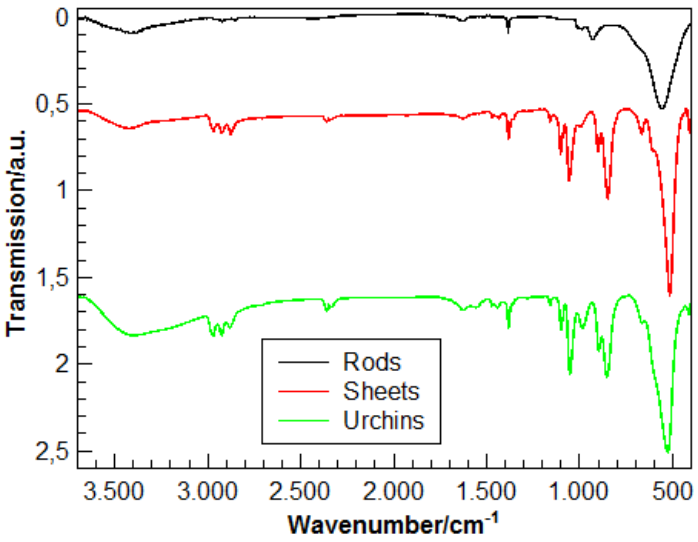

Figure 3.10.: IR spectra of the VO_2 nanorods (black), VO_x nano-sheets (red) and VO_x nano-urchins.

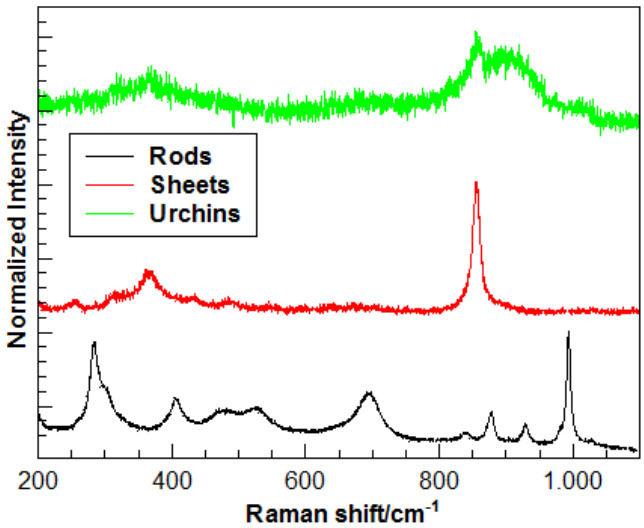

Figure 3.11.: Normalized Raman spectra of the VO_2 rods (black), VO_x nano-sheets (red) and nano-urchins (green).

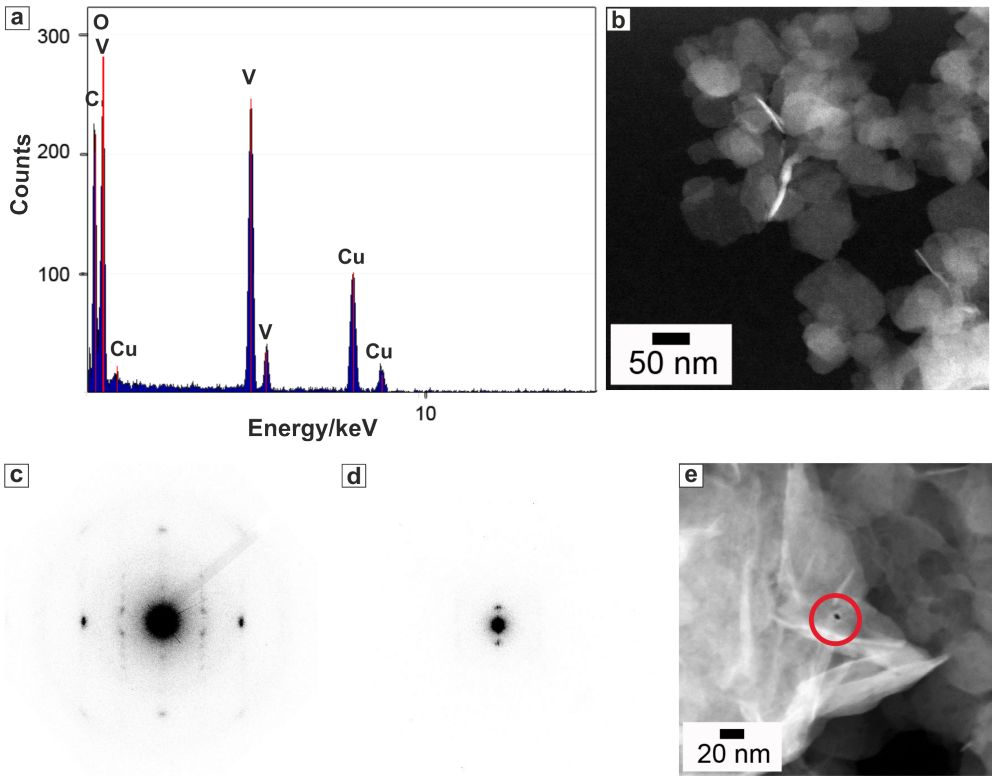

Figure 3.12.: a) TEM EDX and b) darkfield image c) and d) electron diffraction pattern and d) darkfield image showing radiation damage of the VO_x nano-sheets.

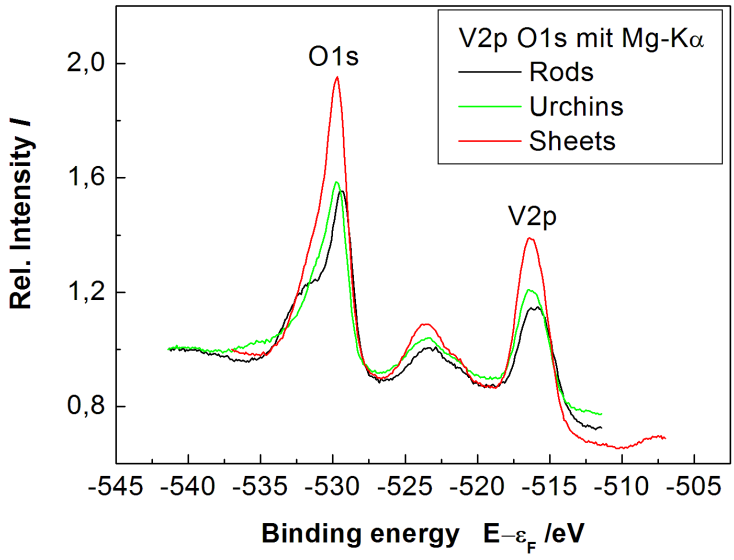

Figure 3.13.: XPS data of the VO_2 nanorods (black), VO_x nano-sheets (red) and nano-urchins (green).

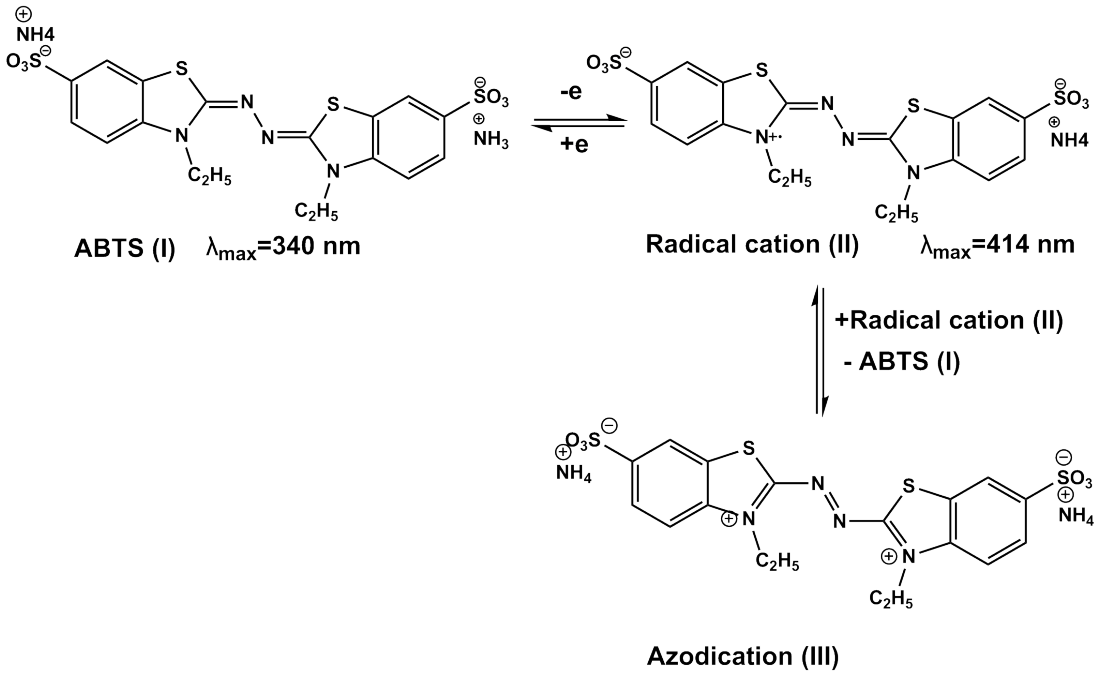

Figure 3.14.: Chemical structure of ABTS and its oxidation products and their emission maxima that occur during the ABTS oxidation with H_2O_2 according to Childs and Bardsley.[168]

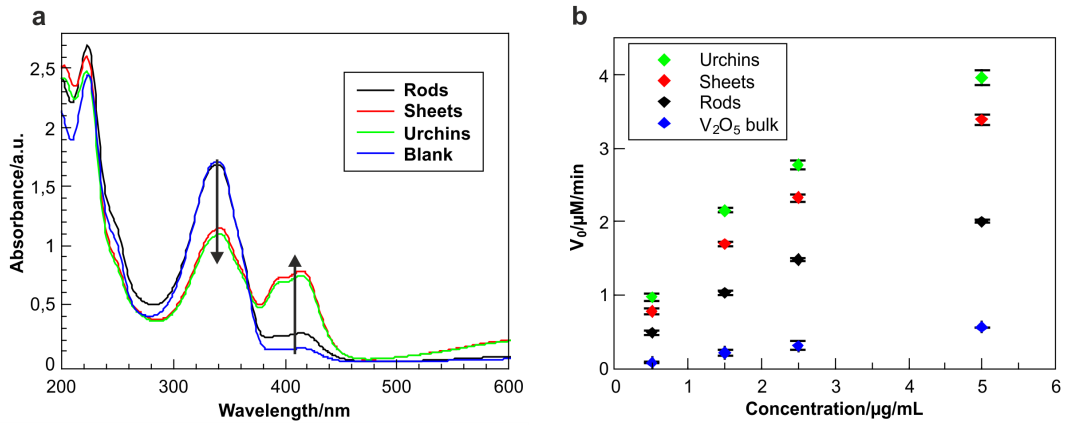

Figure 3.15.: a) Steady state kinetic study of VO_x urchins, sheets and VO_2 rods compared to bulk V_2O_5. The reaction rate is determined for different nanoparticle concentrations. b) UV-VIS spectra of ABTS (50 μL, 10 mM) with 20 μL H_2O_2 (10 mM) in 880 μL acetate buffer (pH=4, 100 mM) after incubation with 50 μL (1 mg/mL) VO_x urchins, sheets and VO_2 rods for 60 min and centrifugation as well as a blank without nanoparticles with the same concentration. (Diluted 1:10)

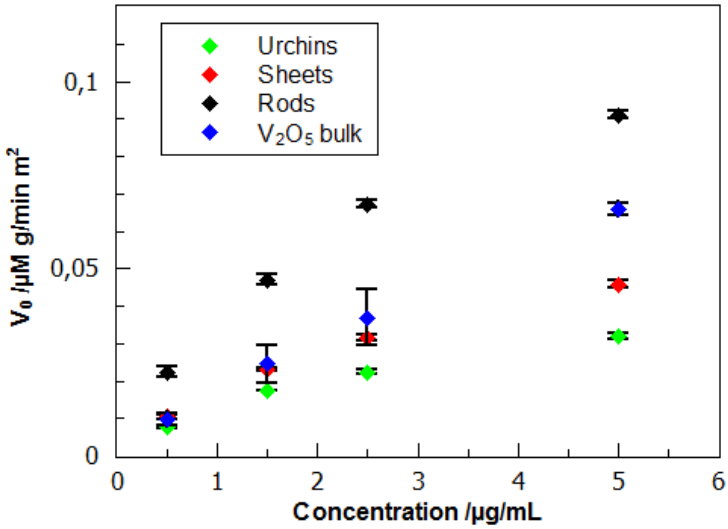

Figure 3.16.: Steady-state kinetic assay of VO_x urchin, sheets and VO_2 rods compared to bulk V_2O_5 by variation of the NP concentration normalized to the surface area.

4

Synthesis of crystalline tantalum oxide and tantalate nanoparticles and their photocatalytic behavior

4.1. Abstract

Alkali metal tantalates are of interest for applications in photocatalysis as well as in high temperature resistance or for capacitor dielectric materials. We have synthesized nano-sized Ta_2O_5 rods and $MTaO_3$ cubes (M=Na, K, Rb) hydrothermally and demonstrate the pH dependence of the synthesis of Tantalum oxide and tantalate nanoparticles. The morphologies of the nanoparticles range from particle agglomerates in acidic reaction media over rods at neutral pH to tantalate cubes in basic reaction media. Whereas there is no apparent influence of the base cation on the particle morphology, there is a pronounced effect on the particle composition. At high base concentrations cubic tantalate particles with a pyrochlore structure are formed. The pyrochlore structure allows a complete ion exchange through the tunnels in the structure by replacing the alkali metal ions by H^+ while retaining the particle morphology. The as-synthesized particles show promising photocatalytic properties.

4.2. Introduction

One of the challenging issues in nanotechnology is the ability to establish protocols for the scalable synthesis, and enhanced properties of nanoscale engineered advanced materials. Many improved pathways for the synthesis of such nanomaterials with tunable properties have been reported recently.[171] Among transition metal oxides, tanalum pentoxide (Ta_2O_5) has proven as a potential candidate in electronics and photoelectrics due to its high dielectric constant, high refractive index, low internal

stress and high resistivity.[172–174] Ta_2O_5 has also been used as an anti-reflection layer in solar cells and for nonlinear optical applications.[175] Moreover, it shows very good thermochromic properties, and its optical properties can be altered by raising the temperature. Furthermore, such systems can be employed in solid electrolyte fuel cells and waste water recovery.[176,177] However, unlike for other metal oxides, reports on a controlled synthesis of tanalum oxide in the nanoregime are scarce. Hydrothermal,[178–184] solvothermal,[159,185–187] sol–gel approaches[188,189] ultrasonic methods,[190] reactions in microemulsions,[61,191,192] and templating methods[193,194] have been applied to synthesize Ta_2O_5 and alkali metal tantalate ($NaTaO_3$ and $KTaO_3$) nanoparticles and powders.[195–201] The majority of the reported $NaTaO_3$ and $KTaO_3$ particles exceed the size of 100 nm. As a major drawback of most of these synthesis methods of nanoparticles is the lack of crystallinity of the tanalum oxide nanoparticles since only amorphous particles can be recovered. Therefore, these nanoparticles always require a thermal post-treatment above 873 K[185] to improve crystallization. Only recently Ta_2O_5 nanorods[178] and flowerlike Ta_2O_5 nanostructures[179] were obtained by a hydrothermal method using hydrofluoric acid. Hence, synthetic routes avoiding the use of toxic chemicals are highly desirable.

In this chapter a versatile hydrothermal method is introduced, which allows us to obtain crystalline Ta_2O_5 nanorods without further heat treatment. In addition, various cubic alkali metal (Na, K, Rb) tantalate nanoparticles are obtained, of which especially $Rb_2Ta_2O_6$ has not been reported before. Additionally, cubic Ta_2O_5 nanoparticles are synthesized *via* fast ion exchange of the tantalates and subsequent heat treatment. Moreover, we present a systematic study to evaluate the influence of the reaction pH value as well as the respective precursor base for the composition and morphology of the nanoparticles. The reactivity of the tantalates in terms of ion exchange is monitored, and the photocatalytic activity of the prepared materials is studied by monitoring the degradation of Rhodamine B (RhB) as a model substrate.

4.3. Experimental section

Materials All chemicals were used without further purification. Tantalum (V) ethoxide (99.98%), sodium hydroxide (pellets, p.a.), potassium hydroxide (flakes, p.a.), and rubidium hydroxide hydrate were purchased from Sigma Aldrich. Tantalum(V) *n*-butoxide (95%) and rubidium hydroxide solution (50 wt%, 99%) were obtained from ABCR, ethanol (p.a.) from VWR and a 0.1 N sodium hydroxide stock solution from Roth.

Synthesis

Synthesis of alkali tantalates with cubic morphology In a typical reaction 0.335 mL (0.80 mmol) of tanalum(V) *n*-butoxide was added to a beaker to 4 mL of ethanol. The sol was aged in a desiccator under a humid atmosphere by keeping a Petri dish containing water at the bottom of the desiccator over a period of 20 h. The formed gel was mixed with 20 mL of a solution containing 0.1 M of the alkali hydroxide (potassium hydroxide, rubidium hydroxide or sodium hydroxide solution, respectively). The resulting solutions were transferred into a 50 mL Teflon-lined autoclave and kept at 473 K for 60 h. Finally, the contents of the reaction vessels were cooled to room temperature, then the product was separated by centrifugation at 9000 rpm for 15 min. The obtained product was further purified by washing twice with 20 mL water each time.

Synthesis of $HTaO_3$ by ion exchange of the alkali tantalate nanoparticles The as-prepared samples were sonicated with 20 mL of (2 M) hydrochloric acid for 30 min, centrifuged, and washed with 25 mL water followed by 25 mL ethanol. The particles were dried *in vacuo* for 12 h.

Annealing of the $HTaO_3$ nanoparticles $HTaO_3$ nanocubes were heated to 1023 K over 3 h and maintained at that temperature for 12 h.

Synthesis of the Ta_2O_5 nanorods Ta_2O_5 nanorods were synthesized by gelation of tanalum(V) *n*-butoxide, carried out as described above for the synthesis of cube-shaped alkali tantalates. The formed gel was transferred to a 50 mL Teflon-lined autoclave together with 20 mL of a 5 mmol base solution, sealed, and kept at 473 K for 60 h. The resulting colorless solid was centrifuged (15 min, 9000 rpm) and washed twice with 20 mL water.

Annealing of the Ta_2O_5 nanorods The as-synthesized nanorods were dried using a vacuum line overnight, and subsequently heated to 1123 K in a corundum boat with a heating rate of 5 K per minute and kept there for 12 h.

Materials characterization

TEM, HRTEM, and EDX The nanoparticles were characterized by transmission electron microscopy (TEM) using a Philips EM420 instrument with an acceleration voltage of 120 kV. TEM samples were prepared by dropping a dilute ethanolic suspension of the nanoparticles on a carbon coated copper grid. High resolution (HR) TEM images, and energy dispersive X-ray (EDX) spectroscopy images were acquired on a FEI Tecnai F30 S-Twin microscope with a 300 kV field emission gun. TEM/HRTEM images and FFT patterns were acquired with a CCD camera (14-bit GATAN 794MSC). For a quantitative EDX analysis carbon coated gold or nickel grids were used to avoid the overlap of the Ta L-lines (11.67 – 7.173 keV) with the Cu K-lines (8.048 – 8.028 keV). EDX spectra were acquired and quantified with the Emispec ESVision software.

X-ray techniques Powder X-ray diffraction patterns were recorded with a Siemens D5000 diffractometer equipped with a Braun M50 position sensitive detector in transmission mode using Ge (200) monochromatized CuKa radiation. Samples were prepared between two layers of Scotch Magic. Phase analyses were performed according to the PDF-2 using Bruker AXS EVA 10.0. Rietveld refinements for quantitative phase analysis, determination of the composition and evaluation of crystallite sizes, respectively, were performed according to reported structure models using Topas Academic V4.1.[202] Reflection profiles were generated according to the fundamental parameter approach[203] applying a correction for anisotropic crystallite morphologies. Within this model individual crystallite (CS_h) sizes are computed for each reflection (hkl) according to the quadratic form $CS_h = 1/norm\{h^T \times C_{ij} \times h\}$ in which h is the reciprocal lattice vector corresponding to (hkl) and $C_{ij} = (a_i)^{\frac{1}{2}} \times (a_j)^{\frac{1}{2}}$ is the symmetric second rank tensor of the square roots of the crystallite dimensions in direction i and j in the basis of the crystal lattice. X-ray fluorescence (XRF) measurements were carried out on a PANalytical aXios 4 kW instrument using SuperQ/OMNIAN V 5.0D PANalytical B.V., Almelo, the Netherlands (2009). The samples (20 mg) were measured in a boric acid pellet (2 g) as matrix.

Photocatalytic measurements Freshly prepared solutions (0.5 mg/mL) of as synthesized nanoparticles mixed with rhodamine B (RhB) solution (0.001 mg/mL) were

irradiated under a 8 W UV-Lamp using UV light of wavelength λ= 254 nm and 366 nm. UV-VIS spectra were measured using a Cary Varian 5G UV-VIS-NIR spectrometer.

4.4. Results and Discussion

4.4.1. Influence of the pH value

In order to demonstrate the effect of pH on the morphology, various experiments were performed by changing the amount of added base (NaOH) while keeping all other parameters constant. This resulted in reaction pH values between pH=3 and pH=13. The products were characterized using TEM. TEM and representative overview TEM images shown in Figure 4.1 depict the particle morphologies in dependence on the pH value. In acidic media (pH=3 in Figure 4.1a) and pH=4 (see Figure 4.1b) a mixture of small needles along with big agglomerates were obtained. A snapshot after 12 h was taken which also yielded agglomerates. Therefore it is not possible to obtain non agglomerated nanorods at acidic pH. At pH=7 (Figure 4.1c) and pH=8 (in Figure 4.1d) rod-shaped nanoparticles were formed with a broad distribution of size and aspect ratio. The average width of the rods is about 9 nm for pH=7 and pH=8 whereas the length of the rods varies between 30 nm and 600 nm. In contrast to an acidic reaction medium there is no agglomeration of the nanorods at near neutral pH values. Both, Figure 4.1f and Figure 4.1g, show the cube-shaped morphology of the nanoparticles produced at pH=12 and pH=13. The cuboidal nanoparticles at pH=13 exhibit a higher polydispersity and are more distorted than the ones obtained at pH=12. Additionally the particles are smaller and have a mean length of 12±6nm (histogram see Figure A.3). In Figure 4.1e (corresponding to a pH value of 9) nanorods and parallelepiped-shaped nanoparticles coexist. Figure 4.1h compiles the NaOH concentrations used to obtain the different pH values in the reaction mixture before hydrothermal treatment. There is no change of the pH values during the reaction as confirmed by pH measurements before and after the reaction.

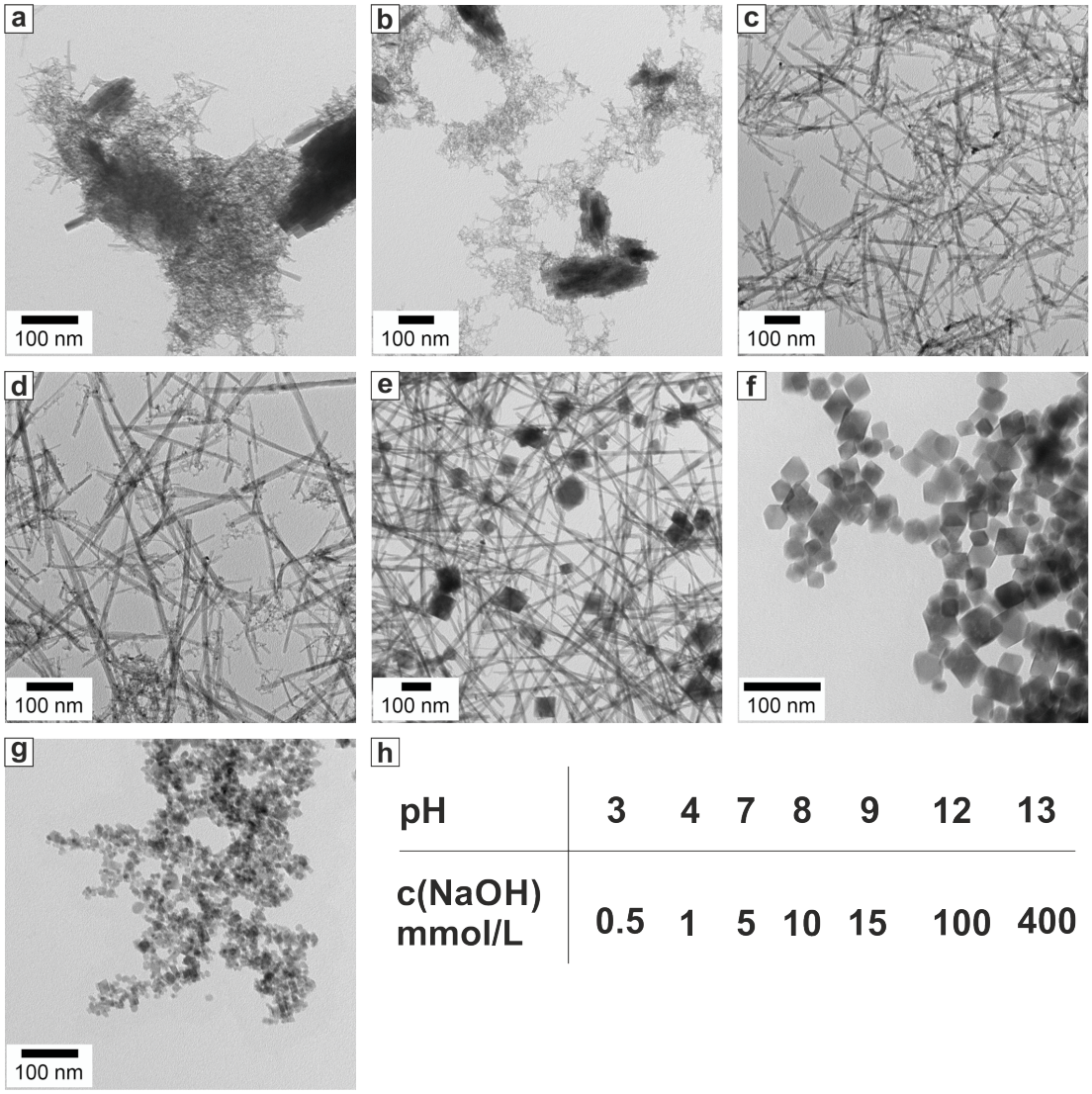

Figure 4.1.: (a-g) TEM micrographs of the tanalum oxide nanoparticles at different pH values. a) pH=3 b) pH=4 c) pH=7 d) pH=8 e) pH=9 f) pH=12 and g) pH=13. h) shows the pH values of the reaction mixtures before (and after) the hydrothermal treatment based on the NaOH concentration.

The X-ray diffraction patterns of the products obtained at different pH values are summarized in Figure 4.2. According to the X-ray diffraction investigations, that are depicted in figure 4.2 the crystalline products formed upon reaction at pH=3 and pH=4 are single phase Ta_2O_5. The (*00l*) reflections exhibit significantly sharper reflection profiles than reflections of general (*hkl*). This points to anisotropic crystallite sizes and was therefore taken into account in the corresponding refinements. The crystallite sizes determined this in this way are 41(1) nm in the *a,b* plane and 70(1) nm in *c* direction for the nanorods obtained at pH=3 and 47(1) nm in *a,b* plane vs. 75(1) nm in *c* direction for the nanorods obtained from the reaction carried out at pH=4. The X-ray diffraction patterns of the products prepared at pH-values of 7 and 8 exhibit still the reflections corresponding to Ta_2O_5. Yet, the profiles of the Ta_2O_5 phase are broader and in addition, very broad intensities of a non-identified phase appeared. X-ray diffraction patterns of the products prepared at pH values of 9, 12 and 13 exhibit the reflections of defect-pyrochlore-type tantalic acid "$HTaO_3$".[204] The product prepared at pH=9 is a mixture of tantalic acid with Ta_2O_5 (15(1) %wt, crystallite size 48(2) nm) whereas the one prepared at pH=13 is a mixture of tantalic acid with $NaTaO_3$[204] (17(2) %wt, crystallite size > 100 nm). The product prepared at pH=12 is single phase pyrochlore-type tantalic acid and exhibits the highest crystallinity within the series of different pH values, i.e. 47(1) nm at pH=12 vs. 33(1) nm at pH=9 and 21(1) nm at pH=13. The crystal chemistry and in particular the exact structure and composition of the defect-pyrochlore-type group V and VI metal acids is a complex matter that cannot be resolved from laboratory X-ray diffraction data of nanoparticular samples. On the other hand, the Rietveld refinements for the pH=9, pH=12 and pH=13 samples point to substantial amounts of sodium cations on the proton positions. The refinements were therefore performed assuming an idealized composition $H_{2-x}Na_{2x}Ta_2O_6$[2219]yH_2O with protons and sodium cations on the 16*d* site and water molecules of crystallization on the 8*b* site. At pH=9 virtually all protons are substituted (x=2.00(6)), increasing the pH value their amount decreases to x=0.84(1) at pH=12 and x=0.78(2) at pH=13, which are identical within 1σ. For further details see Table A.1 in the appendix. Kanhere et al. reported that a higher NaOH concentration favors the formation of perovskite $NaTaO_3$ over the pyrochlore $Na_2Ta_2O_6$ described in this work. The perovskite however appears only at base concentrations higher than the ones used in this work.
For large-scale synthesis reactions can be carried out in a 250 mL autoclave yielding up to 800 mg in one batch. Here the morphology of the products remains is unaltered by upscaling which is one of the advantages of hydrothermal reactions as previously discussed in chapter 2.3.3.

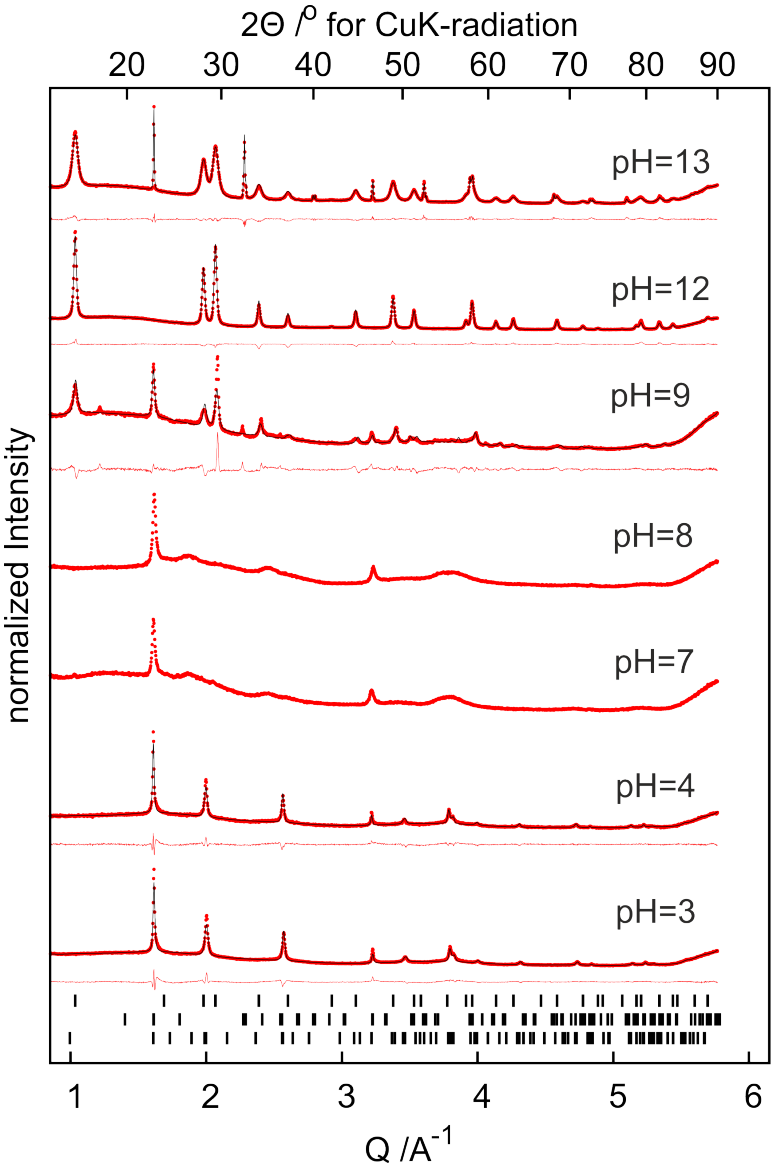

Figure 4.2.: X-ray diffraction patterns and corresponding Rietveld fits (red dots: observed intensity, black line: fit, red line: difference curve) of the products prepared at different pH values and corresponding tic marks of $HTaO_3$ (top), $NaTaO_3$(middle) and Ta_2O_5 (bottom).

In summary, there is a strong dependence of the morphology as well as the composition of the tanalum oxide species on the pH value. This influence can partially be understood as analogous to the Stöber process with silica. [205,206] The occurrence of agglomerates at low pH values can be assigned to a fast hydrolysis rate at low pH values compared to higher ones. Additionally the acidic surface of tanalum oxide facilitates the agglomeration of nanoparticles. With increasing pH the sodium concentration rises and the formation of sodium tantalate occured rather than that of tanalum oxide. The cubic unit cell of the nanoparticles is responsible for the cube-like morphology of the product instead of rods obtained at lower pH. Hence the pH value is a valuable tool for tuning the morphology of the product.

4.4.2. Influence of the base (counter cation) at pH=7 and pH=12

As we observed neutral or basic pH values of 7 and 12 resulted in the formation of well-defined nanorods and cube-shaped nanoparticles. Therefore these conditions were used to further explore the effect of the counter cation while keeping the other parameters constant. In order to evaluate the influence of the cation, NaOH, KOH and RbOH were used as precursor bases with concentrations of 5 mM and 100 mM, respectively. The pH value before and after the reaction was neutral for all used bases with a base concentration of 5 mM. When a 100 mM base solution was used the pH was 12 for all precursor bases, before and after the reaction. In order to clarify the phase composition of the as synthesized products with 100 mM NaOH, KOH and RbOH X-ray powder diffraction data were collected. The X-ray diffraction patterns shown in Figure 4.3 resemble that of the defect-pyrochlore tantalic acid. According to the Rietveld refinements (cf. Table A.2 in the appendix), the approximate composition of the samples is $Na_{0.88}H_{1.12}Ta_2O_6 \times 0.37\ H_2O$, $K_{0.97}H_{1.03}Ta_2O_6$ and $Rb_{0.2}H_{1.8}Ta_2O_6 \times H_2O$. XRF measurements were carried out to determine the ratio between the tantalates and tantalic acid in the nanoparticles. For details see Table A.3 in the appendix. For RbOH an atomic ratio of Rb:Ta of 1:1.27 was found. When KOH was used as a base to keep the pH constant, an K:Ta atomic ratio of 1:2.19 was obtained. The discrepancy between the compositions determined from the XRD and the XRF data indicates the principal limits of X-ray diffraction for the analysis of nanomaterials. TEM images (Figure 4.5) show the morphologies of the nanoparticles synthesized at pH 7 with 5 mM KOH (in Figure 4.5a) and RbOH (Figure 4.5c).
The powder X-ray patterns of products obtained with 5 mM NaOH, KOH and RbOH are summarized in Figure A.5 (see appendix). The crystalline phase of all rods is identical

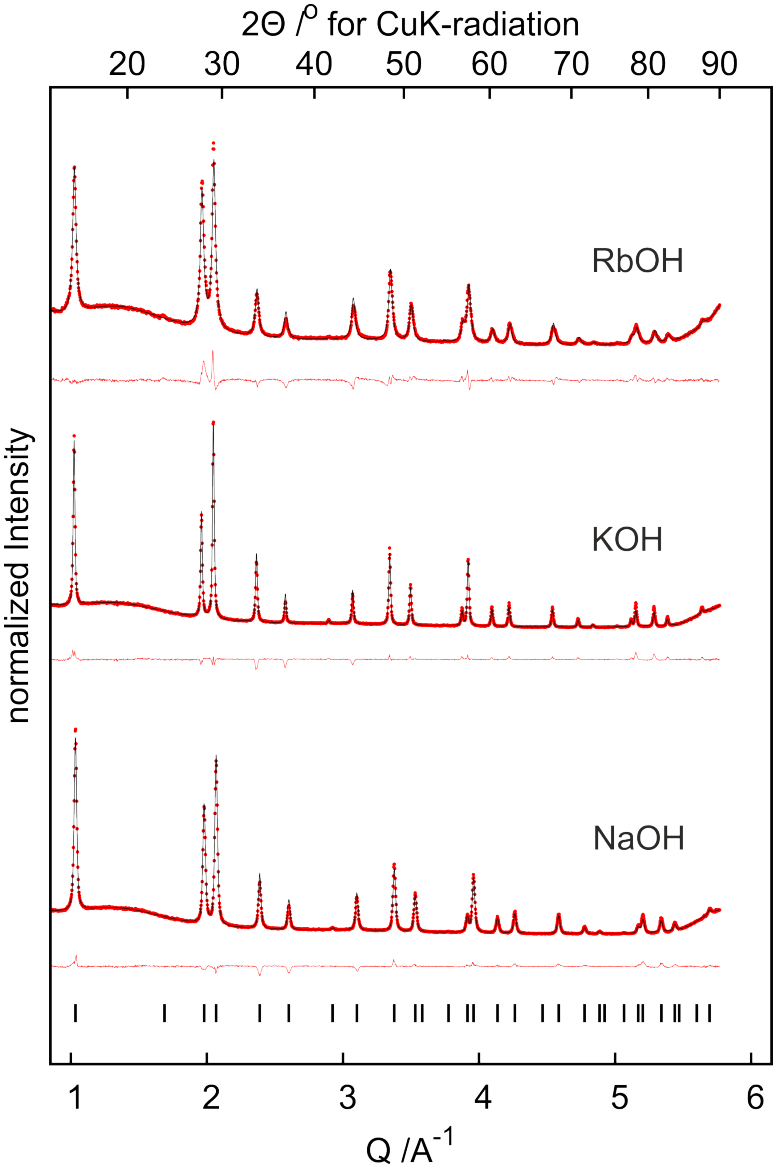

Figure 4.3.: X-ray diffraction patterns and corresponding Rietveld fits (red dots: observed intensity, black line: fit, red line: difference curve) of the products prepared with 0.1 m RbOH, KOH or NaOH respectively. Bottom tick marks for the pyrochlore structure.

as they exhibit the same broad reflexes that cannot be assigned to a phase due to the weak crystallinity. For further characterization EDX was performed on the rods to confirm the elemental composition illustrated in Figure 4.4. Only tantalum and oxygen

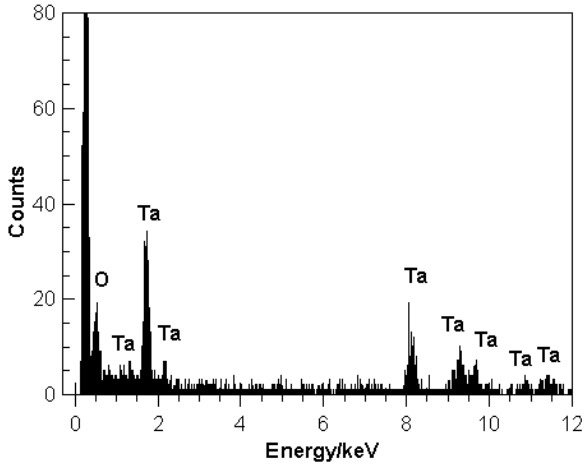

Figure 4.4.: EDX of the tanalum oxide rods obtained with 5 mM RbOH.

are contained in the samples without any trace amounts of rubidium. This is due to the low alkali metal concentration in the solutions. Thus this confirms that the rods are indeed tantalum oxide.

TEM images show the morphology of the products with different bases, KOH and RbOH, synthesized at pH=7 and 12 (see Figure 4.5). In each case (e.g. for NaOH in Figure 4.1) non-agglomerated nanorods were obtained. The product exclusively contained anisotropic particles. The mean width of the nanorods is 8 nm for both RbOH and KOH. Hence there is no discernable morphological difference between the rods synthesized with different bases. Figure 4.5c and d show TEM images of nanoparticles obtained from solutions containing 100 mM of KOH and RbOH, respectively. With KOH, cubic nanoparticles with almost round edges were obtained having an average length of 34±7 nm. No differences in morphology were found between products with either KOH or NaOH. However, when RbOH was used to adjust the pH cube-shaped nanoparticles with a slightly broader size distribution of 26±13 nm were obtained (compared to nanoparticles obtained using KOH)(see Figure A.4).

The HRTEM images in Figure4.6 reveal details of the crystal structure of the cubes as well as the rods. The HRTEM image of the nanoparticles from 100 mM RbOH solution (Figure 4.6a) indicates that the particles are mesocrystalline, i.e. they consist

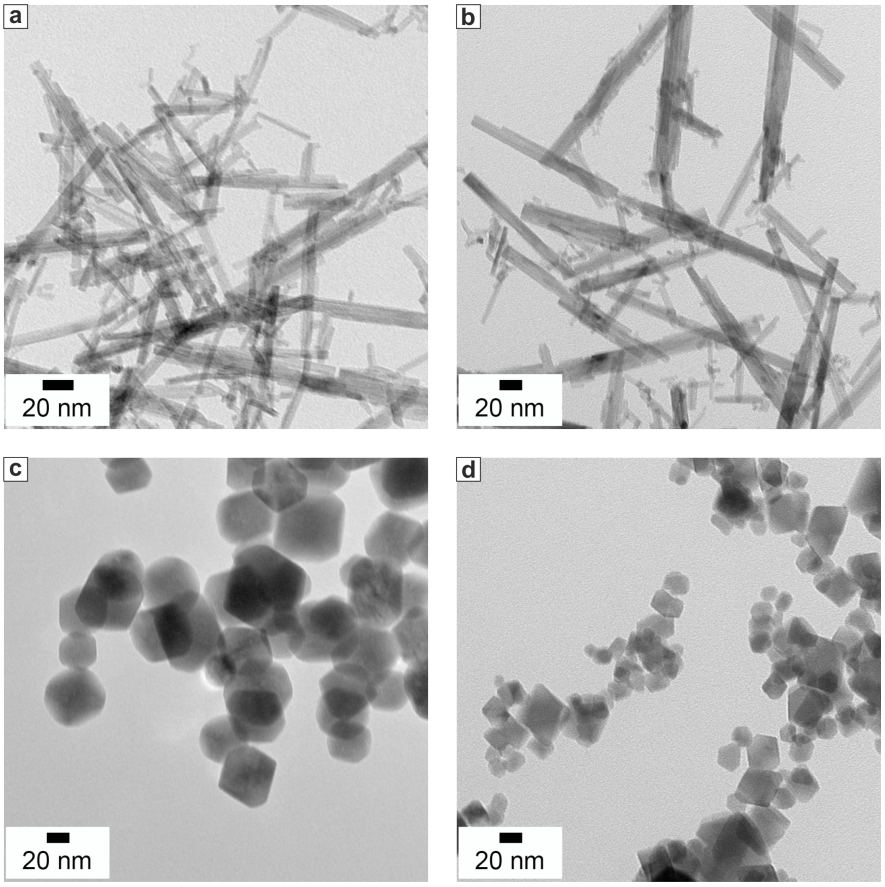

Figure 4.5.: TEM micrographs of the nanoparticles yielded with different bases at different pH values. a) pH=7 with KOH and b) RbOH as applied base and c) KOH at pH=12 and d) RbOH at the same pH.

of individual small crystallites. The crystallinity of the nanocubes was confirmed by fast Fourier transform (FFT, Figure 4.6b). A HRTEM image of the nanorods reveals stacking and lateral disorder in the rods as depicted in Figure 4.6c. The fast Fourier transform image (Figure 4.6d) corroborates the model of crystallinity even though the reflections are blurred due to disorder in the observed area.

4.4.3. Ion exchange in the tantalates and heat treatment

Ion exchange in the pyrochlore structures is a known phenomenon where the alkali metal ions on the intra-channel positions of the pyrochlore framework can be replaced by other cations like H_3O^+ [204] or Pb^{2+}.[176] This offers the opportunity to change the composition of the nanoparticles from tantalates to tantalic acid without a change

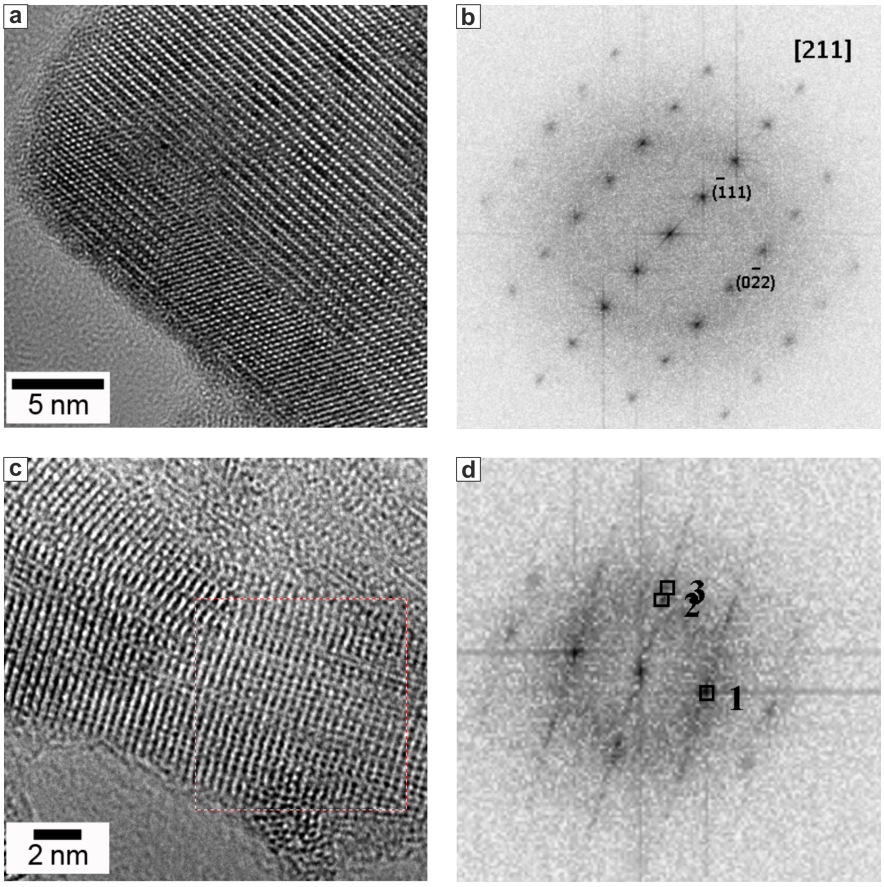

Figure 4.6.: a) HRTEM image of the cubes with 0.1 M RbOH and corresponding FFT. c) HRTEM micrograph of the Ta_2O_5 nanorods synthesized with 5 mM RbOH and associated d) FFT of the nanorods.

in morphology. Hence the tantalates were treated with dilute HCl (2 M) to replace M^+ (M=Na, K, Rb) in the structure by H_3O^+. For ion exchange experiments the tantalate nanoperticles synthesized with 100 mM KOH, NaOH and RbOH, respectively, are used. TEM measurements of the HCl-treated tantalate nanoparticles (Figure 4.7a) reveal no apparent change in morphology or size distribution during the treatment with HCl. The nanoparticles maintain their cubic shape and remain faceted. The particles, however, appear to have rounded edges after the treatment. The extent of the ion exchange was monitored by XRF. The K:Ta ratio of the nanoparticles, synthesized with 100 mM KOH, dropped to K:Ta 1:30 after acid treatment. The corresponding X-ray diffraction patterns are composed in Figure 4.8. The X-ray diffraction pattern of the ion exchanged sample exhibits significant changes of the intensity of some reflections,

i.e. (311), (222), (044) and (622), and a slight shift of all reflection towards higher scattering angles corresponding to a decrease of the lattice parameter from 10.6324(2) Å to 10.6014(2) Å (see Table A.4 in the appendix). According to the results of the Rietveld refinements the composition changes from $K_{0.97}H_{1.03}Ta_2O_6$ to $H_2Ta_2O_6 \times 0.45H_2O$. Thus, the K^+ions are fully replaced by protons and additional water molecules of crystalization. The same effect was found for $NaTaO_3$ and $RbTaO_3$, where virtually no traces of alkali metal were found (see Table A.3 in the appendix). This data corroborates an ion exchange in the tantalate nanoparticles. Ion exchange opens a route to cube-shaped

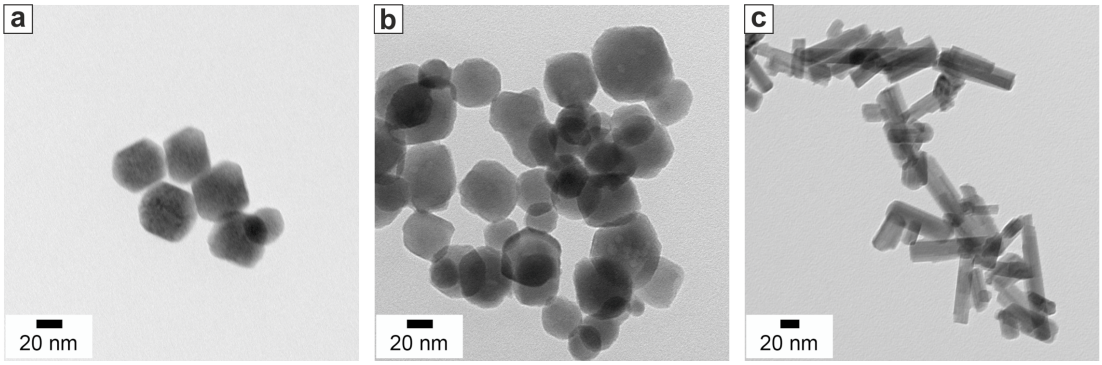

Figure 4.7.: TEM images of a) the tantalate nanoparticles after acid treatment, b) heat treated cubes after 12 h at 923 K, and c) annealed nanorods after 12 h at 1023 K.

tantalum oxide nanoparticles via thermal dehydration of $HTaO_3$. TEM images of a sample heated to 923 K for 12 h confirm that the nanoparticles retain their morphology (Figure 4.7b) after heat treatment. The tantalum oxide nanorods were annealed for 12 h at 1023 K to improve their crystallinity. TEM data (see Figure 4.7c) reveals the calcinated product to retain a rod-like morphology although the aspect ratio has decreased in comparison to the as-synthesized samples. TEM studies show a smaller aspect ratio as the length of the rods decreases while the width increases.

Quantitative phase analyses (see Figure 4.8) reveal both heat treated samples to be phase pure orthorhombic Ta_2O_5 (Ta_2O_5-$oP14$). The crystallite sizes of the cubic nanoparticles correspond to an aspect ratio of 1.5, while 2.9 is found for the rods in agreement with the higher anisotropy of the rods compared to the cubes, even at elevated temperatures. The details of the Rietveld refinement as well as the measuring parameters ae summarized in Table A.4 in the appendix. Without prior acid treatment of the cubes, no phase transformation occurs up to 1023 K for all tantalates.

The HRTEM images of the annealed rods and cube-shaped tantalum oxide nanoparticles

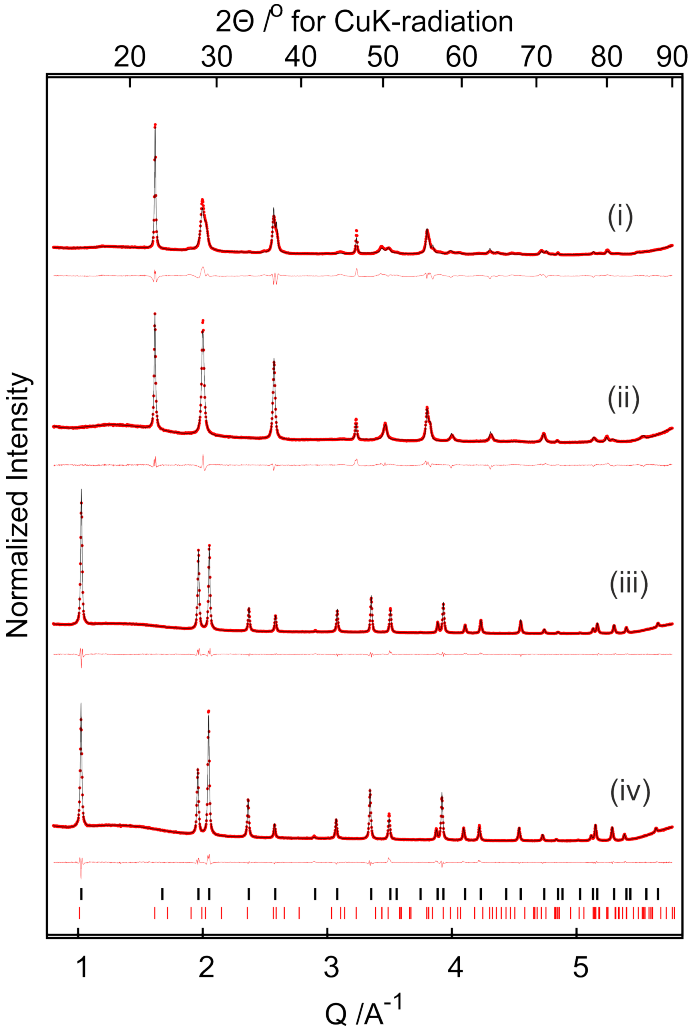

Figure 4.8.: X-ray diffraction patterns and corresponding Rietveld fits (red dots: observed intensity, black line: fit, red line: difference curve) of (i) tantalum oxide rods after annealing at 1123 K for 12 h, (ii) cubes after annealing at 1023 K for 12 h, and (iii) tantalates after and (iv) before acid treatment.

revealed the detailed crystal structure through their corresponding FFT patterns as depicted in Figure 4.9. For the annealed rods the predominant growth direction is along

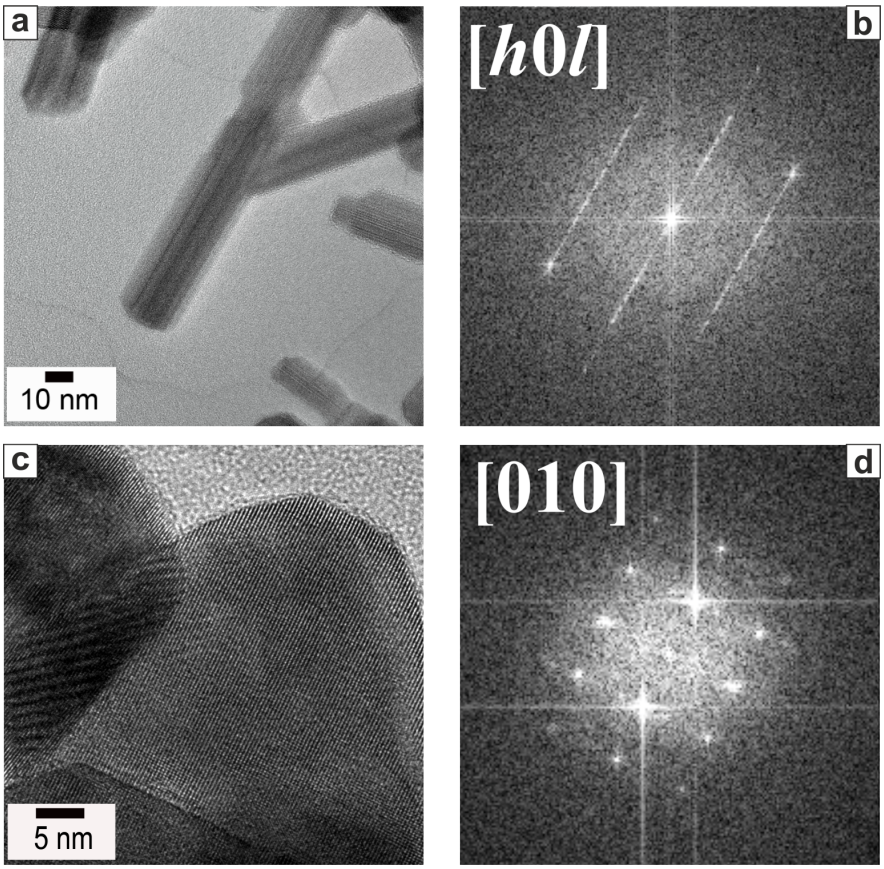

Figure 4.9.: a) HRTEM image of the heat treated rods (12 h, 1123 K) with b) the corresponding FFT pattern. c) HRTEM micrograph of the heat-treated cubes (12 h, 1023 K) synthesized with 0.1 M KOH and the corresponding FFT pattern in d).

the [010] direction. Additionally the annealed rods (Figure 4.9a) show a high degree of disorder orthogonal to the growth direction illustrated by the drawn-out spots in the FFT image in Figure 4.9b. The disorder is less pronounced in the annealed cubes that are shown in Figure 4.9c. However, they are not single crystalline but rather consist of various crystallites which is reflected in the FFT patterns (see Figure 4.9d). The FFT analysis confirms for both samples that the heated cubes as well as the rods consist of orthorhombic Ta_2O_5 in agreement with the PXRD data.

4.4.4. Photocatalytic activity

The photocatalytic activity of the nanoparticles is explored by mixing dispersions with a RhB solution and irradiation with UV light. Figure 4.10a shows the UV-VIS spectra of the solutions after centrifuging the nanoparticles exposed to UV-light for 18 minutes. Figure 4.10b shows a photograph of the corresponding vials. Cube-shaped $KTaO_3$,

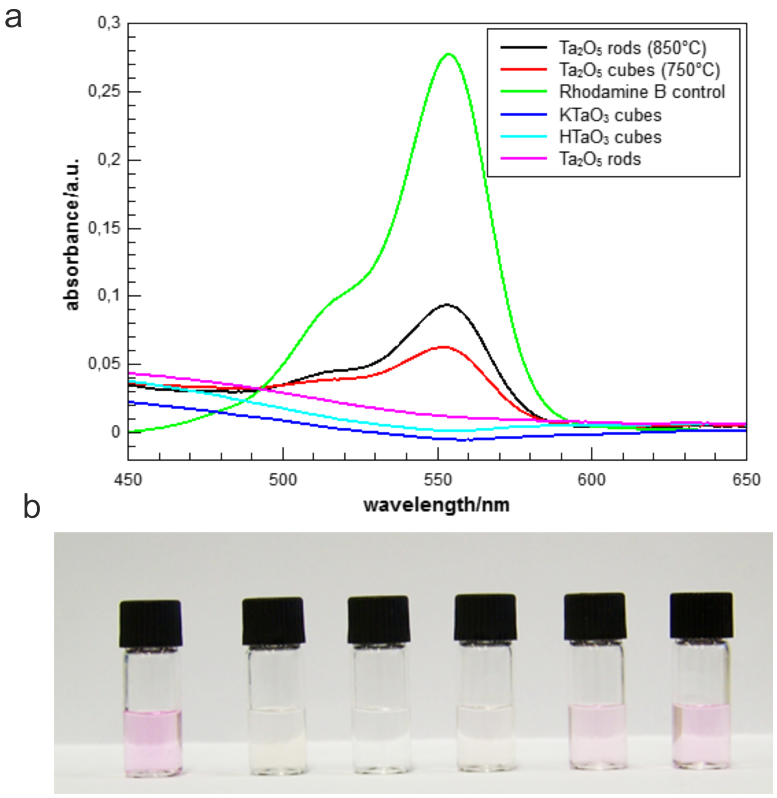

Figure 4.10.: a) UV-VIS spectra of the samples after UV-light irradiation for 18 minutes and centrifugation of the nanoparticles. b) Digital photograph of the corresponding solutions from the left to the right: control RhB solution, $KTaO_3$, $HTaO_3$, Ta_2O_5 (rods), Ta_2O_5 (cube shape)(750°C), and Ta_2O_5 (rods) (850°C)

$HTaO_3$ and as-synthesized Ta_2O_5 nanorods lead to a complete degradation of RhB dye; no absorbance of RhB could be observed. Virtually no RhB absorbance is found after 8 minutes irradiation for the rods, after 4 minutes for cube-shaped $HTaO_3$ and after 12 minutes for cube-shaped $KTaO_3$. The activity difference between cube-shaped $HTaO_3$ and $KTaO_3$ can be attributed to the acidic groups on the surface of $HTaO_3$, which facilitate the degredation of the dye. An absorbance of RhB can be observed

for both heat-treated samples. The absorbance dropped to 22% and 34% compared to the RhB control for the Ta_2O_5 cubes and rods, respectively. As control experiment the samples were stirred with RhB in the dark for 18 min. There was virtually no dye degradation in the dark for all samples as can be seen in Figure A.6 in the appendix. Possible reasons, why the heat treated Ta_2O_5 did not degrade RhB as fast as their as-synthesized counterparts (in spite of their higher crystallinity) might be that this crystalline phase is not as catalytically active as the as-synthesized phases. Additionally, it is likely that the surface area of the samples decreased upon annealing. Additionally, the wetability of the Ta_2O_5 surface might decrease during the heat treatment.

4.5. Conclusions

In summary, we synthesized nanosized Ta_2O_5rods and $MTaO_3$ cubes (M=Na, K, Rb) by a facile hydrothermal route. Furthermore we demonstrated the pH dependence in the synthesis of tantalum oxide and tantalate nanoparticles. Similarly as for titanates [207] the obtained morphologies range from particle agglomerates in acidic reaction media to rods. With varying pH value the obtained morphologies range from particle agglomerates in acidic reaction media over rods at neutral pH to tantalate cubes at neutral pH to tantalate cubes in basic reaction media. Whereas there was no apparent influence of the base cation on the particle morphology, [208] there was a pronounced influence on the particle composition. At high base concentrations cubic tantalate particles with a pyrochlore structure formed. The pyrochlore structure allowed a complete ion exchange through the tunnels in the structure replacing all alkali metal ions with H^+ while retaining the morphology. Thereby cube shaped $HTaO_3$ nanoparticles were obtained. In addition the as-synthesized particles showed promising photocatalytic properties. For this their catalytic activity towards RhB degradation was tested.

5

Synthesis of mesoporous tantalum oxide and loading with palladium nanoparticles

5.1. Abstract

Noble metal nanoparticles supported on mesoporous oxides have garnered the interest of researchers and scientists for catalytic applications. They show promising synergystic properties as they surpass the catalytic properties of their individual compounds. We synthesized mesoporous tantalum oxide (mTa_2O_5) nanoparticles with high surface area (over $165\,m^2/g$) and monomodal pore sizes (3.7 nm) *via* a template-free self-assembly process. The annealing of as synthesized mTa_2O_5 resulted in increased pore diameters (up to 8.1 nm) and crystallinity. The mTa_2O_5 were functionalized with amine groups using 3-aminopropyltriethoxysilane (APTES) to facilitate as subsequent binding of noble metal nanoparticles. Palladium nanoparticles grew onto mTa_2O_5 in a sonochemical reaction to form a nanocomposite ($Pd@mTa_2O_5$) with an intact mesoporous structure.

5.2. Introduction

Noble metal nanoparticles have attracted great interest over the last decades due to their formidable catalytic, electrical and optical properties.[3,45,209] In particular, they catalyze a myriad of different reactions and various substrates.[28,210,211] Since small nanoparticles tend to agglomerate and lose surface area. Noble metal nanoparticles are commonly dispersed on solid oxide supports which improves their thermal stability.[212] Moreover, the supports can also play an active role in catalytic reactions through synergistic interfacial interactions. The supports provide either surrounding acid/base and redox sites or an active metal/metal oxide interface which improves the catalytic

performance of the noble metal nanoparticles.[213–216] Additionally metal nanoparticles might enhance light absorption and charge-carrier separation in semiconducting metal oxide supports. Often mesoporous oxides are used as solid support owing to their high surface area and pores in the same size regime as the metal nanoparticles. Due to their high surface area mesoporous oxides are used as catalysts to catalyze various reactions such as redox reactions,[24] photocatalytic hydrogen evolution[21,174,217,218] and Acetal-/Ketalization.[219] In turn noble metal particles can improve those reactions as well as alter the chemoselectivity.[220]

While there are several methods used for the synthesis of bulk mesoporous transition metal oxides[26,84,85,219,221–224] the preparation of mesoporous transition metal nanoparticles remains a challenge due to their high reactivity compared to silica.[26,93] Especially for mTa_2O_5 nanoparticles there are a few protocols reported so far. The high hydrolysis rate leads to bulk[85,91,218,222,225–227] or large size mTa_2O_5 microparticles[217,228,229] or poorly shaped mTa_2O_5 nanoparticles.[223,230] The most common way to synthesize mesoporous materials are template-assisted routes where the mesoporous structure is predetermined by either a hard (like nanocasting) or soft (e.g. Pluronic F127) template as discussed in chapter 2.4. One of the advantages of syntheses without auxiliary templates is that there are no arduous subsequent steps required for template removal. Additionally, mesostructures may collapse upon template removal.[231] Sometimes the reactivity of mesoporous materials is not only linked to their surface area but to the pore size and crystallinity as well. Therefore, mesoporous materials are subjected to a subsequent heat treatment to induce crystallization which can also alter the pore size.[220,222]

In general, there are two different approaches to load metal nanoparticles onto mesoporous supports: i) co-precipitation and ii) impregnation. For the former, the metal nanoparticles and the support are synthesized simultaneously whereas for the latter the metal nanoparticles are loaded onto the pre-formed supports.[216,232–234] One of the major drawbacks of the co-precipitation is the deviating condensation and growth kinetics as well as the chemistry of the metal oxide and metal precursors. Often this prohibits co-assembly and leads to a phase separation at the macro scale . For the impregnation approach either the pores are impregnated with a liquid precursor and the nanoparticles form in situ or preformed nanoparticles are deposited onto the mesoporous support.[235,236] The main problem is the limited wetting/distribution of the nanoparticles resulting in inhomogeneous or low nanoparticle loading. Here the mesoporous support is functionalized with amine groups first. The amine groups facilitate the impregnation of the palladium precursor as well as a homogeneous nucleation and

growth of nanoparticles.
This chapter describes a simple template-free method which allows to obtain spherical mTa_2O_5 nanoparticles with high surface areas (over 165 m^2/g) and narrow pore size distributions. First the reaction parameters (acid/base, Pluronic amount, temperature) are optimized to get uniform, reproducible mTa_2O_5. In addition, a subsequent heat treatment yields crystalline mTa_2O_5 nanoparticles retaining a mesoporous structure. The average pore size of the nanoparticles can be controlled *via* the heating time as the pore sizes increase with heating time. Furthermore, the mTa_2O_5 nanoparticles are decorated with palladium nanoparticles after a foregoing amine functionalization. The Pd@mTa_2O_5 retain their mesoporous structure and high surface area values as measured using nitrogen sorption experiments (according to Brunauer, Emmett and Teller (BET)).

5.3. Experimental

Materials All starting materials were used without further treatment or purification. Pluronic F-127, tantalum(V)-*n*-butoxide ($Ta(OnBu)_5$), 3-aminopropyltriethoxysilane (APTES) (≥98%), absolute ethanol, toluene (p.a.), and sodium tetrachloropalladate(II) (98%) were purchased from Sigma Aldrich. Toluene (extra dry, 99.85% was obtained from Acros Organics.

Synthesis

Synthesis of mTa_2O_5 Typically $Ta(OnBu)_5$ (0.23 mL, 0.53 mmol) was added dropwise to 5 mL of ethanol. After the solution was stirred for 4 h, it was rapidly poured into a 50 mL Teflon lined autoclave filled with 20 mL of water. The autoclave was kept at 473 K for 8 h. After cooling to room temperature, the obtained colorless product was centrifuged (15 min, 9000 rpm) and the supernatant was discarded. Subsequently, the product was washed with 15 mL of ethanol twice and recovered by centrifugation (15 min, 9000 rpm). The particles were dried *in vacuo* at 313 K for 12 h and stored at ambient temperature.

Calcination of mTa_2O_5 The dried as synthesized mTa_2O_5 were heated to 923 K in a corundum boat with a heating rate of 3 K/min and maintained at this temperature for 1, 3 or 6 h, respectively.

Amine functionalized mTa_2O_5 The reaction was carried out in an argon atmosphere. For amine functionalization, 5 mg of mTa_2O_5 nanoparticles were dispersed in 25 mL of dry toluene and heated to 363 K. Then 50 μL of APTES were added and the reaction was stirred overnight. The product was precipitated by centrifugation (10 min, 9000 rpm), washed with 10 mL of toluene and redispersed in 5 mL of ethanol.

Palladium functionalization of amine-functionalized mTa_2O_5 (Pd@mTa_2O_5) The palladium nanoparticle decoration of mTa_2O_5 followed the method previously reported by Lee et al. with slight modifications.[237] The freshly synthesized amine-functionalized mTa_2O_5 in 5 mL of ethanol were mixed with 11.7 mg of Na_2PdCl_4 in 15 mL of ethanol. Then the dispersion was sonicated at ambient temperature for 1 h. The resulting brown product was collected by centrifugation (15 min, 9000 rpm) and washed with 500 μL of water twice, before it was redispersed in 5 mL of ethanol.

Materials Characterization

TEM, HRTEM, EDX. The nanoparticles were characterized by TEM with a Philips EM420 instrument with an acceleration voltage of 120 kV. Alternatively, a Zeiss LEO 906e was used. For sample preparation a dilute ethanolic or aqueous solution was dripped on a carbon coated 300 mesh copper grid. [1]

XRD X-ray diffraction patterns were recorded with a Bruker AXS D8 Discover diffractometer equipped with a HiStar detector using graphite monochromatized CuKα radiation. Samples were glued on top of glass using a VP/VA copolymer (vinylpyrrolidone/vinylacetate) solution in isopropanol. Additionally, powder X-ray diffraction patterns were recorded with a Siemens D5000 diffractometer equipped with a Braun M50 position sensitive detector in transmission mode using Ge (200) monochromatized CuKa radiation. Samples were prepared between two layers of Scotch Magic. Phase analyses were performed according to the PDF-2 using Bruker AXS EVA 10.0. Rietveld refinements for quantitative phase analysis, determination of the composition and evaluation of crystallite sizes, respectively, were performed according to reported structure models using Topas Academic V4.1.[202] Reflection profiles were generated according to the fundamental parameter approach[203] applying a correction for anisotropic crystallite morphologies. Within this model individual crystallite (CS_h) sizes are computed for each reflection (hkl) according to the quadratic form $CS_h = 1/norm\{h^T \times C_{ij} \times h\}$ in

[1] HRTEM measurements were performed by Ingo Lieberwirth

which h is the reciprocal lattice vector corresponding to (hkl) and $C_{ij} = (a_i)^{\frac{1}{2}} \times (a_j)^{\frac{1}{2}}$ is the symmetric second rank tensor of the square roots of the crystallite

N_2 sorption. Nitrogen sorption experiments were performed with a Quantachrome autosorb 6B instrument. The adsorbate was N_2 at 77 K. The multipoint Brunauer-Emmett-Teller (BET) method was employed to determine the specific surface area. The pore size distribution and volume were calculated with the Barrett-Joyner-Halenda (BJH) method of desorption. Before analysis the samples were dried in a vacuum oven (318 K) overnight. [2]

Fourier-transformed infrared spectroscopy FT-IR spectra were measured on a Bruker Tensor 27 spectrometer. The samples were prepared in a KBr pellet.

Zeta potential Zeta potential (ζ-potential) measurements were conducted with a Malvern Zetasizer Nano-ZS. Nanoparticles were either dissolved in ethanol or water before they were filterd with a Millex-GS syringe filter (pore-size 0.22 μm). The surface potential was determined by 2x15 single measurements at T=298 K. [3]

[2] BET measurements were performed by Martin Klünker
[3] Zeta potential measurements were performed by Jan Hilgert and Heiko Bauer.

5.4. Results and Discussion

The synthesis scheme of the Pd@mTa_2O_5 is depicted Figure 5.1. It illustrates the formation process of mTa_2O_5 nanoparticles and their subsequent amine-functionalization as well as the binding of palladium nanoparticles to the tantalum oxide surface. At

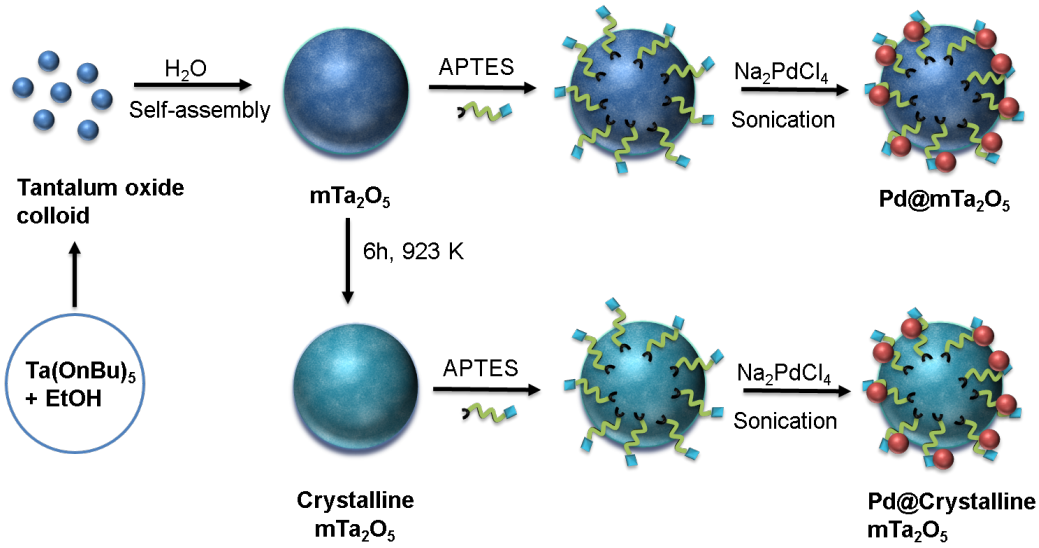

Figure 5.1.: Schematic representation of the synthesis and heat treatment of mTa_2O_5 and their subsequent amine-functionalization and decoration with palladium nanoparticles.

first $Ta(OnBu)_5$ was mixed with ethanol and aged under constant stirring for several hours. This yields a tantalum-containing colloid. Upon addition to water mTa_2O_5 nanoparticles form through a self-assembly process as the small tantalum oxide colloid particles congregate into hierarchical spheres. In a second step mTa_2O_5 nanoparticles are functionalized with APTES *via* a condensation of silane groups onto the hydroxyl groups of the tantalum oxide surface. The presence of amino groups on the surface is essential for the attachment of palladium nanoparticles onto the particles. Subsequently palladium nanoparticles are prepared and attached to mTa_2O_5 in situ using an ultrasonic synthesis.[237] Analogously, crystalline mTa_2O_5 nanoparticles with palladium nanoparticles are synthesized except for an additional heating step (6 h, 923 K) prior to the amine functionalization.

5.4.1. Synthesis of mesoporous tantalum oxide

The following section deals with the relevant reaction parameters for the synthesis of mTa_2O_5 and their influence on the morphology of the nanoparticles.

Influence of bases and acids Commonly, most of the aqueous nanoparticle syntheses are either base or acid catalysed.[74,75,90,93,238] For this reason the Tantalum containing colloid is transferred into different acids e.g. acetic acid, HCl and bases like NH_3, NaOH for hydrolysis with the aim to obtain mesoporous tantalum oxide nanoparticles. The TEM images of those products are compiled in Figure 5.2. Figure 5.2a shows

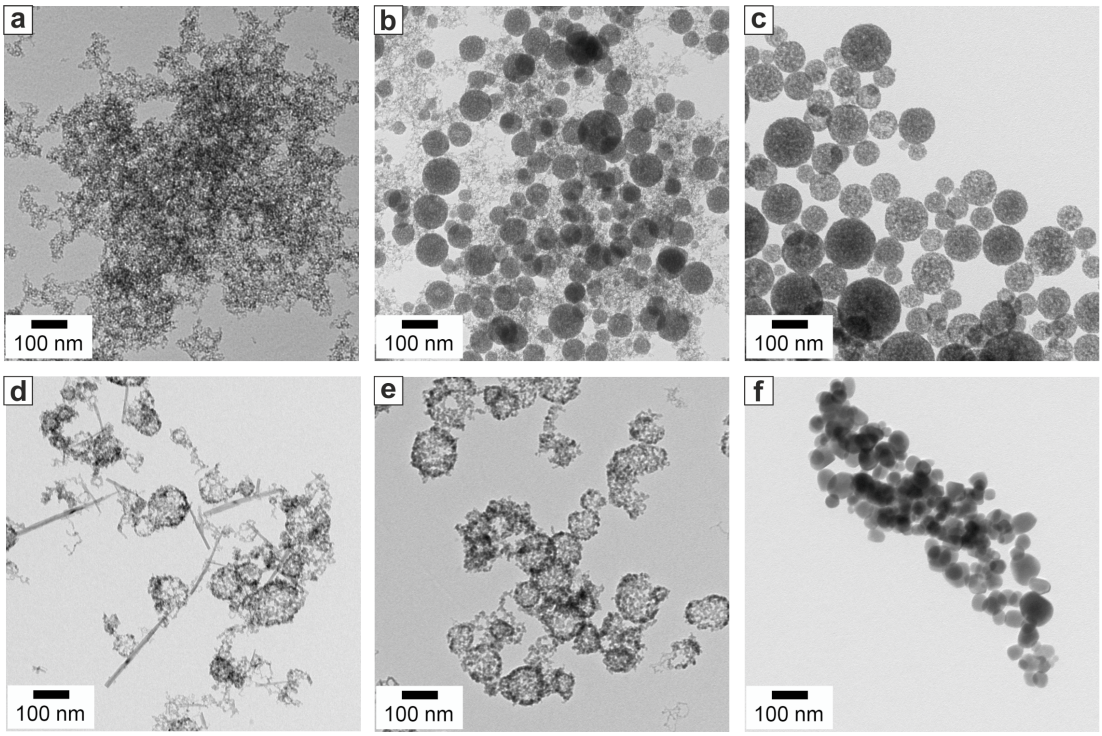

Figure 5.2.: TEM images of the synthesis with 0.5 mL a) HCl b) acetic acid c) only with water d) 0.5 mL and e) 19 mL NH_3 and f) 0.5 g NaOH.

the products synthesized with 0.5 mL of HCl. The TEM images reveal large particle assemblies that consist of small particles. These assemblies, however, lack a distinct shape. In contrast Figure 5.2b depicts the yielded product with 0.5 mL acetic acid. On the one hand there are also small particles that agglomerate randomly like with HCl. On the other hand spherical nanoparticles are present that are between 30 and 180 nm in diameter. Those particles are composed of a myriad of small particles which cause the

grainy texture in the TEM images. When more acetic acid is used the amount of spheres decreased while the agglomerates increased. As opposed Figure 5.2d and e illustrate the reaction products with 0.5 and 19 mL NH_3 respectively. For both the samples consist of small nanoparticles that construct hollow particles occasionally. In case of 0.5 mL of NH_3 nanorods can be observed additionally. Those rods have the same phase as the rods described in chapter 4.4.1. Other NH_3 (between 1 and 5 mL) concentrations were investigated as well but they yield the same results as the examples described here. Figure 5.2e illustrates the reaction product with 0.5 g NaOH. The sample comprises cuboid-shaped particles with rounded edges in the size regime between 20 and 100 nm. The particles resemble the $NaTaO_3$ nanoparticles as described in chapter 4.4.1 and have the same crystalline phase which is a pyrochlore structure. Figure 5.2 c depicts the nanoparticles synthesized without the aid of either acid or base. The whole sample is made up of spherical particles formed of a multitude of smaller particles. There are no other agglomerates present.
The acids and NH_3 primarily influence the small nanoparticles assembly into irregular shapes. To conclude the best mesoporous nanoparticles are obtained with water because the small particles assemble into regular spheres then. Henceforth only synthesis with water will be considered in the following paragraphs.

Variation of the Pluronic F127 amount As most synthesis of mesoporous materials are template assisted co-block polymer Pluronic F127 is chosen as a template agent. The Pluronic F127 amount is varied to gauge its influence as depicted in Figure 5.3. When

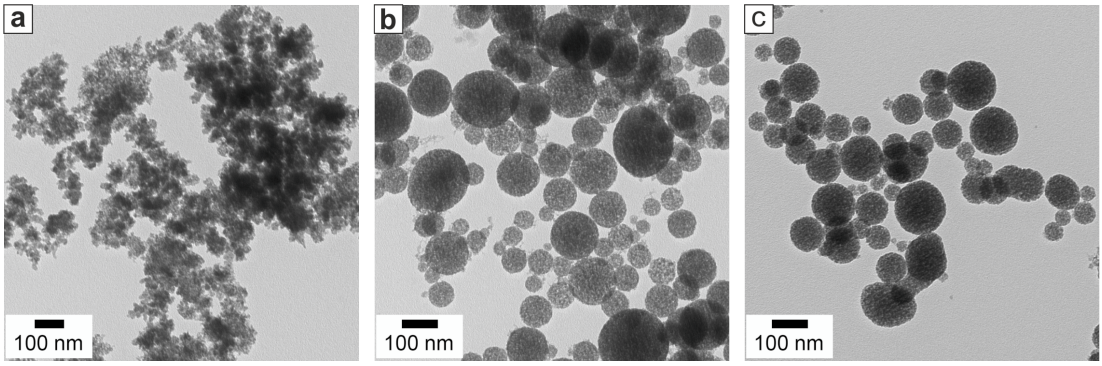

Figure 5.3.: TEM images of the mTa_2O_5 nanoparticles in dependence on the Pluronic amount. a) 600 mg b) 100 mg and c) 0 mg Pluronic F127.

600 mg of Pluronic F127 is used the product contains small randomly agglomerated particles. Thus a high Pluronic F127 concentration hinders the assembly of the tantalum

oxide nanoparticles into well defined mTa_2O_5 nanospheres. An example for 300 mg of Pluronic can be found in figure 5.2 c where the sample consists of spherical mTa_2O_5 nanoparticles. Figure 5.3 b shows that spherical mTa_2O_5 nanoparticles form with 100 mg of Pluronic F127. There is virtually no difference between 100 and 300 mg Pluronic when it comes to morphology (150 mg is tested as well and yields the same morphology). At least the reaction is carried out without Pluronic F127 and is illustrated in Figure 5.3 c. Surprisingly there are spherical mTa_2O_5 nanoparticles with a grainy texture as well. Additionally some dumbbell-shaped particles appear that are also mesoporous. Thus the formation of mesoporous particles is not dependent on Pluronic F127. As a consequence the underlying mechanism cannot be a classical template mechanism as no template is required. Alternatively the formation of mTa_2O_5 nanospheres might be according to a self-assembly mechanism.[239] A common feature in the synthesis attempts of mTa_2O_5 is that most samples consist of small particles. Merely the arrangement of those small particles differs. Hence those particles are probably preformed in the tantalum oxide colloid.[240] In a second step the Ta_2O_5 nanoparticles are poured into an aqueous solution. There they assemble into spherical particles depending on the solvent composition. The driving force behind the self-assembly process is the minimization of surface energy which is the lowest for spheres. This explains why high Pluronic F127 concentrations disturb the assembly. Since they stabilize the Ta_2O_5 nanoparticles the gain in surface free energy is reduced. The same is true for high acid concentrations. At low pH the tantalum oxide surface is protonated and the charge prevents the assembly of single particles due to electrostatic repulsion.

Other parameters As the tantalum oxide colloid precipitates immediately when poured into water, the solid was investigated using TEM [4]. Figure 5.4 b shows the precipitate as spherical particles that resemble the particles after hydrothermal treatment using autoclaves. Thus the mTa_2O_5 form promptly which is unexpected. Usually the assembly of mesoporous materials is governed by slow processes like EISA (see chapter 2.4.1) as the high reactivity needs to be moderated for ordered mesoporous materials.[26] In a next step the influence of the water temperature was determined. Figure 5.4 a and c show the mTa_2O_5 precipitated from water at 279 K and 318 K respectively. For both, mesoporous spherical particles are obtained. Yet at 318 K some of the particles are either agglomerated or dumbbell-shaped. Thus the assembly of mTa_2O_5 nanoparticles cannot proceed in a regular fashion leading to uncontrolled agglomeration at higher

[4] It is common that the precursors precipitate in water prior to a hydrothermal treatment. Those precipitates are agglomerates mostly.

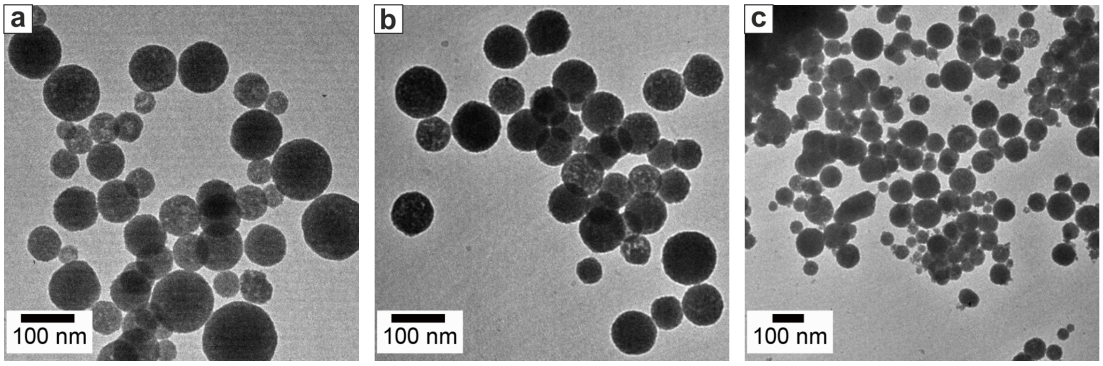

Figure 5.4.: TEM images of the mTa_2O_5 nanoparticlesin dependence of the water temperature. Water temperature in a) 279 K b) 298 K and c) 318 K.

temperatures. This is probably due to higher reaction rate at elevated temperatures. In the following sections the mTa_2O_5 are synthesized at ambient temperatures as the yield is reduced at 279 K. Despite these findings the mTa_2O_5 the mTa_2O_5 are subjected to hydrothermal treatment as the long time stability increased upon the hydrothermal treatment. Since the particles are already formed it does not matter whether the nanoparticles are heated to 473 K or 453 K.

Moreover the influence of the stirring time of the Tantalum containing colloid was monitored. The stirring time was varied between 1 h and 30 h. There is no difference in the mTa_2O_5 nanoparticle morphology. The morphology is independent of the stirring time in this time interval.

To conclude the best mTa_2O_5 particles can be synthesized with water without additional acid or bases at room temperature. An Pluronic F127 amount between 150 and 300 mg leads to the best spherical mTa_2O_5.

5.4.2. Structural characterization

Morphology of the as synthesized an annealed mTa_2O_5 nanoparticles The morphology of the as synthesized and heat treated mTa_2O_5 nanoparticles was characterized using TEM . Representative overview TEM images are shown in Figure 5.5 for the as synthesized (see Figure 5.5 a) and annealed for 1, 3 and 6 h respectively (see Figure 5.5 b-d) mTa_2O_5 nanoparticles. All samples consist of spherical particles in a size regime

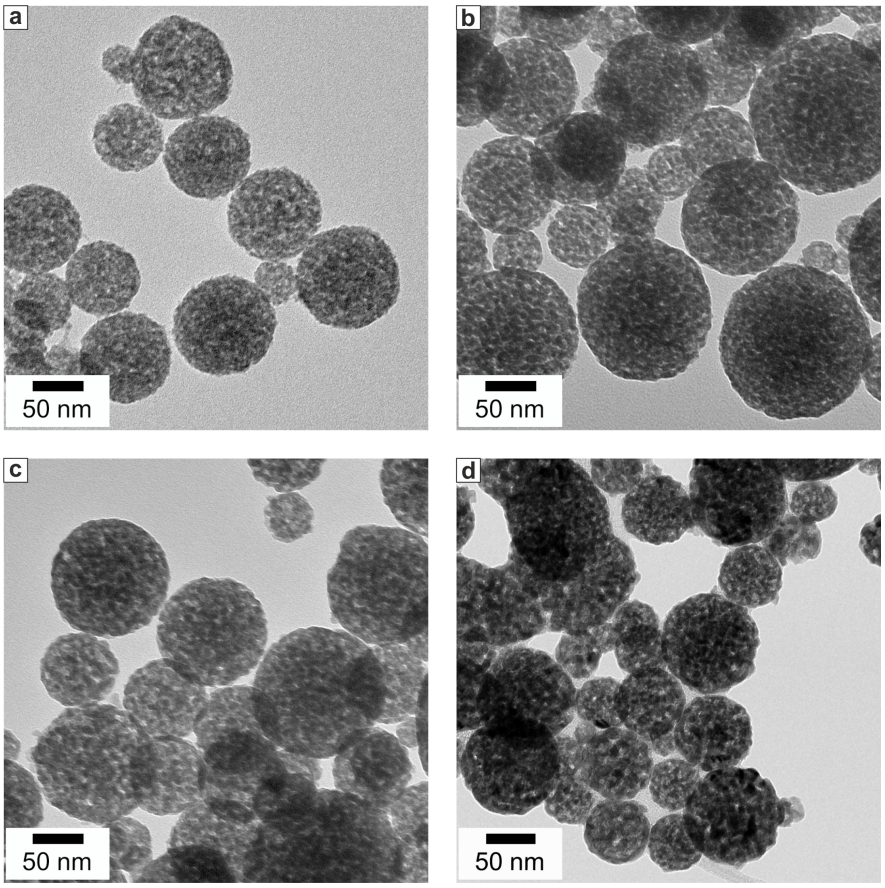

Figure 5.5.: TEM micrographs of the mTa_2O_5 a) as synthesized and after b) 1 h c) 3 h and 6 h at 923 K.

between 20 nm and 180 nm. Hence the mTa_2O_5 retain their shape and overall size distribution upon annealing. Taking a closer look the mTa_2O_5 nanoparticles do not have a uniform TEM contrast but are mottled. This texture originates from a myriad of smaller (about 5 nm) Ta_2O_5 nanoparticles that assemble to form the mTa_2O_5. The driving force behind the self-assembly into mesostructured spheres is the reduction in free surface energy as the spheres have the lowest surface to volume ratio.

As the annealing time increases, the texture of the mTa_2O_5 nanoparticles coarsens. The diameter of the cavities (areas of lower color contrast in the TEM images) enlarge in the particles. At the same time the small Ta_2O_5 building blocks grow especially in the sample after 6 h at 923 K. Furthermore after annealing for 6 h some of the whole mTa_2O_5 start to sinter together.
When even higher temperatures (973 K or 1073 K) are employed the mTa_2O_5 nanoparticles sinter together to a higher degree. At 1173 K the mTa_2O_5 nanoparticles lose the texture and shape of the as synthesized particles as can be seen in Figure 5.6. The single mTa_2O_5 building blocks are completely sintered together under these conditions. Therefore all pores are collapsed which is a common occurrence upon heat treatment. [222] The overall size of the particles, however, is still in the nanometer regime.

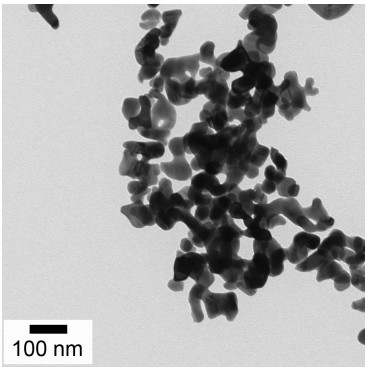

Figure 5.6.: TEM micrograph of the mTa_2O_5 heat treated at 1123 K for 6 h.

The HRTEM images in Figure 5.7 reveal the detailed structure of the as synthesized as well as the annealed (6 h, 923 K) mTa_2O_5 nanoparticles. In Figure 5.7 the amorphous structure of the as synthesized can be observed as there is a random arrangement of atoms. In addition there are areas of a low color contrast in the TEM images that correspond to areas with (more) cavities. The SAED pattern of the as synthesized mTa_2O_5 in Figure 5.7 b has neither distinct reflexes nor Debye Scherrer rings. These findings promote the lack of crystallinity in the as synthesized samples which is in good agreement with the X-ray diffractogram. In contrast the SAED of the heat treated mTa_2O_5 (see Figure 5.7 d) exhibit distinct Debye Scherrer rings confirming the crystallinity of the sample. Furthermore this signifies the polycrystallinity in the observed area. Figure 5.7 c presents a HRTEM image of the heat treated nanoparticles. As opposed to the as synthesized mTa_2O_5 these particles exhibit lattice fringes typical for crystalline substances. Additionally the nanoparticles also feature cavities. Those cavities, however, are distinctly larger than those for the as synthesized mTa_2O_5. Yet it

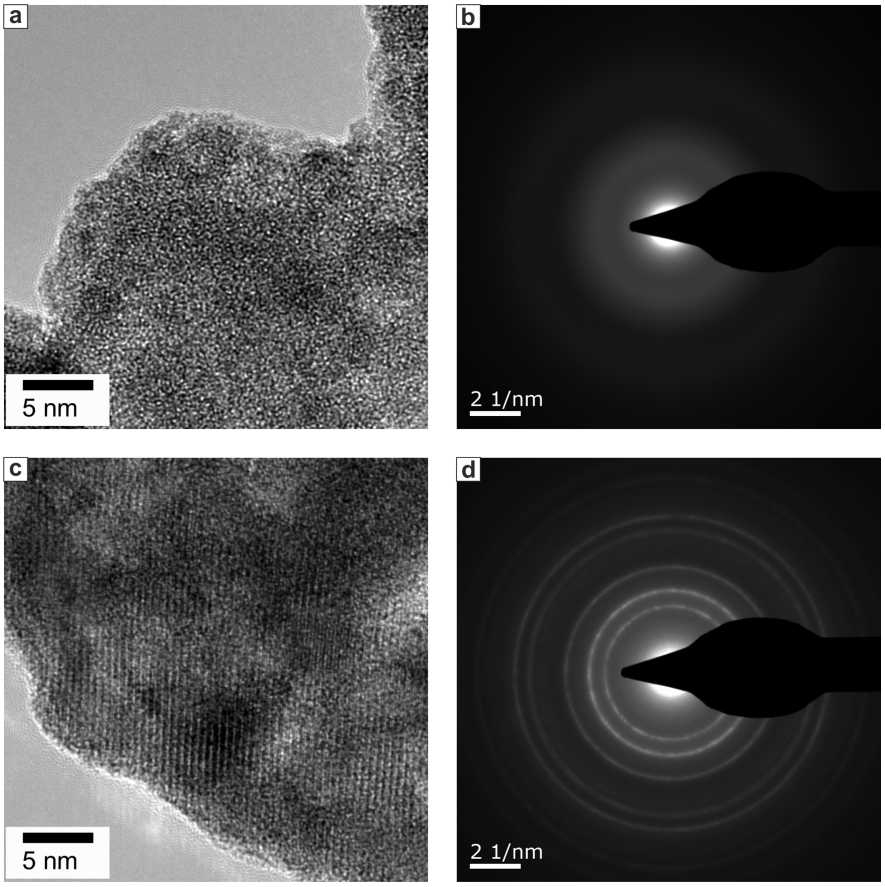

Figure 5.7.: a) HRTEM micrograph of the as synthesized mTa_2O_5 and b) an associated SAED pattern. c) HRTEM image of annealed mTa_2O_5 (6 h at 923 K) and d) associated SAED pattern.

is not possible to determine the exact cavity size based on the HRTEM images as the cavities are superimposed.

Crystallinity In order to determine the crystallinity of the as synthesized and heat treated samples, powder XRD diffractograms were recorded that are illustrated in Figure 5.8. The as synthesized mTa_2O_5 exhibit no crystalline phase and thus can be desribed as amorphous. This turns out as expected since most as synthesized Tantalum oxides nanoparticles are amorphous prior to a heat treatment.[185] Additionally there is no crystalline phase observable for the samples heated for 1 h and 3 h at 923 K, respectively. In contrast when the mTa_2O_5 were annealed for 6 h the sample is crystalline. The reflexes can be assigned to phase pure orthorhombic Ta_2O_5 (Ta_2O_5-$oP14$, see tic marks in Figure 5.8). According to Rietveld refinement the average crystallite size is 23(1) nm.

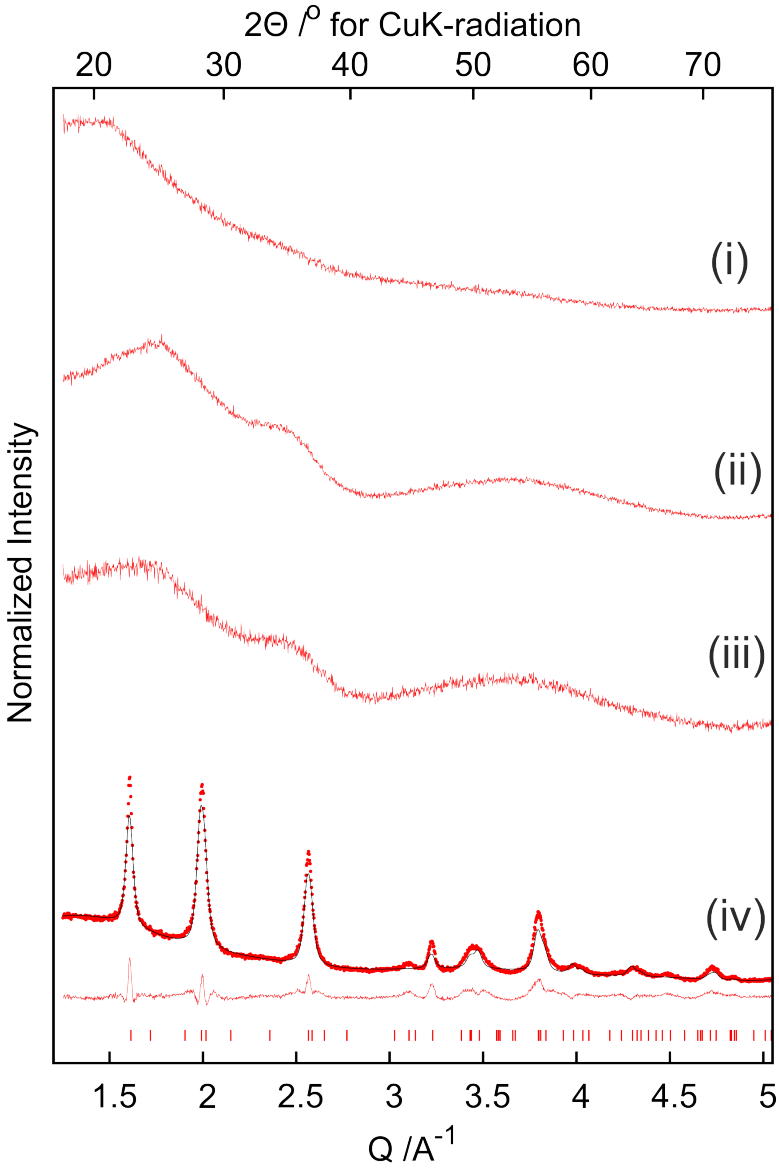

Figure 5.8.: X-ray diffraction patterns and corresponding Rietveld fits (red dorts: observed intensity, black line: fit, red line difference curve) of the (i) as synthesized mTa_2O_5 and heat treated mTa_2O_5 for (ii)1 h, (iii) 3 h and (iv) 6 h at 923 K. Bottom: tic marks of Ta_2O_5.

This is bigger than a single nanoparticle building block of the $mTa2O_5$ as observed in the TEM images in Figure 5.5. Therefore it is likely that two or more nanoparticle building blocks sinter together to form a crystallite. The details of the Rietveld refinement are summarized in table A.5 in the appendix.

Mesoporous structure. The surface area and mesoporosity of the as synthesized mTa_2O_5 as well as the heat treated samples (1, 3 or 6 h at 923 K) was determined with N_2 sorption isotherms as shown in Figure 5.9 a. The slope of the isotherm between 0.05 and 0.3 p/p_0 (linear region) is used to calculate the surface area (S_{BET}) of the particles with the with N_2 sorption utilizing the BET method. Those surface areas for all samples are listed in table 5.1. For the as synthesized mTa_2O_5 nanoparticles the surface area is 166 m^2/g. This value is higher than those reported for mTa_2O_5 in the literature[222,225,228,230] that are between 95, 132 and 153 m^2/g whereas the latter is reported for bulk mTa_2O_5. When the samples are heat treated at 923 K the surface area decreases over time. After 1 h the surface area is 110 m^2/g, 100 m^2/g after 3 h and goes down to 65 m^2/g in 6 h time. Upon heating the particles start to coalescence. This leads to a loss in surface area when two seperate particle join surfaces to form a single particle which is in good accordance to the TEM data discussed earlier in this chapter. A schematic representation of this process is shown in Figure 5.10.

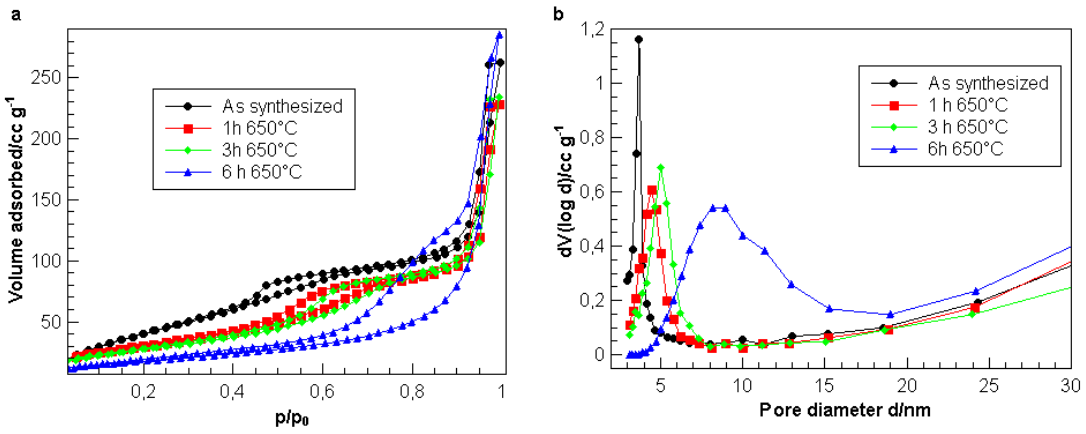

Figure 5.9.: a) N_2 soprtion isotherms and b) BJH desorption pore-size distributions of the mTa_2O_5 as synthesized and heat treated at 923 K for 1, 3 and 6 h.

The shape of isotherms especially at higher relative pressures is related to the mesoporous structure. Generally mesoporous compounds exhibit a hysteresis loop. Here the hysteresis shape is connected to the pore geometry and size distribution of the pores.

All samples show hysteresis above 0.8 p/p_0. This hysteresis suggests the mTa_2O_5 have a mesoporous stucture which is preserved upon annealing. In case of the as synthesized and shortly (1 and 3 h) heat treated mTa_2O_5 the hysteresis curve shows a type IV isotherm with a narrow hysteresis curve.[241] A narrow hysteresis curve indicates an uniform pore-size distribution. In contrast the nanoparticles that were heat treated for 6 h have a broad hysteresis curve which start to fan out at 0.6 p/p_0. Hence, those particles posses widespread pore sizes.
Furthermore the pore-size distribution can be calculated according to the BJH method. The obtained pore size distributions for all samples are displayed in Figure 5.9 b.

Table 5.1.: Structural parameters of the mTa_2O_5 in dependence on the time of heat treatment at 923 K

Time at 923 K/ h	S_{BET} / m^2g^{-1}	Pore size/ nm	Pore Volume/ cm^3g^{-1}
0	166	3.7	0.384
1	110	4.4	0.349
3	100	5.3	0.363
6	65	8.1	0.446

Generally the mean pore size given by the maximum in the pore size distribution curves increases with heat treatment. The pristine mTa_2O_5 nanoparticles have a mean pore size of 3.7 nm before it expands to 4.4 nm and 5.3 nm after 1 h and 3 h heating respectively. Finally after 6 h the mean pore size reaches 8.1 nm. Additionally the pore-size distributions get broader with heating time. The longer the nanoparticles are annealed the more irregular the pore sizes become especially after 6 h at 923 K.

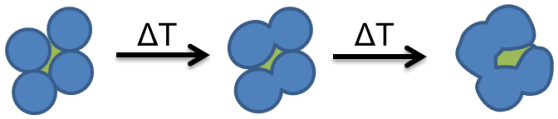

Figure 5.10.: Schematic illustration of the decrease in surface area (darker blue) and increase in pore size (green) upon heat treatment of the mTa_2O_5 nanoparticles.

Overall those observations are in good agreement with the hierarchical nature of the mTa_2O_5 nanoparticles that consist of small Ta_2O_5 nanoparticles as building blocks. Owing to their structure mesopores are formed by connected interparticle voids. When the mTa_2O_5 nanoparticles are heated the separate particles start to sinter together.

Hence, some of the pores vanish while others grow in size like it is illustrated in Figure 5.10. Taking the X-ray data into account the rearrangement of the nanoparticles starts prior to crystallization. As the pore sizes already increase when the particles are still amorphous (after 1 and 3 h at 923 K). By and by the structural rearrangement gets more pronounced and the mTa_2O_5 have enough energy to crystallize. Finally the relatively large crystallite size of 23(1) nm supports the theory that single building blocks coalescence.
Both the decrease in surface area as well as pore expansion is typical of mesoporous materials with a nanoparticle aggregate nature.[225,242,243] In contrast the pores of mesoporous materials synthesized via a template route shrink upon heat treatment due to further condensation of the pore walls.[111,222,244] Those findings indicate mTa_2O_5 nanoparticles do not form via a template method although Pluronic F127, a classical templating agent, is also used in some of the synthesis. To summarize, all structural parameters of the as synthesized and heat treated mTa_2O_5 are composed in table 5.1.

5.4.3. Functionalization with palladium Nanoparticles

The amine functionalization is a crucial step in order to decorate the mTa_2O_5 with palladium nanoparticles. As the as synthesized mTa_2O_5 nanoparticles are amorphous no epitaxial growth can occur on the surface. Therefore the attachment of the Pd nanoparticles is mediated via amino groups[237] due to matching Pearson hardness.[245] This strategy is commonly used to attach nanoparticles *via* different functional groups like thiols onto amorphous particles and surfaces.[237,246–248] Without amino groups there is no attachment of Pd on the mTa_2O_5 surface. Amino groups are introduced to the mTa_2O_5 surface in the form of 3-aminopropyltriethoxysilane (APTES). APTES has a silane group which can bond to the nanoparticles *via* hydroxyl groups on the surface in a condensation reaction. A simplified scheme of the silanisation of the mTa_2O_5 surface is illustrated in Figure 5.11.

The IR spectra attest the functionalization of the as synthesized, amine functionalized and palladium decorated mTa_2O_5 nanoparticles displayed in Figure 5.12. As pristine mTa_2O_5 are not functionalized, there are no bands that can be assigned to organic molecules. The broad band at 3420 cm^{-1} can be assigned to the Ta-O-H stretching band whereas the band at 664 cm^{-1} belongs to the Ta-O-Ta stretching band.[249] At 1624 cm^{-1} the O-H bending band of surface -OH groups and absorbed water, respectively, can be found.[250] After amine functionalization the particles the Ta-O-H stretching band is

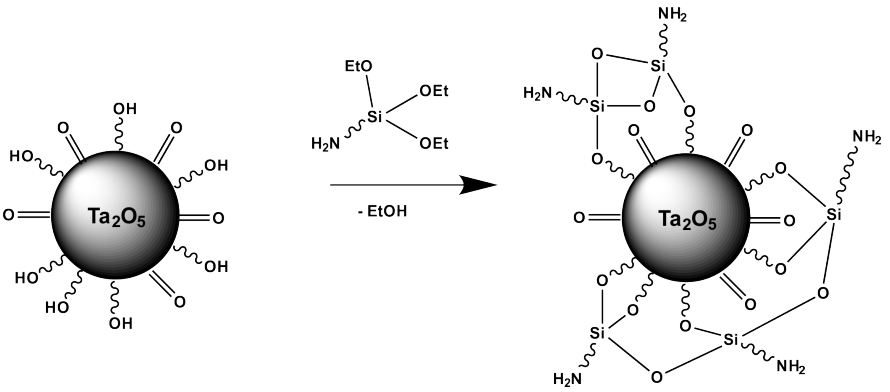

Figure 5.11.: Simplified scheme of the silanisation reaction of APTES on the mTa_2O_5 nanoparticle surface.

far less pronounced as some of the OH groups react with silanes. Additionally a N-H bending vibration appears at 1650 cm^{-1}. Further there are two weak C-H stretching bands of C-H_2 groups at at 2964 and 2927 cm^{-1} that can be attributed to the CH_2 group in the APTES. These findings indicate an amine functionalization of the once pristine mTa_2O_5 nanoparticles. When palladium is attached to nanoparticles there is no clear change in the IR spectrum that can be clearly assigned to palladium. Therefore other characterization methods have to be applied to confirm their presence.
Furthermore the ζ-potential of the nanoparticles was measured to draw inferences from the zeta potential about the surface functionalization. For pristine mTa_2O_5 the ζ potential is -7.7±5.06 mV. In contrast the ζ-potential is 19.5±6.0 mV for the NH_2 functionalized Pd@mTa_2O_5 nanoparticles. Thus there is a marked increase in ζ-potential which can be attributed to the amine functionalization. Typically basic amine groups are positively charged (at acidic or neutral pH).[251,252] Therefore the ζ-potential is a further clue for the amine functionalization.

Morphology The attachment of palladium nanoparticles to both, the as synthesized and annealed mTa_2O_5 nanoparticles, is monitored by TEM (see Figure 5.13). In Figure 5.13 a and b the as synthesized Pd@mTa_2O_5 are displayed. The Pd@mTa_2O_5 maintain the spherical morphology of the pristine mTa_2O_5 (see Figure 5.5 a). Additionally there are nanoparticles attached to the mTa_2O_5 that have the shape of Wulff polyhedrons[18,253] with a diameter of approximately 11 nm. Those are the palladium nanoparticles that are uniformly spread over the mTa_2O_5 nanoparticles.
Figure 5.13 c and d displays the annealed (6 h, 923 K) Pd@mTa_2O_5. The spherical

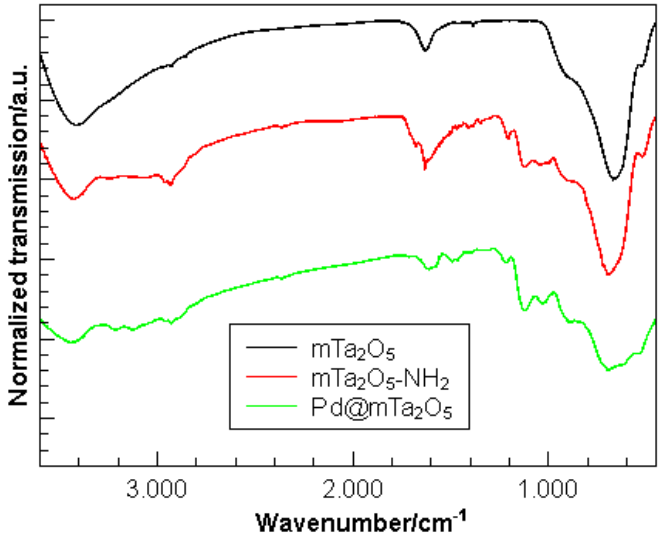

Figure 5.12.: IR spectra of the as synthesized mTa_2O_5 (black), the amine functionalized mTa_2O_5 (red) and the $Pd@mTa_2O_5$ (green) nanoparticles.

shape of the heat treated mTa_2O_5 (shown in Figure 5.5 d) is retained. Those particles are covered in Wulff polyhedron shaped palladium nanoparticles with a diameter around 9 nm. The palladium coverage of the mTa_2O_5 of the heat treated samples is not as dense as pristine mTa_2O_5. This might be due to the lower reactivity of the heat treated tantalum oxide surface. Thus the reactivity towards APTES is decreased and there are less amine groups for palladium to attach to.

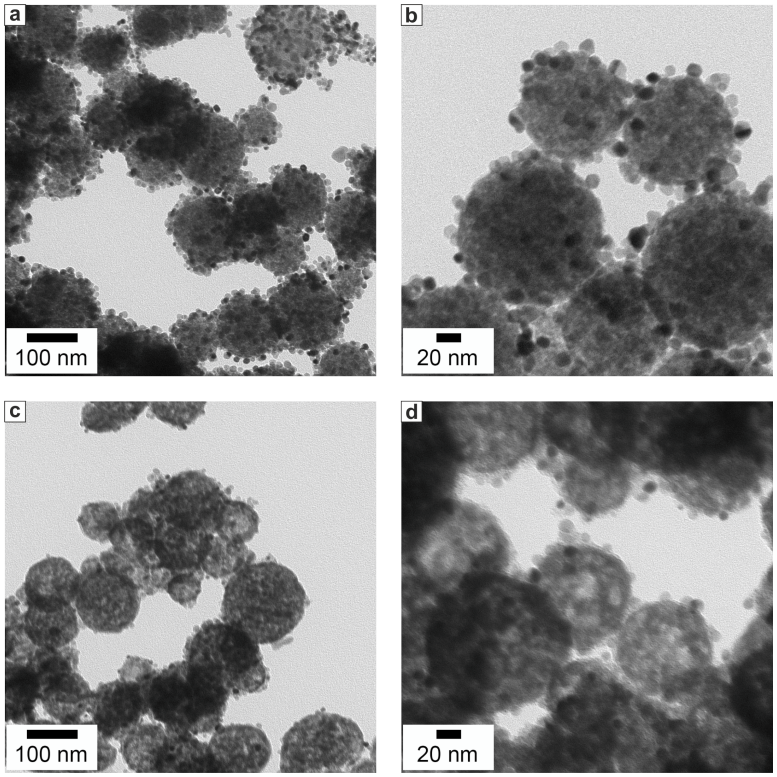

Figure 5.13.: TEM micrographs of the a) and b) the as synthesized Pd@mTa_2O_5 nanoparticles and the c) and d) heat treated (6 h, 923 K) Pd@mTa_2O_5

Crystallinity For further confirmation of the Pd functionalization X-ray diffractograms were recorded illustrated in Figure 5.14. The X-ray diffraction patterns of Pd@mTa_2O_5 with as synthesized mTa_2O_5 nanoparticles exhibit a strong amorphous background that can be attributed to pristine mTa_2O_5 as it is amorphous (see Figure 5.8). Additionally there is one discernable reflex that can be assigned to Pd which corroborates the presence of Pd in the sample. However, due to the amorphous baseline and the weak reflex it is not possible to determine neither the percentage of palladium nor the crystalline size via Rietveld refinement. For the Pd@mTa_2O_5 with annealed mTa_2O_5 (6 h at 923 K) two crystalline phases are present. The main phase can be assigned to orthorhombic Ta_2O_5 (Ta_2O_5-$oP14$) with a crystallite size of 20 nm. This is in good agreement with the PXRD data of the pure mTa_2O_5 that were used as starting material for the palladium functionalization. The second crystalline phase belongs to palladium which makes up 10% of the crystalline substances in the sample. According to Rietveld refinement the size of the palladium crystallites is 12 nm. This corroborates the nanoparticle size obtained from the TEM images.

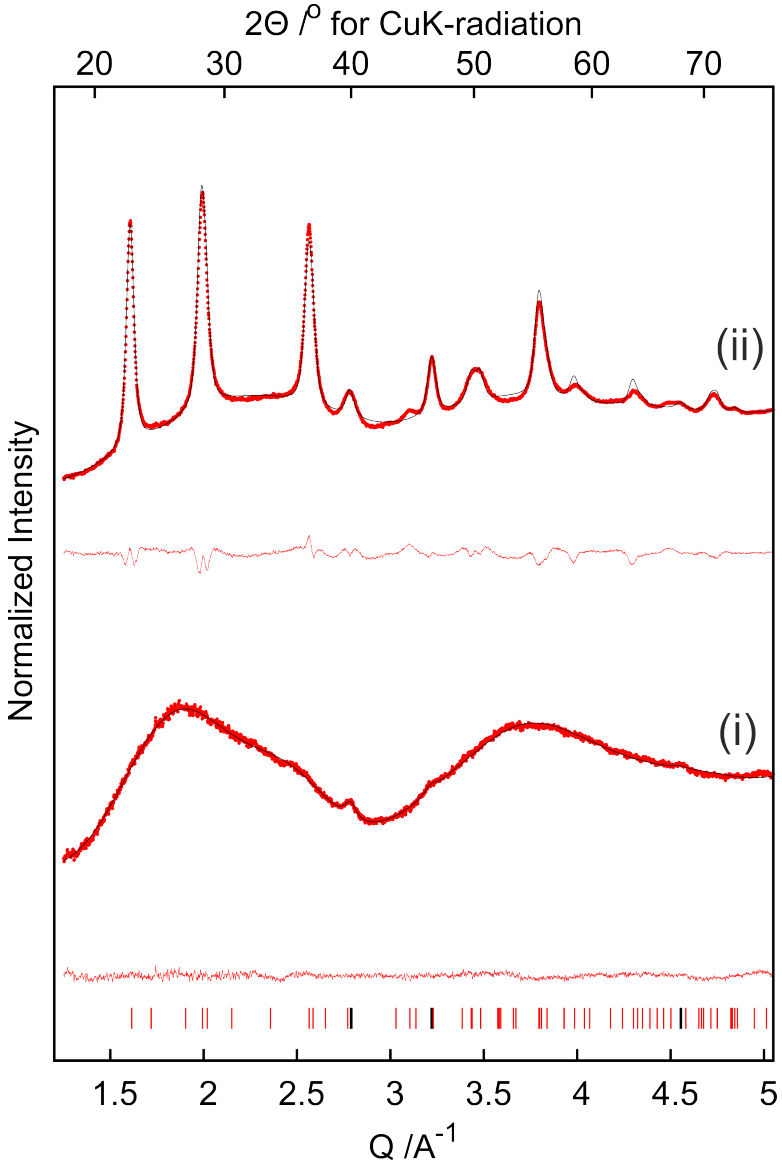

Figure 5.14.: X-ray diffraction patterns and corresponding Rietveld fits (red dots: observed intensity, black line: fit, red line: difference curve) of the Pd@mTa_2O_5 with (i) as synthesized mTa_2O_5 and (ii) heat treated (6 h, 923 K) mTa_2O_5 nanoparticles. Bottom: tick marks for Ta_2O_5 (red) and palladium (black).

Mesoporous structure Figure 5.15 shows the N_2 sorption isotherm (black symbols) as well as the pore size distribution (red symbols) of Pd@mTa_2O_5 nanoparticles. The

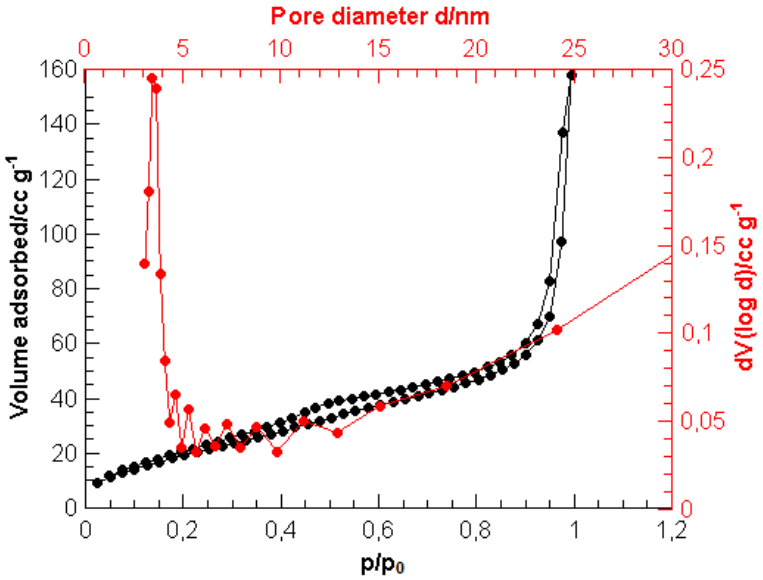

Figure 5.15.: N_2 sorption isotherm (black) and BJH desorption pore-size distributions (red) of Pd@mTa_2O_5 nanocomposite.

overall course of the N_2 sorption isotherms of Pd@mTa_2O_5 resembles that of mTa_2O_5 (see Figure 5.9 a). That is an isotherm with a narrow type IV hysteresis curve. Therefore the initial mesoporous structure is retained upon functionalization with Pd nanoparticles. The surface area, determined by the BET method, is 79 m^2/g which is considerably lower than the 166 m^2/g for mTa_2O_5. This decrease in surface area can be attributed to the mass increase due to functionalization with APTES [254] and Pd nanoparticles. Furthermore some of the Pd nanoparticles might block the pores that they are inaccessible during the measurement. This lowers the determined surface area. [255,256] Further the pore size distribution remains uniform after functionalization as can be seen in Figure 5.15 as well. The average pore size is 3.5 nm which is slightly smaller than the 3.7 nm from before. This decrease might be due to the silane functionalization of the pores in the sample.

5.5. Conclusions

To summarize, a new and simple synthesis for spherical mTa_2O_5 nanoparticles is established that yield mesoporous nanoparticles with high surface areas (above 160 m^2/g)

and uniform pore-sizes. The synthesis is optimized in regard to acid/base, temperature and Pluronic F127 concentration, revealing no templating agent is required. Further the as-synthesized mTa_2O_5 nanoparticles are amorphous and start to crystallize into orthorhombic Ta_2O_5 at 923 K. Upon crytallization, the pores of the mTa_2O_5 nanoparticles expand from 3.7 nm up to 8.1 nm and the pore-size distributions become less uniform. At the same time, the surface area of the Ta_2O_5 decreases (down to 65 m^2/g), as the Ta_2O_5,that make up the mTa_2O_5, start to sinter together. Those findings suggest the mTa_2O_5 form *via* a self-assembly mechanism of small Ta_2O_5 nanoparticles instead of a template mechanism. At higher temperatures (1123 K and beyond) there are still Ta_2O_5 particles in the nanometer size regime but the mesoporous structure is lost.
In the second part of the chapter, the decoration of the mTa_2O_5 with Pd nanoparticles is introduced. Here, the attachment of the palladium was mediated *via* aminogroups that were introduced to the mTa_2O_5 surface with APTES. The amine functionalization was confirmed by FT-IR and ζ-potential measurements. Subsequently, Pd nanoparticles were deposited on mTa_2O_5 nanoparticles, either as synthesized or heat treated (6h at 923 K), in a sonochemical reaction to yield Pd@mTa_2O_5. In both cases the Pd nanoparticles are uniformly distributed on the outer mTa_2O_5 nanoparticles surface and have an average size of 11 nm evidently in the TEM images. Furthermore the Pd@mTa_2O_5 retain their mesoporous structure with a narrrow pore-size distribution around 3.5 nm. The surface area of the Pd@mTa_2O_5 decreased compared to mTa_2O_5 but is still fairly high with 79 m^2/g.

6

Gadolinium doped mesoporous tantalum oxide nanoparticles as multimodal contrast agent

6.1. Abstract

Currently several imaging modalities, such as magnetic resonance imaging (MRI) and X-ray computed tomography (CT), are combined to exploit their complement strengths. This has promoted the interest as contrast agents, that fulfill the requirements of various imaging techniques simultaneously. We have synthesized spherical mesoporous tantalum oxide nanoparticles with high surface areas ($180\,m^2/g$) doped with different amounts of Gadolinium (mTa_2O_5:Gd). Further the mTa_2O_5:Gd were biofunctionalized with Methoxy(polyethyleneoxy)propyltrimethoxy silane (PEG-TES)/3-Aminopropyltriethoxysilane (APTES) and their bio-compatibility was confirmed with cytotoxicity-assays. Moreover, the mTa_2O_5:Gd were functionalized with dye molecules (Fluorescein 5(6)-isothiocyanate, FITC) and their fluorescence and cell uptake was confirmed with fluorescence imaging of immunofluorescence stained cells. The release of Diclofenac out of mTa_2O_5 was monitored. The mTa_2O_5:Gd act as CT as well as T_1 contrast agent and are suitable for optical imaging. Whereby the relaxitivity of mTa_2O_5:Gd changes with the Gd amount and is at its highest for low Gadolinium doping.

6.2. Introduction

In recent years, much effort has been put in the improvement of bioimaging techniques for the detection of diseases. Currently, the imaging techniques in clinical use are computed X-ray tomography (CT), magnetic resonance imaging (MRI), positron emission

tomography (PET), ultrasound (US) imaging and single-photon emission computed tomography (SPECT).[257,258] Yet, the inherent contrast of the examined (soft) tissues is often not sufficient for most imaging methods. Therefore contrast agents (also imaging probes) are required, which improve the signal-to-noise ratio, sensitivity and/or resolution.[40,259] Further every method has its own intrinsic strengths and limitations. They differ in terms of imaging depth, sensitivity, spatial and temporal resolution, anatomical and molecular contrast, exposure time and radiation load.[260,261] Consequently different imaging techniques are combined which is called multimodal imaging.[246,262] This allows to circumvent their complement weaknesses and exploit the strengths of various techniques at the same time.[258] The combination of imaging modalities leads to new challenges in the design of contrast agents. Since every imaging modality has its own prerequisites in regard to contrast enhancement, contrast agents have to balance the requirements of the employed methods. In particular, nanoparticles are suitable candidates for multimodal imaging, as their properties can be well tailored in regard to size, composition, optical and magnetic features. Furthermore they have a high surface-to-volume ratio which allows rational surface functionalization for enhanced targeting and prolonged circulation times.[40,262–264]

CT is one of the most widely used non-invasive clinical imaging techniques owing to its cost efficiency, wide availability and unlimited penetration depth.[61,265] The principle of CT imaging is based on the attenuation of X-rays in matter due to absorption and scattering. The degree of X-ray attenuation is given by the Lambert-Beer law:

$$I = I_0 \exp^{-\mu x} \tag{6.1}$$

Where I_0 is the initial intensity compared to the intensity I after permeating tissue of the thickness x. μ, the mass attenuation coefficient, is a substance specific intrinsic property, that is highly depending on the atomic number Z ($\mu \propto Z^3$). For a sufficient CT contrast, which is expressed in Hounsfield units (HU), the attenuation difference has to be high. The contrast between bones and soft tissues is adequate, while it is hard to differentiate soft-tissues having low inherent contrast differences. Therefore CT contrast agents require elements with high atomic numbers. Further prerequisites for contrast agents are a good solubility in physiological media and biocompatibility, long circulation times and target specificity.[43,259] Currently, most CT contrast agents contain water soluble iodinated (Z=53) molecules such as derivates of 1,3,5-triiodobenzene.[43,265,266] The main disadvantages of iodinated molecules are the short circulation time as well as the high viscosity and osmolality - that have adverse effects for the patient.[267] To avoid those

disadvantages iodine is introduced into nanosized carriers such as micellar nanoemulsions, polymers, metal organic frameworks (MOFs), liposomes or dendrimers.[43,265,268] Alternatively inorganic nanoparticles with high Z contrasts are tested as CT contrast agents. They have prolonged circulation times and a versatile surface chemistry that allows functionalization for tissue specific uptake. Typical examples are Gold,[246,269,270] lanthanide based NP[271] and bismuth sulfide.[272–274] Further, tantalum oxide was demonstrated to be a suitable CT contrast agent.[39,61,192,275–278] It shows promising properties such as a high X-ray attenuation (Z=73) which is comparable to Au (Ta, 4.3 and Au, 5.16 cm^2 at 100 eV[61]) although Tantalum is much cheaper than Gold. Moreover, tantalum oxide is biocompatible and inert especially when compared to Bi_2S_3 due to the intrinsic toxicity of Bi. Furthermore the surface functionalization is diverse as the surface chemistry closely resembles that of silica and can be adapted.
Next to CT, MRI is the most common 3D imaging technique in clinical use. It provides a high spatial resolution, strong soft tissue contrast, no depth limitation and no radiation risks.[41,258,260,278] The disadvantages of MRI are the high cost and low sensitivity. The underlying principle of MRI is nuclear magnetic resonance (NMR) where water Protons (^{1}H) get excited. Briefly, the proton spins align parallel or antiparallel in an external magnetic field (B_0). At the same time the spins precess with the Larmor frequency ($\omega_0 = \gamma B_0$, γ gyromagnetic constant). When a strong radio-frequency (RF) pulse is applied perpendicular to B_0 the spins realign themselves according to the RF pulse generating a transverse magnetization and a decreased longitudinal magnetization. There are two different pathways for spin relaxation which are denominated longitudinal (T_1) and transverse relaxation (T_2). Longitudinal relaxation describes how the decreased net magnetization recovers, when the spins flip back into their initial orientation.[41,47] This is mediated via an energy transfer from the proton spin to the surrounding medium. Differences in the relaxation are caused by chemical differences in the medium that either increases or decreases the energy transfer (spin-lattice-relaxation). Upon RF excitation the spins are in phase. During transverse relaxation, T_2, the spins dephase and the induced magnetization in the perpendicular plane is lost. Here, the contrast originates from the differences in the magnetic field that the protons experience due to local magnetic field gradients influencing how fast the spins randomize (spin-spin-relaxation). Depending on the relaxation process the used contrast agents are denominated T_1 and T_2 respectively. Typical T_2 contrast agents are based on iron oxide or other magnetic oxides nanoparticles with high magnetization like MFe_2O_4 (M=Mn, Co, Ni).[279–281] Their high magnetic moment disturbs the external field and causes local inhomogeneities leading to faster dephasing. Thus T_2 contrast agents cause a decreased signal intensity

which shows as a darkening in the MRI images. Nevertheless, T_2 contrast agents exhibit several disadvantages as the dark contrast leads to a lower contrast compared with T_1 images. The dark areas might conceal pathogenic conditions, that show a darkening in the MRI images as well. Further the magnetic particles can also cause a perturbation of the magnetic field in the surrounding healthy tissue which obscures the images.[42] As a consequence T_1 contrast agents are favored in MRI imaging. Typical T_1 contrast agents are characterized by unpaired electrons or surface spins shortening the longitudinal relaxation which gives rise to positive contrast. In this regard, MnO nanoparticles have been proposed as T_1 consrast agents as they possess uncompensated surface spins.[47,282] Commercially, Gadolinium(III) complexes are applied e.g. Gd-DTPA (Magnevist) or Gd-DOTA (Dotarem).[283–285] Due to the inherent toxicity of Gd^{3+}, ions are either bound in stable complexes,polymers, nanoparticles or porous structures.[284,286–289]
In this work, the Gadolinium ions are enclosed in mesoporous tantalum oxide nanoparticles to avoid free Gd^{3+} and leaves free surface groups for further functionalization.[287] Additionally the high surface area of mesoporous tantalum oxide allows for many Gd^{3+} to be close to the surface. In this way the MRI active Gadolinium is combined with CT active tantalum oxide to act as CT/MRI dual imaging contrast agent. As Gadolinium is used as a dopant it is possible to tune the amount of Gadolinium relatively to Tantalum. This takes the higher sensitivity of MRI compared to CT into account. In addition other imaging modalities can be introduced via surface functionalization with imaging probes. Optical imaging constitutes as a complementary imaging method to CT and MRI.[39,264] Since optical imaging provides a high resolution and sensitivity at a cellular level that CT and MRI lack.[264] However, the 3D and spatial resolution of optimal imaging is insufficient and needs to be supported by CT and MRI data. For optical imaging dye molecules can be introduced to the nanoparticle surface or its capping molecules.
In addition, mesoporous nanoparticles can be used as carriers for drug delivery of therapeutic agents can either be loaded into the pores or can be attached to their large surface. Therefore mesoporous tantalum oxide nanoparticles are suitable for theranostic applications which combine **thera**py and diag**nostic** in one platform.
This section describes the synthesis of mesoporous tantalum oxide nanoparticles doped with different amounts of Gadolinium. Further the impact of the Gadolinium doping upon mTa_2O_5 nanoparticles is assessed in regards to morphology and mesoporosity. Following the nanoparticles are functionalized with a polyethylene glycol (PEG) silane and amine silane (APTES) for further functionalization and biocompability which is proved subsequently. Additionally the nanoparticles are connected to a dye for fluo-

rescence imaging. Then the ability of the mTa_2O_5:Gd to act as a CT as well as MRI contrast agent is demonstrated. Herein, the relaxivity of the mTa_2O_5:Gd is investigated in relation to the amount of Gd in the nanoparticles. Furthermore the mTa_2O_5 are loaded with diclofenac and its release out of the pores is monitored.

6.3. Experimental

Materials All starting materials were used without further purification or treatment. Methoxy(polyethyleneoxy)propyltrimethoxy silane (PEG-TES) (90%, 9-12 PE units), and Gadolinium isopropoxide (Gd(O^iProp)$_3$) (99.9% REO) were purchased from abcr. Pluronic F-127, Tantalum(V) *n*-butoxide (Ta(OnBu)$_5$) (99.99%),fluorescein 5(6)-isothiocyanate (FITC), acetone (p.a.), concentrated ammonia (NH_4OH), cyclohexane (p.a), acetone (p.a.), triethylamine (≥99%), and 3-aminopropyltriethoxy silane (APTES) (≥98%) were obtained from Sigma Aldrich.

Synthesis

Synthesis of mTa_2O_5:Gd In a typical synthesis, 0.30 g of Pluronic F127 and Gd(O^iProp)$_3$ (3, 6,12, or 16 mg) were dissolved in 5 mL absolute ethanol in an ultra sonic bath. Under constant stirring 0.23 mL (0.53 mmol) of Ta(OnBu)$_5$ were added in a dropwise manner. After stirring for 4 h the solution was poured into 20 mL of water and transferred into a 50 mL Teflon lined autoclave. The autoclave was kept at 473 K for 8 h. When the autoclave had cooled down to ambient temperature the colorless product was collected by centrifugation (15 min, 9000 rpm). Then it was washed with 15 mL of ethanol twice.

Synthesis of mTa_2O_5:Gd with higher Gd concentrations Typically 0.30 g of Pluronic F127 and Gd(O^iProp)$_3$ (45 mg) were dissolved in 10 mL absolute ethanol in a ultra sonic bath and stirred overnight. Ta(OnBu)$_5$ (0.23 mL, 0.53 mmol) was added drop by drop and stirred for 4 h before the solution was poured into 15 mL of water. The reaction solution was transferred into a 50 mL Teflon lined autoclave and heated to 473 K for 8 h. The obtained colorless product was centrifuged (15 min, 9000 rpm) and the supernatant was discarded. Subsequently, the product was washed with absolute ethanol (15 mL) twice.

mTa_2O_5:Gd-PEG-APTES The reaction was carried out in an argon atmosphere. For ligand functionalization 10 mg of mTa_2O_5:Gd were dispersed in 20 mL of actone and 150 μL NH_4OH were added. After stirring for 5 min, 150 μL APTES and 150 μL PEG-TES were injected into the reaction solution. The reaction continued over night. Then the solution was concentrated to 3-5 mL under reduced pressure on a rotary evaporator (bath temperature 313 K). The product was precipitated with cyclohexane (30 mL), centrifuged (6 min, 6000 rpm) and redispersed in 5 mL aceton. This step was repeated twice, before the nanoparticles were dispersed in 5 mL of ethanol.

mTa_2O_5:Gd-PEG-FITC All reaction steps were performed under argon atmosphere in the dark. mTa_2O_5:Gd-PEG-APTES was dispersed in 10 mL of ethanol before 2 mg of FITC were added. The solution was stirred for 24 h in the dark. The product was precipitated with cyclohexane and centrifuged (10 min, 9000 rpm). The particles were redispersed in 5 mL of ethanol, precipitated with cyclohexane and centrifuged (10 min, 9000 rpm). The product was stored in 5 mL ethanol in the dark at 281 K.

Drug load and Drug release 30 mg of 2-[2-(2,6-Dichlorophenylamino)phenyl]acetic acid) (diclofenac) dissolved in 10 mL cyclohexane were added to 30 mg of mTa_2O_5 in 10 mL of cyclohexane. The dispersion was stirred over night. Then the dispersion was centrifuged (15 min, 9000 rpm) and the supernatant was discarded. Carefully 40 mL of PBS buffer (phosphate buffered saline) were layered over the nanoparticle precipitate. Aliquotes (0.5 mL) were taken between 1 min and 27 h and the absorption was measured *via* UV-VIS.

Materials Characterization

TEM, HRTEM, EDX The nanoparticles were characterized using a Philips EM420 TEM with an acceleration voltage of 120 kV. For sample preparation a dilute ethanolic solution was dropped on a carbon coated copper grid. HRTEM images and EDX spectroscopy were acquired on a FEI Tecnai F30 S-Twin microscope with a 300 kV field emission gun. HRTEM images were collected with a CCD camera (14-bit GATAN 794MSC). For a quantitative EDX analysis carbon coated nickel grids were used to avoid the overlap of the Ta L-lines (11.67 – 7.173 keV) with the Cu K-lines (8.048 – 8.028 keV). EDX line scans were acquired and quantified with the Emispec ESVision software.

XRD Powder X-ray diffraction patterns were recorded with a Siemens D5000 diffractometer equipped with a Braun M50 position sensitive detector in transmission mode using Ge (200) monochromatized CuKa radiation.

N_2 sorption experiments Nitrogen sorption experiments were performed with a Quantachrome autosorb 6B instrument. The adsorbate gas is N_2 at 77 K. The multipoint Brunauer-Emmett-Teller (BET) method was employed to determine the specific surface area. The pore size distribution and volume were calculated with the Barrett-Joyner-Halenda (BJH) method of desorption. Before analysis the samples were dried in a vacuum oven (318 K) overnight.

Inductively Coupled Plasma Mass Spectrometry Inductively coupled plasma mass spectrometry (ICP-MS) was measured with a ICP-Quadrupol-MS (ICP-Q-MS) with a collision reaction chamber Agilent 7700x (Agilent Technologies, Waldbronn Germany). The sample was introduced into the ICP-Q-MS with a CETAC autosampler and a PFA nebulizer via a PFA-Scott chamber (at 275 K). Every sample was measured twice with 5 cycles. For sample preparation, the nanoparticles were dissolved in concentrated hydrofluoric acid. The solutions were diluted with 3% HNO_3 and 0.2% hydrofluoric acid.

UV-VIS UV-VIS spectra were collected with a Cary Varian 5G UV-VIS-NIR spectrometer.

Fourier Transformed Infrared Spectroscopy FT-IR spectra were measured on a Bruker Tensor 27 spectrometer. The samples were prepared in a KBr pellet.

Zeta potential Zeta potential (ζ-potential) measurements were conducted with a Malvern Zetasizer Nano-ZS. Nanoparticles were either dissolved in ethanol or water before they were filterd with a Millex-GS syringe filter (pore-size 0.22 μm). The surface potenial was determined by 2x15 single measurements at T=298 K.

Cytotoxicity-assay For a cytotoxicity-assay a cervical carcinoma cell line (HeLa) was used. Cells were cultured in DMEM/Ham´s F12 (Sigma Aldrich), supplemented with 10% FCS (Sigma Aldrich) and antibiotic solution (100 μg/mL penicillin and 100 μg/mL streptomycin, Sigma Aldrich) at 310 K in 5% CO_2. In order to analyse cell viability after

treatment with the mTa_2O_5:Gd-PEG-FITC nanoparticles (filtered through aMillex-GS syringe filter (pore-size 0.22 μm), 15000 cells/well were seeded in a 96 well plate and cultivated over night for adherence. Next day, the cells were treated with the nanoparticles in the final concentrations (12.5, 25, 50, 100 and 200 μg/mL) for 24 h. After incubation 100 μL of 70% ice cooled ethanol was added to the cells used for death control for 10 min. The medium was replaced with 200 μL FCS-medium and 10% Alamar Blue (Biozol Diagnostica, Eching, Germany) for all wells. Subsequently the 96 well plate was incubated for 3 h at 310 K. The results were obtained with the aid of a plate reader (excitation. 540 nm, emission:600 nm) (Fluoroskan Ascent Microplate reader,Thermo Fisher Scientific GmBH, Rockford, USA). The values were normalized to the untreated control.

Immunofluorescence staining The cells were fixed with 4% paraformaldehyde and methanol and subsequently washed three times with Phosphate Buffered Saline (PBS). Nonspecific interactions were blocked with 1% Bovine Serum Albumin (BSA)/PBS. Afterwards these cells were expoxed to Alexa Fluor® 555 Phalloidin (5 μL/200 μL v/v, Cell Signaling, Danvers, USA) for 20 min. The coverslips were mounted on glass slides utilizing DAKO fluorescet mounting medium (DAKO, Inc., Carpinteria, CA, USA). All slides were examined using an inverted microscope (Nikon ECLIPSE TE2000-U).

Computed Tomography and Magnetic resonance imaging Magnetic resonace imaging (MRI) measurements were performed on a clinical 3.0 Tesla (Magnetom Trio, Siemens Medical Solutions, Erlangen, Germany) by means of a T_1 measurement using a spoiled gradient echo (SRGE) with variable repetition time.

6.4. Results and Discussion

A schematic representation for the synthesis and functionalization of Gadolinium doped mTa_2O_5 NP is illustrated in Figure 6.1. First, the $Ta(OnBu)_5$ and $Gd(O^iProp)_3$ are mixed in ethanol and aged under stirring for several hours to yield a Tantalum-Gadolinium containing colloid. Then mTa_2O_5:Gd form through a rapid self-assembly process when the precursor solution is poured into water.

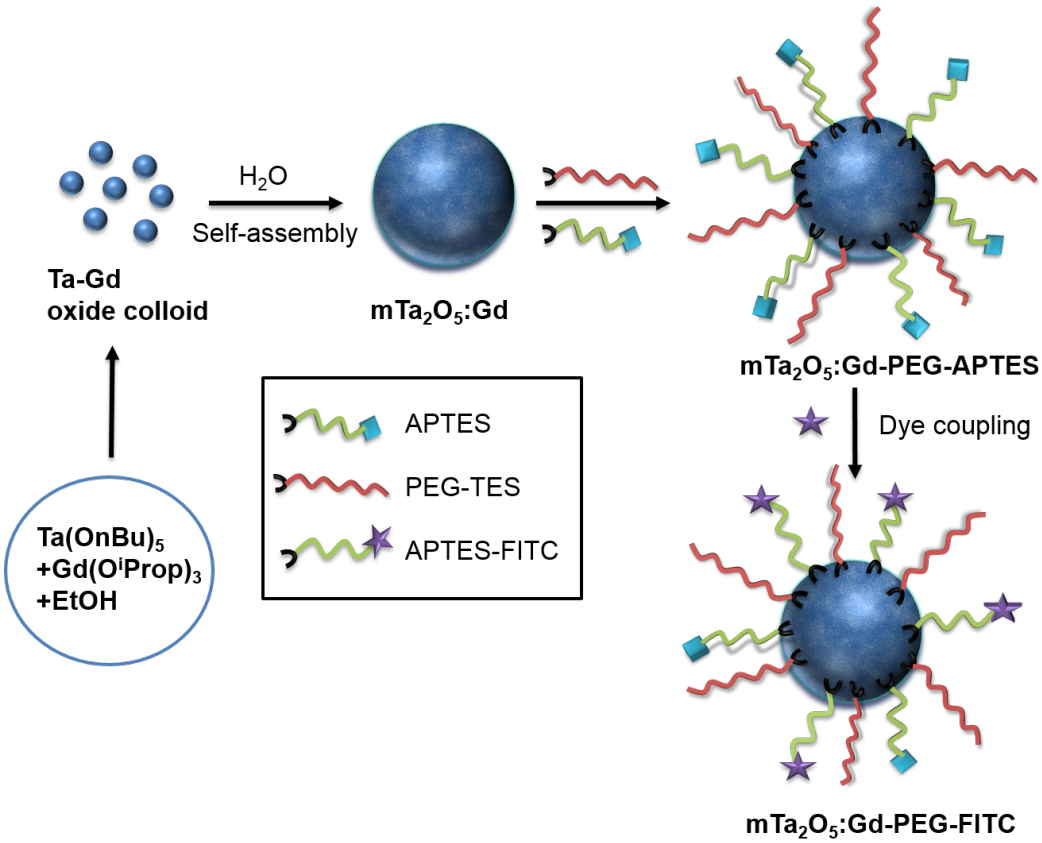

Figure 6.1.: Schematic illustration of the synthesis of the mTa_2O_5:Gd and their subsequent functionalization.

In a second step, the mTa_2O_5:Gd are functionalized with APTES and PEG-TES *via* condensation of silane groups onto the tantalum oxide surface.[290] The attachment of PEG groups is used both to increase the water solubility of the nanoparticles as well as ensure their biocompatibility. While the free amino groups allow further conjugation of other functional molecules onto the nanoparticles. The free NH_2 groups are exploited in a subsequent step when dyes like FITC are bound to them.

6.4.1. Structural characterization of Gadolinium doped mesoporous tantalum oxide

Morphology. The morphology of the mTa_2O_5:Gd nanoparticles is characterized in dependence on the Gd amount using TEM. Representative TEM overview images for different Gd concentrations are shown in Figure 6.2. Figure 6.2 a depicts pure mTa_2O_5 nanoparticles that are polydispers with a spherical morphology. Likewise mTa_2O_5:Gd with nominal Gd concentrations between 1.5% (see Figure 6.2 b) and 9% (in Figure 6.2 e) yield spherical particles with similar size distributions. The diameter of the particles is between 20 and 200 nm for those samples. Thus, the particle morphology and size are independent of the Gd concentration in this concentration regime.

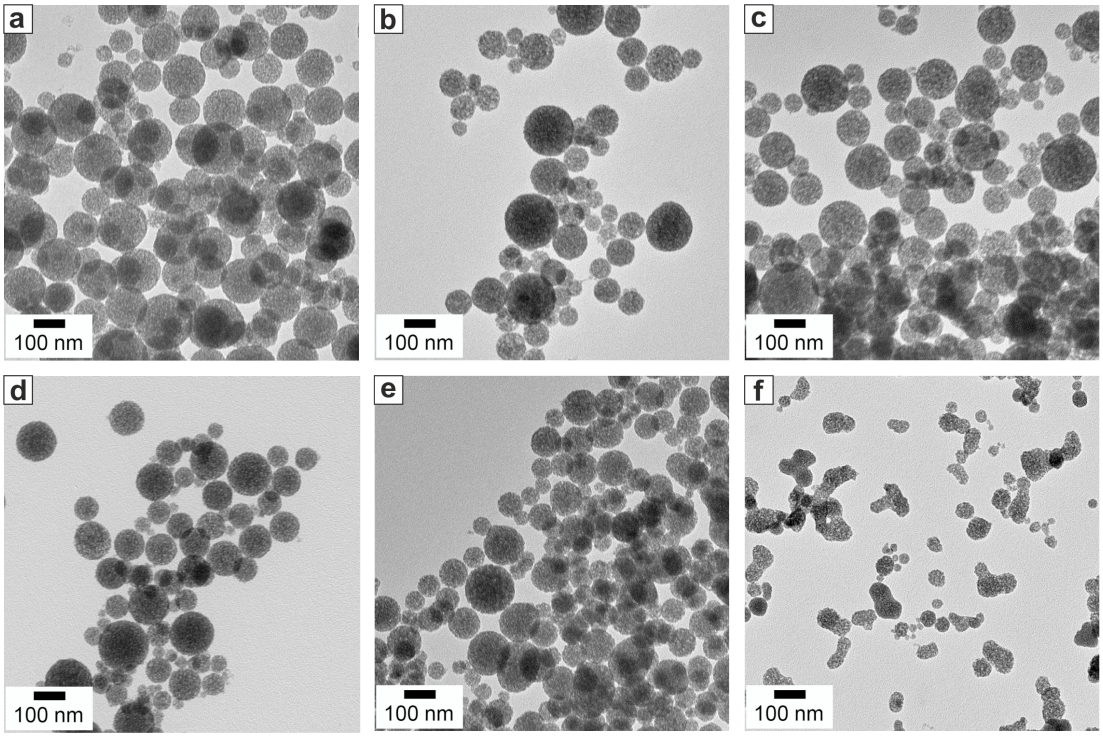

Figure 6.2.: TEM micrographs of the mTa_2O_5:Gd with a nominal Gd amount of a) 0% b)1.5% c) 3% d) 6% e) 9% f) 25%.

As opposed to low Gd concentrations, mTa_2O_5:Gd, with a nominal Gd amount of 25%, have a less uniform morphology. While they consist of some spherical particles, most of the nanoparticles are dumbbell or tri- or tetrapod shaped. These structures emerge, as the spherical mTa_2O_5 start to agglomerate. Thus, high Gd concentrations seem to

affect the self-assembly of the small Ta_2O_5 NP into mTa_2O_5. However, the limited solubility of $Gd(O^iProp)_3$ in ethanol has to be accounted for as well. Due to this 10 mL instead of 5 mL ethanol are used (the water amount was decreased accordingly) which is also slightly detrimental for morphology control.
All mTa_2O_5 nanoparticles exhibit a grainy texture in the TEM images. This can be attributed to small nanosized particles that agglomerate to mesoporous nanoparticles.

Composition. Often, the actual concentration of the dopant in the product differs drastically from the amount ratio used during the synthesis.[291] Therefore, it is essential to determine the actual molar ratios. For this purpose the real Ta:Gd ratio in the nanoparticles is investigated using ICP-MS. An overview of the obtained molar fraction of Gd compared to Tanatalum is given in table 6.1 (on page 95). The percentage of Gd, relative to the Tantalum amount, ranges between 0.02% for the sample with a nominal amount of 1.5% and 1.54% for the nanoparticles with nominally 25%. Thus all actual concentrations are considerably lower, by some orders of magnitude, than the nominal percentages. The actual Gd ratio, however, is not directly proportional to the nominal values. Nevertheless the real Gd amount increases when more Gd is used. These findings may suggest a non homogenous mixture in the Tantalum-Gd oxide colloid. So when tantalum oxide precipitates in water the percentage of enclosed Gd oxide may vary. Additionally, the different Pearson hardness of Gd and Tantalum as well as the presumably distinct hydrolysis rates impede the enclosing of Gd in the mTa_2O_5 nanoparticles. When the precursors are incompatible there is no inclusion in the mTa_2O_5 which was the case for europium when europium(III)chloride was used as dopant. Likewise it is not possible to embed nanoparticles during synthesis as they disrupt the formation of mTa_2O_5 nanoparticles.
In addition an EDX line scan illustrates the distribution of the Gd in the mTa_2O_5:Gd nanoparticles. Figure 6.3 provides a STEM image of mTa_2O_5:Gd nanoparticles (on the left side). The corresponding line scans are presented on the right. The orange line, in the STEM image, represents the examined area.
The EDX line scan shows the element concentration at any given point along the orange line. This line starts next to the nanoparticles, where no elements are counted (the carbon line is deleted as the measurement is carried out on a carbon coated grid). On the edge of the particles, the counts on Ta, Gd and O rise simultaneously. The concentration for those elements remains on a high level over the whole particles. At the particle boundary the concentration drops again for all three elements. The simultaneous drop implies Ta and Gd are colocalized in the nanoparticles. The concentration of Gd is low

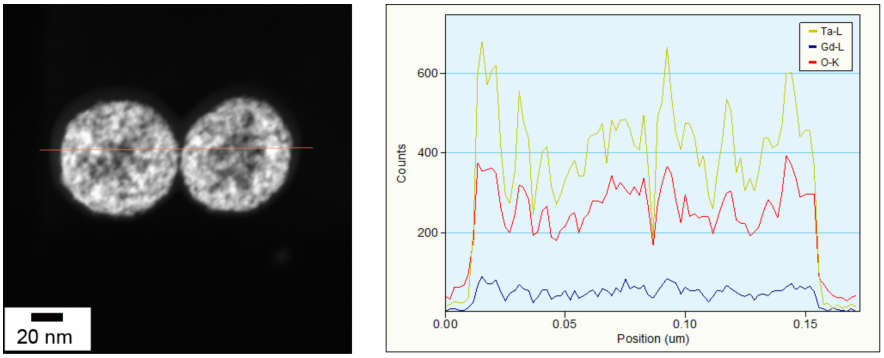

Figure 6.3.: Left: STEM image of mTa_2O_5:Gd with 1% of Gd and on the right: corresponding EDX line scan.

compared to Ta but detectable still. That is in good agreement with the small amount of Gd in the sample determined using ICP-MS.
Alternatively it might be possible that the Gd is not inside the nanoparticles but only on the surface. Yet a mere attachment of Gd ions to the surface of tantalum oxide is highly unlikely as there were several washing steps before the Gd concentration was determined.
However, from an application point of view relatively low Gd concentrations are desired. CT and MRI have a varying sensitivity and therefore require different concentrations of contrast agents for good contrast enhancement.[261,262,292] MRI needs micromolar concentrations of contrast agents. Compared to MRI, CT has a lower sensitivity and necessitates milimolar concentrations.[265] Therefore a optimal performance as bimodal contrast agents is expected for Gd concentrations under 1%.

X-ray diffraction. For further characterization, the crystallinity of the as synthesized mTa_2O_5:Gd is investigated. The crystallinity of pure mTa_2O_5 was already discussed in chapter 5.4.2. An exemplary XRD pattern of mTa_2O_5:Gd is plotted in Figure 6.4. There are no discernable reflexes present in the X-ray diffractogram for all mTa_2O_5:Gd. Thus the mTa_2O_5 are amorphous like pristine mTa_2O_5. When the mTa_2O_5 are heat treated (6 h at 923 K) they crystallize as phase pure orthorhombic Ta_2O_5 (Ta_2O_5-$oP14$) as described for mTa_2O_5 nanoparticles (see chapter 5.4.2). No gadolinium oxide phase can be found as the amount of Gadolinium in all samples is under the limit of detection for powder X-ray diffraction (especially of nanoparticles).

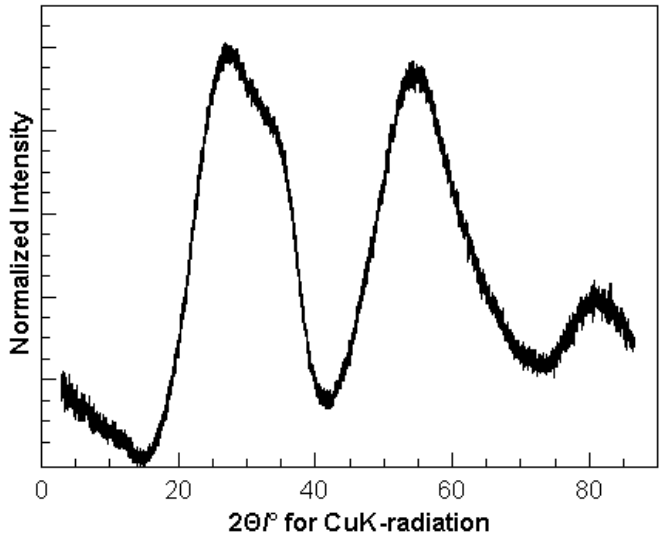

Figure 6.4.: XRD pattern of the as synthesized mTa_2O_5:Gd nanoparticles with a nominal amount of 6% Gd.

Mesoporous structure. N_2 sorption experiments are performed to evaluate whether the Gadolinium doping has an impact on the surface area and mesoporosity or not. Table 6.1 summarizes the obtained data, whereas Figure 6.5 shows an exemplary N_2 sorption isotherm and pore distribution of mTa_2O_5:Gd nanoparticles (with 6% nominal Gadolinium amount). In Figure 6.5 the N_2 sorption isotherm (black symbols) of

Table 6.1.: Composition and structural parameters of the mTa_2O_5:Gd nanoparticles in dependence on the Gd concentration.

Gd amount		S_{BET}/	Pore size/	Pore Volume/
nominal/%	actual /%	m^2g^{-1}	nm	cm^3g^{-1}
0	0	166	3.7	0.384
1.5	0.02	133	3.9	0.464
3	0.24	117	3.9	0.300
6	0.10	188	3.7	0.368
9	0.81	114	3.7	0.342
25	1.54	103	3.7	0.442

mTa_2O_5:Gd depicts a typical type IV hystersis curve with narrow hysteresis.[241] This suggests the presence of uniform mesopores in the sample. The surface area is 188 m^2/g, which is even higher than the surface area for pristine mTa_2O_5 with a surface area

of 166 m^2/g (see table 6.1, discussed in chapter 5.4.2). Figure 6.5 also presents the associated BJH pore-size distribution (red symbols). The pore-size distribution is slim which confirms the presence of monodisperse pore-sizes. As the maximum is at 3.7 nm this is the average pore-size. This confirms, that in this case, the mesoporosity is not ill affected by Gadolinium doping.
Taking the other mTa_2O_5:Gd with different Gadolinium amounts into consideration, there is no apparent influence on the pore size by Gadolinium doping. As the pore sizes are either 3.7 nm or 3.9 nm (see table 6.1), which is not significantly different. Additionally there is no consistent trend in surface area as well, as the values range between 103 and 188 m^2/g for all samples. Although the surface area of the mTa_2O_5:Gd nanoparticles is the smallest for the highest Gadolinium amount. This, however, is in good agreement with its morphology that is more agglomerated than the other samples. To conclude the Gadolinium doping does not compromise the mesoporosity of mTa_2O_5.

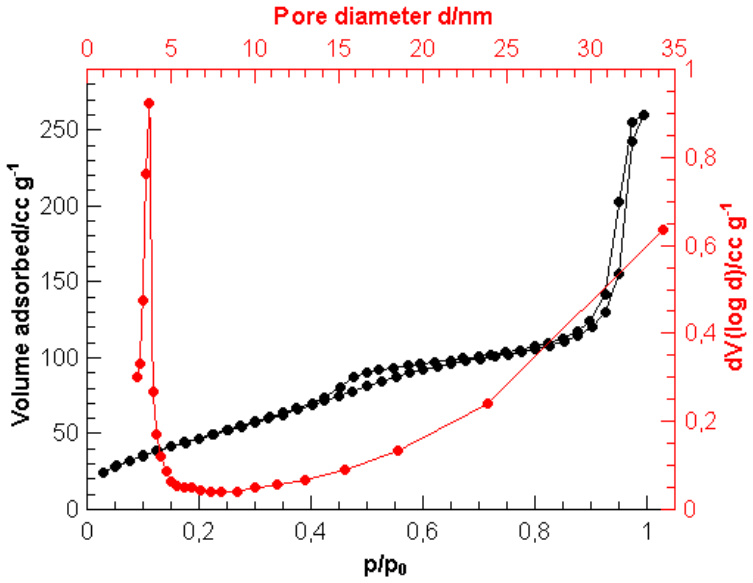

Figure 6.5.: N_2 soprtion isotherm (black) and BJH desorption pore-size distributions (red) of mTa_2O_5:Gd with a nominal Gd amount of 6%.

6.4.2. Surface functionalization and biocompatability

Biofunctionalization. For biomedical applications the surface modification of nanoparticles is a crucial step.[14,33] Without a suitable ligand shell, the nanoparticles might not be soluble in bloodstream and agglomerate. Alternatively they are prone to opsonisation and cleared via the reticulo endothelial system (RES).[293–295] Opsonisation

is a defence mechanism of the immune system where certain serum proteins (Opsonins) bind to the particle surface. This targets the particles for destruction by phagocytes. To avoid a negative immune response, PEG ligands are commonly used for NP stabilization *in vivo* due to their suitable properites.[293,294] Generally PEGs are water soluble and stable in biological conditions. In addition, they provide "'stealth"' to the nanoparticle cores from opsonisation and thus enable long circulation times in blood.[263,296,297] In this case PEG-TES, a PEG silane, was used. The ligand was covalently bound to the surface via a condensation reaction between the silane group and surface hydroxyl groups (see also chapter 5.4.3). One of the advantages of a covalent attachment is the better long term stability, as the ligands cannot dissociate in contrast to coordinative binding.[293,294] Moreover an amine group in the form of APTES is introduced to the surface *via* a condensation reaction between the silane group of APTES and hydroxyl groups on the tantalum oxide surface for further biofunctionalization.
The functionalization with PEG-TES and APTES is confirmed using FT-IR spectroscopy as illustrated in Figure 6.6 a. For mTa_2O_5:Gd the IR spectrum shows the typical bands

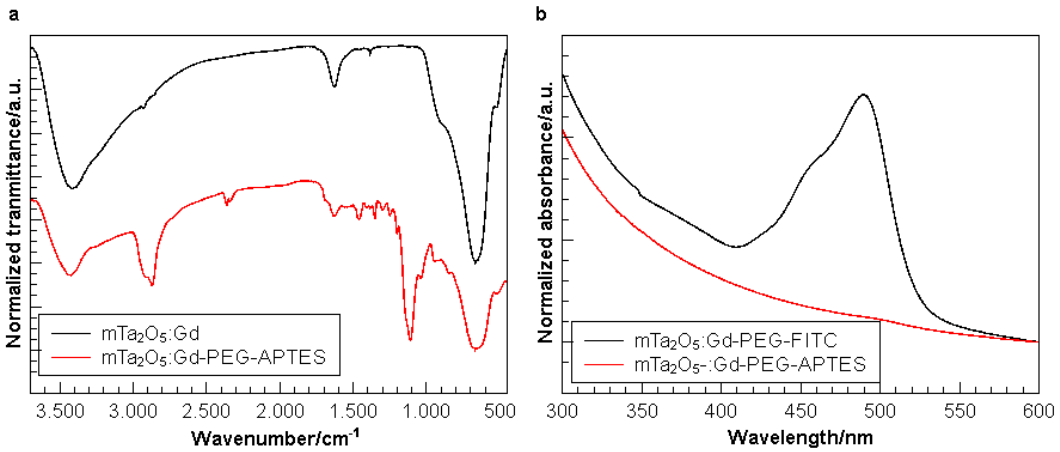

Figure 6.6.: a) IR spectra of the mTa_2O_5:Gd and mTa_2O_5:Gd-PEG-TES nanoparticles. b) UV-VIS spectra of mTa_2O_5:Gd-PEG-TES and mTa_2O_5:Gd-FITC-PEG nanoparticles in water.

of Ta_2O_5. The Ta-O-Ta and Ta-OH stretching bands appear at 664 cm^{-1} and 3420 cm^{-1} respectively.[249] Additionally there is the corresponding -OH bending band attributed to either absorbed water or the surface hydroxyl groups at 1627 cm^{-1}.[250] After functionalization with PEG-TES and APTES, all those bands are still present. Further there are also two bands at 2918 and 2841 cm^{-1} that belong to the CH_2 symmetric and asymmetric stretching bands of the alkyl moiety in PEG-TES. The C-O-C stretching

vibration of the ether groups in the PEG causes the bands at 1468 cm^{-1} and 1350 cm^{-1}. The strong band at 1108 cm^{-1} is due to symmetric and asymmetric stretching vibration of O-Si-O. At 1455 cm^{-1} the N-H bending vibration gives rise to a weak broad band. Thus the IR spectrum of mTa_2O_5:Gd-PEG-APTES supports the successful functionalization of mTa_2O_5:Gd with PEG-TES and APTES.
In addition the ζ-potential is measured for pristine mTa_2O_5 and the mTa_2O_5-PEG-TES. For mTa_2O_5 the ζ-potential is 0 mV ,whereas it is 11 mV for mTa_2O_5-PEG-TES. The increase in the ζ-potential is typical for an amine functionalization (see chapter 5.4.3), given the amine group is protonated at neutral pH values.[251,252] Hence the ζ-potential supports the functionalization of the mTa_2O_5 with amine groups.
Furthermore, UV-VIS spectra of mTa_2O_5:Gd-PEG-APTES and mTa_2O_5:Gd-PEG-FITC are recorded as displayed in Figure 6.6 b. For mTa_2O_5:Gd there is no apparent absorption band only a steady slope at decreasing wavelength. This increase in absorbance can be attributed to scattering caused by the nanoparticles. In contrast the mTa_2O_5:Gd-PEG-FITC nanoparticles exhibit a strong absorbance band at 490 nm corresponding to FITC. Thus the dye coupling is confirmed using UV-VIS spectroscopy. Generally this demonstrates that the amines from APTES are accessible and other molecules, like antibodies for cell targeting,[270,298] can also be introduced to the nanoparticles.
Another common method labeling amorphous nanoparticles with dyes is to incorporate the dye in the particle itself.[290,292,299] Principally this strategy also works with mTa_2O_5 nanoparticles because Gadolinium is doped in the same fashion. The dye molecules are readily built in the nanoparticles, which can be observed by the color change in the sample. Except they rapidly degrade due to the photocatalytic activity of Ta_2O_5 described in chapter 4.4.4. Therefore a spacer is required between dye molecules and the tantalum oxide surface.

Cell tests. In order to assess the biocompability of the mTa_2O_5:Gd-PEG-FITC nanoparticles cervical carcinomal cells (HeLa) are incubated with the NP for 24 h. Subsequently the viability in the cells is determined as illustrated in Figure 6.7. The viability was measured for mTa_2O_5:Gd-PEG-FITC with different Gadolinium concentrations. The surveyed NP concentrations were between 12.5 and 200 μg/mL for all samples. In nearly all cases the viability of the cells is above 80% which is usually considered as the threshold for toxicity (in some instances a viability above 60% is considered untoxic). The only exception is undoted mTa_2O_5:Gd-PEG-FITC where the viability is slightly lower with 77% at 200 μg/mL. Generally there is neither a discernable trend in viability with the Gadolinium amount nor with the concentration of the nanoparticles.

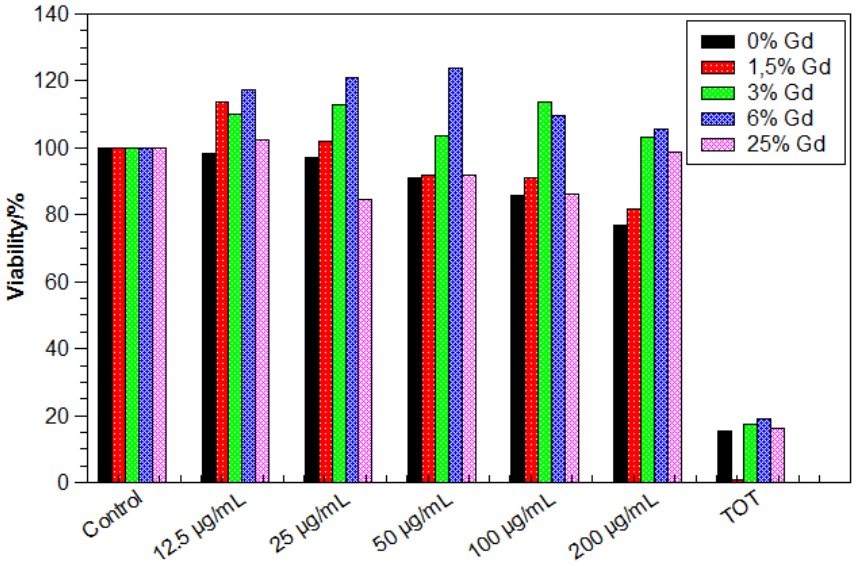

Figure 6.7.: Cytotoxicity-assay of the mTa_2O_5:Gd-PEG-FITC NP performed with different nominal Gadolinium amounts (between 0% and 25% Gd). The HeLa cells were grown overnight before they were incubated with the NP for 24 h.

Altogether the particles show no pronounced toxicity and can be deemed save for further biomedical testing. The low toxictiy of tantalum oxide is in good agreement with the literature as described by Oh et al..[61] Free Gd^{3+} ions, on the other hand, are known to be toxic.[41,262,283,300] Therefore the Gd^{3+} ions have to be bound either in a stable complex or inside of nanoparticles.[301] Here free Gadolinium ions were avoided by introducing the Gadolinium into a tantalum oxide matrix. The Gadolinium appears to be tightly bound as there is no increase in toxicity with ascending Gadolinium amount which would be expected for a toxic compound.

In a next step, fluorescence images of the cells incubated with mTa_2O_5-PEG-FITC nanoparticles are taken to determine whether the particles are internalized in the cells. Further the fluorescence images can confirm the successful dye functionalization of the nanoparticles. Figure 6.8 shows the fluorescence images of cell with different mTa_2O_5-PEG-FITC concentrations between 25 μg/mL (Figure 6.8 a) and 100 μg/mL (see Figure 6.8 c). A control picture of the cells without nanoparticles can be found in the appendix (Figure A.7). The images on the left show the cells, whose actin proteins are stained with Alexa Fluor® 555 Phalloidin in the cytosceleton. The fluorescence of the FITC labeled nanoparticles can be observed in the middle row in Figure 6.8.

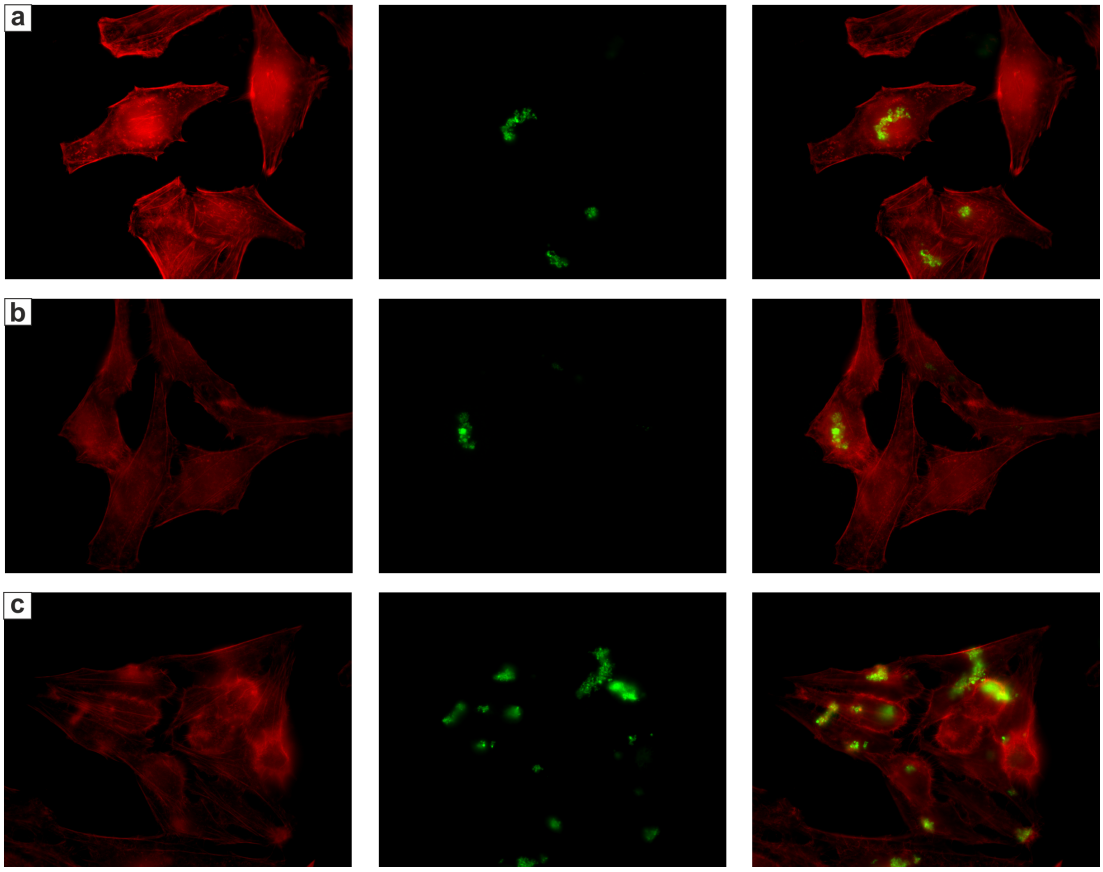

Figure 6.8.: Confocal laser scanning images of HeLa cells stained with Alexa Fluor® 555 Phalloidin incubated with a) 25 μg/mL, b) 50 μg/mL and c)100 μg/mL mTa_2O_5:Gd-PEG-FITC nanoparticles for 24 h. The pictures on the left show the cells, the ones in the middle the FITC labeled nanoparticles and the ones on the right show the merged pictures of the cells and nanoparticles.

Overlay images of the cells and the mTa_2O_5 nanoparticles are shown on the right. For all mTa_2O_5-PEG-FITC concentrations fluorescence of FITC can be detected. This confirms the dye functionalization of the mTa_2O_5-PEG-FITC. Furthermore the merged pictures demonstrate, that the NP and the cells are co-localized. It is unlikely, that the NP adhere to the cell surface as the cells were repeatedly washed prior to the measurement. Hence the nanoparticles are probably incorporated in the cells. This might make them suitable for drug delivery in cells.

6.4.3. Drug release

For drug delivery applications, the loading of the carriers as well as the release time have to be investigated. As a simple model system the mTa_2O_5 nanoparticles are loaded with Diclofenac by diffusion into the pores for at least 12 h. The subsequent release of diclofenac from the mTa_2O_5 was monitored with UV-VIS. The release profile as well as the structural formula of diclofenac are depicted in Figure 6.9. Here the adsorbance of

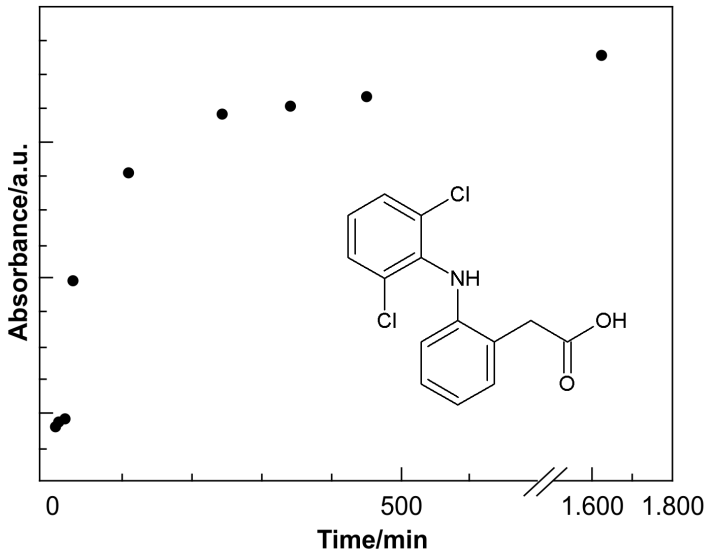

Figure 6.9.: Release profile of diclofenac (see inset) from mTa_2O_5-NH_2 nanoparticles in PBS buffer at ambient temperature.

diclofenac is plotted against the time. The diagram shows the typical release curve of non-functionalized mesoporous materials which is characterized by a sharp increase in the beginning (burst effect) followed by a slow release towards the end. [302] Essentially the diclofenac release reaches saturation after 6 h afterwards the absorbance increased

only insignificantly (up to 27 h). Further half of the Diclofenac diffuses out of the pores after about 90 min. This release time is to short for most applications, that require longer circulation times up too several hours before any significant release occurs.[303,304] Yet, such a fast release can be useful in the treatment of acute inflammations or infections where large dose are needed fast.[302] Likely the fast diffusion out of the mTa_2O_5 is caused by the large pores (3.7 nm) and no tailored functionalization to keep the diclofenac inside the mTa_2O_5 nanoparticles. There are different strategies that can be applied to retard the release like bonding of the pharmazeuticals to the particle surface or lipid bilayers around the particles as a whole.[305–307] Alternatively the release can be triggered by external stimuli such as pH change, enzymes or proteins, temperature, light, ultrasound oar an applied magnetic field[308,309] The large pores however might be suitable for the delivery of larger molecules like DNA or other macromolecules.

6.4.4. Application as multimodal contrast agent

In order to confirm the potential of the mTa_2O_5:Gd to act as multimodal contrast agents, the CT and MRI contrasts are investigated. Figure 6.10 a depicts the CT-contrast of mTa_2O_5:Gd-PEG-APTES in Hounsfield units (HU) in dependence on the Tanatalum concentration which was determined by ICP-MS measurements of the sample. As expected the CT-contrast increases linearly with the Tantalum concentration in the solution. At the highest concentration, the CT-contrast is 122 HU, which slightly lower than expected for a linear increase. This might be attributed to a decreased solubility of the nanoparticles at high concentrations. However, the rising CT-contrast confirms the activity of the mTa_2O_5:Gd-PEG-APTES as a CT-contrast agent. The CT values of the mTa_2O_5:Gd-PEG-APTES are too low for medical applications where CT-contrast agents should have contrasts around 200 HU. Therefore higher mTa_2O_5:Gd concentrations than the ones used for this measurement are needed. Albeit the solubility of the mTa_2O_5:Gd must be improved if higher concentrations are required as the mTa_2O_5:Gd-PEG-APTES precipitate faster at the highest measured concentrations.
Next to CT-contrast enhancement the mTa_2O_5:Gd-PEG-APTES should be MRI active due to the unpaired spins in Gd^{3+} which makes them suitable as T_1 contrast agents.[33,42] Therefore T_1 weighted MRI measurements were performed on the mTa_2O_5:Gd-PEG-APTES with 1% Gd. Figure 6.10 b shows the corresponding T_1 relaxivity plots. There $1/T_1=r_1$ is plotted against the Gadolinium concentration. The relaxivity r_1, defined as the relaxation enhancement normalized to the concentration, is given by the slope. The MRI contrast increases linearly with the Gadolinium concentration confirming

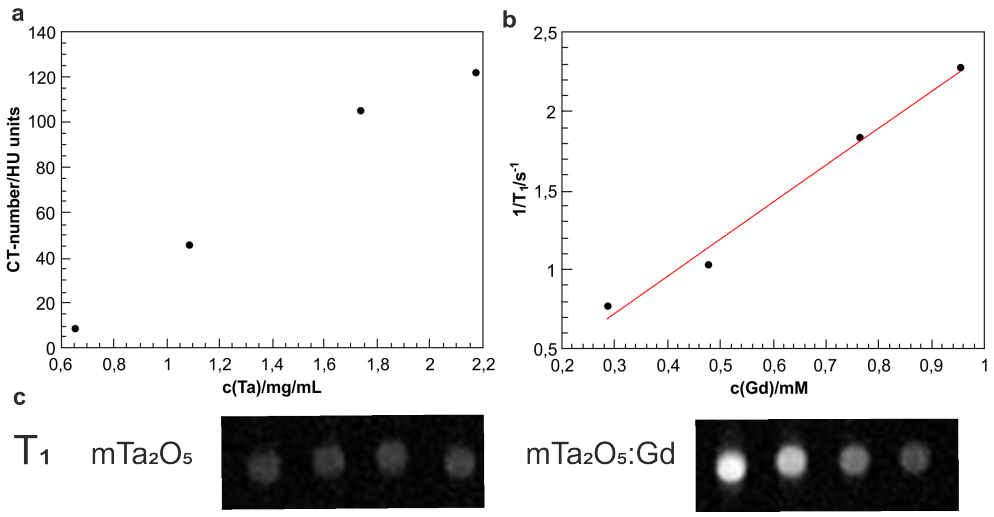

Figure 6.10.: a) CT contrast of mTa_2O_5:Gd-PEG-APTES in dependence on the Ta concentration b) T_1 measurement of the mTa_2O_5:Gd-PEG-APTES with the relaxivity r_1 in dependence on the Gadolinium concentration c) images of the T_1 contrast of mTa_2O_5-PEG-APTES (left) and mTa_2O_5:Gd-PEG-APTES (right) in dependence on the concentration.

the T_1 activity. The relaxivity, determined by linear regression, is r_1=2.34 mM/s for mTa_2O_5:Gd-PEG-APTES with 1% Gd which is in the typical order of magnitude for Gadolinium based nanoparticle contrast agents.[310,311] The T_1 contrast is corroborated by the T_1 images of mTa_2O_5-PEG-APTES and mTa_2O_5:Gd-PEG-APTES with different concentrations in Figure 6.10 c on the left and right respectively. For mTa_2O_5, all spots have the same shade, whereas the spots become lighter with increasing NP concentration for mTa_2O_5:Gd-PEG-APTES. A brightening in the T_1 image is typical for T_1 contrast agents as they have a positive contrast.[42] This confirms the Gadolinium inside the mTa_2O_5-PEG-APTES is responsible for the T_1 contrast, since the nanoparticles are T_1 inactive without Gadolinium.

Moreover the T_1 relaxivity of the mTa_2O_5:Gd-PEG-APTES was investigated for different Gadolinium amounts within the nanoparticles to determine the influence of the Gadolinium amount. The r_1 value is a measure for the quality of a T_1 contrast agent. In general, the r_1 values are a measure for the efficiency of a T_1 contrast agent; the higher the r_1 value the better the contrast agent[312] Table 6.2 summarizes the r_1 values of the mTa_2O_5:Gd with varying Gd concentration while the corresponding T_1 relaxivity

plots are shown in Figure A.8 in the appendix. The r_1 values for the mTa_2O_5:Gd-

Table 6.2.: Relaxivity r_1 of the mTa_2O_5:Gd nanoparticles with different Gd amounts.

Amount of Gd/%	$r_1/mM^{-1}s^{-1}$
0.02	21.4
0.10	14.4
0.24	10.2
0.81	1.63
1.54	3.61

PEG-APTES are between 1.63 and 21.4 mM/s for the nanoparticles with 1.54% and 0.02% Gd respectively which are in the typical order of magnitude for Gadolinium based contrast agents.[310] Generally the samples with a higher Gadolinium amount exhibit lower r_1 values whereas the ones with lower Gadolinium concentrations have higher r_1 values. The relaxivity enhancement for an individual Gd^{3+} arises from the interaction of the time fluctuation of the dipolar coupling between the electron magnetic moment of the metal ion and that of the water protons either *via* an inner or outer sphere mechanism.[286,313] For this interactions to happen the metal ions and water molecules have to be in close proximity. Therefore the Gd^{3+} have to be at or close to the surface of the mTa_2O_5:Gd-PEG-APTES to be able to interact with the water protons. This might also explain the different relaxivities of the mTa_2O_5:Gd with different Gd amounts. The Gd^{3+} that embedded deep inside the mTa_2O_5:Gd-PEG-TES might be silent from an relaxometric point of view because they are not exposed to the solvent and thus cannot interact. This is supported by the findings of Johnson et al.,[310] that demonstrated the relaxivity per Gd^{3+} increases with the fraction of surface atoms for $NaGdF_4$ nanoparticles. Apparently for the mTa_2O_5:Gd with low Gadolinium concentrations the molar fraction of Gadolinium close to the surface is higher making them the better T_1 contrast agents.
Additionally, the mTa_2O_5:Gd-PEG-FITC can also be used for optical imaging. Owing to the FITC attached to the nanoparticles, the mTa_2O_5:Gd-PEG-FITC fluoresce as demonstrated in Figure 6.8. Optical imaging complements CT and MRI as it has a higher resolution up to the cellular level and sensitivity that cannot be attained by CT and MRI.[264] Therefore the combination of the nanoparticles with dyes allows for an increase in information. Hence mTa_2O_5:Gd-PEG-FITC nanoparticles can be applied as multimodal contrast agents for optical imaging, CT and MRI.

6.5. Conclusion

In summary, spherical Gadolinium doped mesoporous tantalum oxide nanoparticles were synthesized with varying Gadolinium amount between 0 and 1.5%. The shape, surface area and mesoporous structure of the mTa_2O_5 is independent of the Gadolinium amount up to 1%. For higher Gadolinium concentrations (1.5%) the spherical shape gets distorted although the mesoporous structure remains. The actual Gadolinium:Tantalum ratio was determined using ICP-MS. For further applications, the mTa_2O_5 were functionalized with PEG for biocompability and amine groups to induce further active moieties e.g. dyes such as FITC. IR, UV-VIS and ζ-potential measurements corroborate the successful functionalization of the mTa_2O_5:Gd nanoparticles . Whereas the biocompability was confirmed with cell tests that show no toxic effect for all investigated nanoparticles. Additionally the low toxicity indicates Gadolinium is embedded in the mTa_2O_5. Drug release test showed a fast diffusion driven release of Diclofenac within hours. Moreover, the mTa_2O_5:Gd were tested as multimodal contrast agents. Fluorescence images of the mTa_2O_5-PEG-FITC prove their applicability for fluorescence imaging as well as cell uptake as the pictures were taken in cells. CT and T_1-MRI images were taken at the same time and confirmed mTa_2O_5:Gd-PEG-APTES can act as CT and MRI contrast agents simultaneously. Further the relaxiviy of mTa_2O_5:Gd is related to the Gadolinium amount. Here, the samples with lower Gadolinium amounts show a higher relaxivity, up to 21.4 mM/s, making them the most promising candidates for CT/MRI dual imaging.

7 Conclusion and Outlook

This dissertation introduced several new synthesis procedures for various non-porous and mesoporous metal oxide nanoparticles. It demonstrated how the composition and morphology of nanoparticles can be tuned by varying the reaction parameters influencing the nucleation and growth kinetics. Moreover, different applications for metal oxide nanoparticles were explored in the field of catalysis and nanomedicine.

A new hydro-/solvothermal synthesis route for vanadium(IV) oxides was established. It allowed the formation of VO_2 nanoparticles with various distinct shapes such as rods, sheets and urchins. This morphology control was achieved by a systematic variation of the solvent ratios using water and ethanol in a binary mixed solvent. It was found that high water concentrations favor rod-shaped nanoparticles whereas sheets are formed at higher ethanol amounts.Urchin-shaped Vanadium oxide nanoparticles are obtained applying pure ethanol as solvent. The urchin-like shape evolves from the sheet-like particles that congregate in ethanol due to a lack of surface stabilization. Further, the reaction conditions for the urchin-formation were closer examined in terms of reaction temperature and Pluronic F127 concentration. Additionally, the impact of the nature of the alcohol on the morphology of the particles was determined. Therefore the alcohols with different chain lengths as well as bulky alcohols were applied as solvent. The steric hinderance of the longer chained alcohols prohibits the assembly into urchin-shaped nanoparticles and instead nanosheets emerge. These particles were characterized using TEM, IR, Raman, XRD and XPS.

Moreover, the vanadium oxide nanoparticles were tested for their catalytic activity as vanadium is known to be present in the active center of various enzymes. Among those enzymes are peroxidases which is why their peroxidase activity was evaluated using ABTS as a model substrate. The peroxidase activity of the rod, sheet and urchin-shaped

nanoparticles was investigated and compared to bulk V_2O_5 which has a confirmed peroxidase activity.[113] For all investigated nanoparticles the catalytic activity was better than that of bulk V_2O_5. The nano-urchins have the highest peroxidase activity closely followed by the nanosheets whereas the activity of the rods is considerably lower. The high catalytic activity of the urchins can be attributed to their high surface area which is one of key factors that govern the catalytic performance of nanoparticles. In order to ascertain this correlation the surface area of the vanadium oxide nanorods, sheets and urchins was determined using surface measuring methods (BET). The impact of the surface area was confirmed as it is the highest for the urchins ($124.6\,m^2/g$) followed by the nanosheets ($73.9\,m^2/g$) and lowest for the rods ($21.7\,m^2/g$) being in correlation to their catalytic proneness. Then the catalytic activity was directly related to the surface area by normalizing the catalytic activity to the BET surface area. Thereby the normalized peroxidase activity of the rods was distinctly higher than that of the nano-urchins and sheets, respectively. This finding demonstrates the strong influence of the surface area whereas the difference between the normalized activities stems form the different structures of the rods and urchins and sheets on the other side.

Future work comprises further investigations of the catalytic properties of the vanadium oxide nanoparticles. For one, he catalytic tests for the peroxidase activity will be expanded to the kinetic parameters of Michaelis-Menten type reactions. These tests determine the enzyme mimetic properties of the vanadium oxide nanoparticles in regard to their peroxidase activity. As vanadium is also present in the active center of other enzymes it is prudent to test the catalytic activity of the vanadium oxide nanoparticles for other reactions.

In addition, new hydrothermal synthesis protocols were designed to obtain nanosized Ta_2O_5 rods and $MTaO_3$ cubes (M=Na, K, Rb,H). Therefore we investigated the pH dependence in the synthesis of tantalum oxide and tantalate nanoparticles as the pH value and ion concentration often has a pronounced effect on the morphology and composition of nanoparticles. In acidic reaction media, particle agglomerates predominate whereas non-agglomerated tantalum oxide rods are obtained at nearly neutral pH values. With increasing pH values rods change into cube shaped nanoparticles. This shape transformation is accompanied by a change in composition from tantalum oxide to tantalate nanoparticles. Additionally, the impact of the base cation was determined. While there is no apparent influence of the base cation on the morphology, different $MTaO_3$ (M=Na, K, Rb) are obtained at high base concentrations. All tantalates have a pyrochlore structure, which is characterized by tunnels that host the alkali metal ions. The alkali metal cations can be easily replaced with other ions like H^+ while still

retaining their morphology. We exploited the ion exchange to obtain cube shaped $HTaO_3$ nanoparticles that can be transformed into cube shaped Ta_2O_5 nanoparticles upon heat treatment. Furthermore, these nanoparticles, especially the $HTaO_3$ nanoparticles, show promising catalytic properties which were tested in the degradation of Rhodamine B.
Furthermore, spherical mesoporous tantalum oxide nanoparticles were synthesized that are characterized by their high surface areas above $160\,m^2/g$ and a narrow pore size distribution. The reaction parameters of the nanoparticle formation were investigated, these include employed acids and bases, reaction temperature and amount of templating agent. Thereby it was found out that the mTa_2O_5 nanoparticles are formed *via* a self-assembly process of small tantalum oxide nanoparticles instead of a template controlled mechanism, and no template is required. This assumption was further corroborated upon heat treatment. There the pore sizes increased upon annealing as the particles start to coalescence which is typical of mesoporous materials that are made up of particle aggregates. In contrast, the pore sizes of mesoporous materials formed *via* a templating mechanism shrink when they are annealed. Besides, the surface area decreases and the nanoparticles start to crystallize when they are heat treated. Moreover, the mesoporous nanoparticles were decorated with noble metal nanoparticles. However, the mTa_2O_5 are amorphous. Therefore the attachment of noble metal particles was mediated via amino groups which were grafted onto the tantalum oxide surface with using APTES as ligand. The amine functionalization was confirmed using FT-IR and ζ-potential measurements. Subsequently, palladium nanoparticles were uniformely deposited onto mTa_2O_5 nanoparticles *via* a sonochemical reaction. Both, the high surface are as well as the mesoporous structure of the mTa_2O_5, was retained. This makes them promising candidates for further catalytic applications.
Future work will include an investigation of the catalytic activity of the $Pd@mTa_2O_5$ for several reactions like hydrogen evolution or hydrogenation reactions. Additionally the effect of the support on the catalytic activity of the Pd nanoparticles is to be investigated. Palladium in different shapes, sizes and amounts will be attached onto the mTa_2O_5 as these properties factor often favor the catalytic activities due to a synergistic effect of electron transfer. Furthermore, the attachment of nanoparticles can be expanded to other noble metal nanoparticles like gold that have a similar Pearson hardness and also interact well with amines. Various noble metal nanoparticles on the mesoporous tantalum oxide allow to widen the scope of catalytic reactions as well as compare to the performance.
Moreover, mesoporous tantalum oxide nanoparticles can be used for biomedical applications. Also Gadolinium doped mesoporous tantalum oxide nanoparticles were

synthesized that can not only act as a CT contrast agents but also for MRI imaging due to the unpaired spins of the Gd^{3+} ions. For this purpose the synthesis of mTa_2O_5 was adapted to obtain mTa_2O_5:Gd nanoparticles with varying amount of Gadolinium which was determined using ICP-MS. The Gadolinium doping did neither affect the morphology nor the shape of the mTa_2O_5 nanoparticles for low Gadolinium concentrations whereas the spherical shape is obscured at higher Gadolinium concentrations. For biological applications the solubility and biocompability of nanoparticles is crucial. Therefore the nanoparticles were functionalized with APTES and PEG-TES, a PEG silane. Further the biocompability was corroborated by cytotoxicity-assays as now toxic effects are observed for all Gadolinium concentrations. Additionally, dye molecules were attached to the nanoparticles over the amine groups of the APTES. The dye functionalization was observed in cell fluorescence images that also confirmed that the nanoparticles are readily taken up into cells. This observation indicates the dye functionalized nanoparticles are suitable for fluorescence imaging. The drug release of mTa_2O_5 nanoparticles was also studied using diclofenac as a model substrate. What is more the mTa_2O_5:Gd-PEG-APTES were also tested as simultaneous CT and MRI contrast agent. The mTa_2O_5:Gd-PEG-APTES exhibit a CT and T_1 contrast enhancement at the same time that makes them suitable for CT/MRI dual imaging. Additionally, the T_1 relaxitivity was related to the Gadolinium amount in the nanoparticles. Thereby samples with lower Gadolinium amounts have a higher T_1 contrast per Gadolinium ion up to 21.4 mM/s.

Future work also compromises the functionalization of the mTa_2O_5:Gd with more sophisticated polymers that allow an improved solubility in physiological media and enable cell targeting. Then, the nanoparticle may be tested *in vivo*. Additionally, mesoporous nanoparticles can be used as carriers for targeted drug delivery. As the pores in the mTa_2O_5:Gd are relatively large with an average of 3.7 nm they release small molecules fast. Therefore the mTa_2O_5 will either be loaded with larger molecules or the the release can be slowed down by encapsulating the nanoparticles in lipid bilayers. These nanoparticle plattforms can be used for targeted delivery *in vivo*.

A Appendix

A.1. Supporting Information

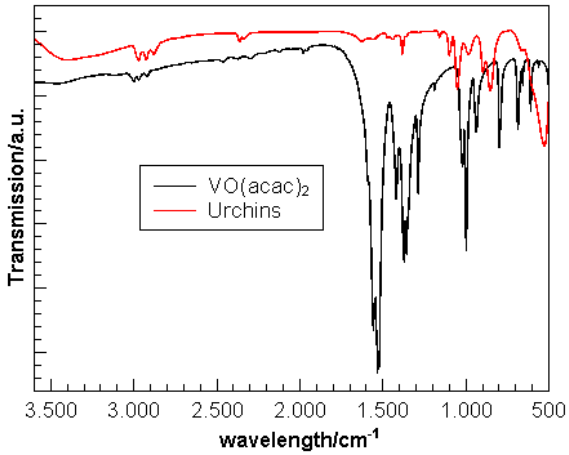

Figure A.1.: IR spectra of the $VO(acac)_2$ (black) precursor used in the synthesise of the VO_x nanourchins (red).

Table A.1.: Measurement and refinement parameters of the X-ray diffraction patterns of the products prepared at different pH-values.

	pH=3	pH=4	pH=9	pH=12	pH=13
Diffractometer	Siemens D5000				
Sample preparation	Fine powder fixed between two stripes of Scotch tape				
Measuring mode	Transmission				
Wavelength	1.540596				
Measuring range	$10 \leq 2\Theta/^\circ \geq 90$, $0.71 \leq Q/Å^{-1} \geq 5.77$				
Temperature/K	298K				
Profile Fit	Rietveld refinement with reported crystal structure models				
Background	Chebyshev				
Profile function	Fundamental Parameters Approach				
Program	TOPAS Academic V5				
Total no. Parameters /Background	29/20	29/20	33/20	27/20	33/20
R_{exp}	1.97	3.47	2.06	1.96	1.94
R_{wp}	4.21	6.55	6.72	5.17	4.97
GoF	2.92	1.89	3.26	2.64	2.52
DW	0.36	0.69	0.25	0.30	0.52
Ta_2O_5-*oP*14					
Spacegroup		*Pccm*			
Cell parameters/Å	a=3.6188(5) b=6.304(2) c=7.7910(1)	a=3.6264(5) b=6.318(2) c=7.8097(9)	a=3.5810(1) b=6.14(4) c=7.775(2)		
Crystallite size/nm	41(1)(ab) 70(1)(c)	47(1)(ab) 75(1)(c)	48(2)(ab)		
Fraction/%wt	100	100	15(2)		
Biso	3.3(1)	3.4(1)	3.0(fix)		
Preferred Orientation	1.33(1) /(020)	1.38(1) /(020)	3.3(2) /(020)		
$H_2Ta_2O_6 \cdot H_2O$-*cF*104					
Spacegroup				*Fd-3m*	
Cell parameter/Å			a=10.457(2)	a=10.5249(3)	a=10.5237(5)
Crystallite siz/nm			33(1)	47(1)	21(1)
Fraction/%wt			85(1)	100	83(1)
Biso			3(fix)	3(fix)	3(fix)
site occupation factor 16*d*			1.00(6)	0.42(1)	0.39(2)
site occupation factor 8b			1.0(1)	0.37(3)	0.28(4)
approx. composition			$Na_2Ta_2O_6 \cdot H_2O$	$Na_{0.84}H_{1.16}Ta_2O_6 \cdot 0.37H_2O$	$Na_{0.78}H_{1.22}Ta_2O_6 \cdot 0.28H_2O$
$NaTaO_3$-*oP*10					
Spacegroup					*Pnma*
Cell parameter/Å					a=5.5258(3) b=7.7971(4) c=5.4839(3)
Crystallite size/nm					>100 nm
Fraction /%wt					17(2)
Biso					3.0(fix)

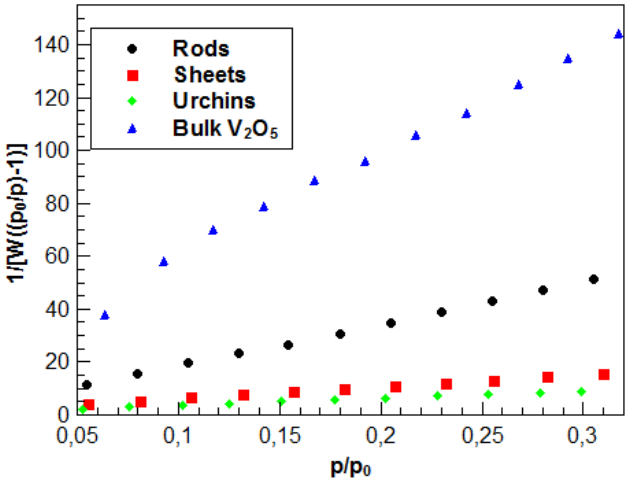

Figure A.2.: Multipoint BET of the VO_2 rods and VO_x urchins and sheets.

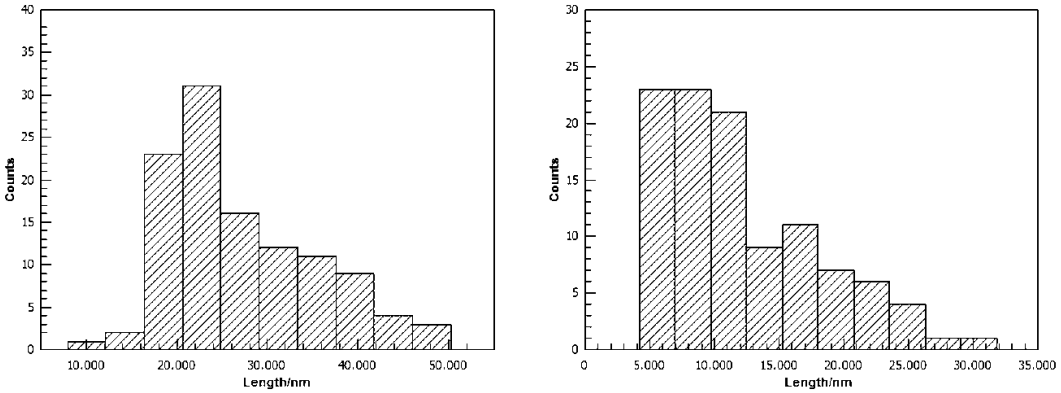

Figure A.3.: Histograms of the $NaTaO_3$ nanorods synthesized at pH=12 (left) and pH=13 (right)

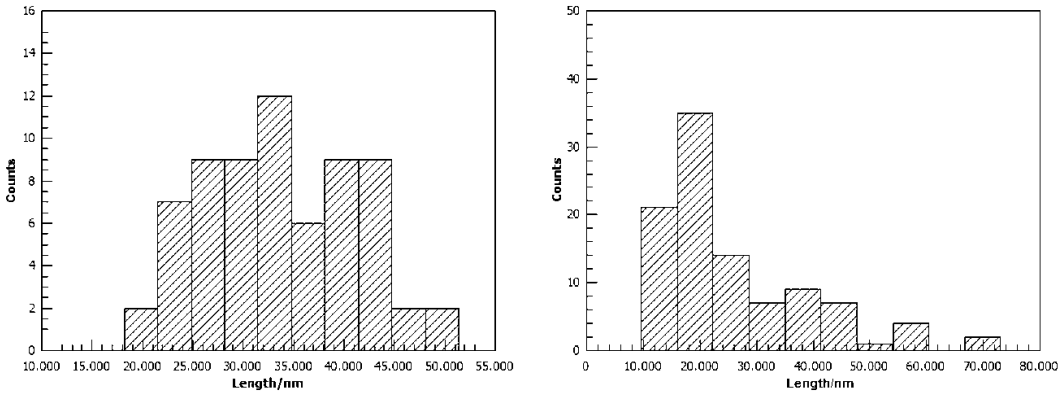

Figure A.4.: Histograms of the $KTaO_3$ (left) and $RbTaO_3$ nanoparticles synthesized at pH=12.

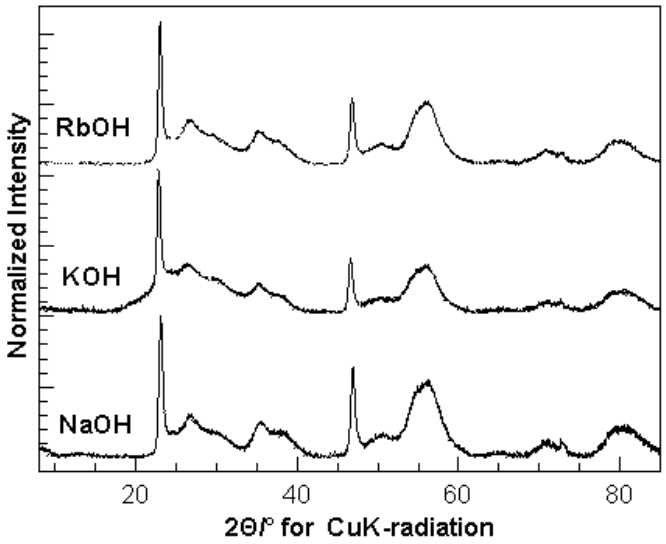

Figure A.5.: X-ray diffraction patterns of the Tantalum oxide rods with 5 mM NaOH, KOH, RbOH (from bottom to top) respectively.

Table A.2.: Measurement and refinement parameters of the X-ray diffraction patterns of the cube-shaped nanoparticles with different bases

	Na	K	Rb
Diffractometer	Siemens D5000		
Sample preparation	Fine powder fixed between two stripes of Scotch tape		
Measuring mode	Transmission		
Wavelength	1.540596		
Measuring range	$10 \leq 2\Theta/^\circ \geq 90$, $0.71 \leq Q/Å^{-1} \geq 5.77$		
Temperature/K	298K		
Profile Fit	Rietveld refinement with reported crystal structure models		
Background	Chebyshev		
Profile function	Fundamental Parameters Approach		
Total No. Parameters /Background	27/20		
R_{exp}	1.96	1.97	3.59
R_{wp}	5.17	5.57	3.59
GoF	2.64	2.83	2.06
Ta_2O_5-*oP*14			
Spacegroup	*Fd-3m*		
Cell parameter/Å	10.5249(3)	10.6324(2)	10.6146(7)
Crystallite size/nm	47(1)	68(1)	31(1)
Fraction/%wt	100	100	100
Biso	3(fix)		
Site occupation factor 16*d*	0.42(1)	0.488(8)	0.098(5)
Site occupation factor 8b	0.37(3)	0.00(3)	1.00(5)
Approx. composition	$Na_{0.88}H_{1.12}Ta_2O_6 \cdot 0.37H_2O$	$K_{0.97}H_{1.03}Ta_2O_6 \cdot 1H_2O$	$Rb_{0.2}H_{1.8}Ta_2O_6$

Table A.3.: XRF data of the cube-shaped $MTaO_3$ (M=Na, K, Rb) before and after treatment with 2 M HCl for 30 min.

Compound	Analyte	Calibration Status /kcps	Measured /kcps	Used /%	Conc.	Status
$NaTaO_3$	Na	Calibrated	6.102	5.587	12.551	calc.
	Ta	Calibrated	77.874	78.487	87.449	calc
HCl washed $NaTaO_3$	Al	Calibrated	0.101	0.097	0.187	calc.
	Ta	Calibrated	46.512	46.769	99.813	calc.
$KTaO_3$	Al	Calibrated	0.137	0.124	0.102	calc.
	Si	Calibrated	0.569	0.460	0.481	calc.
	K	Calibrated	7.553	7.554	9.019	calc
	Ta	Calibrated	100.934	101.813	90.398	calc.
HCl washed $KTaO_3$	Si	Calibrated	0.614	0.490	0.540	calc.
	S	Calibrated	0.346	0.232	0.101	calc.
	K	Calibrated	0.483	0.434	0.551	calc.
	Ta	Calibrated	104.688	101.813	90.398	calc.
$RbTaO_3$	Rb	Calibrated	151.266	151.206	27.107	calc.
	Ta	Calibrated	84.145	84.646	72.893	calc.
HCl washed $RbTaO_3$	Ta	Calibrated	84.973	85.650	100.000	calc.

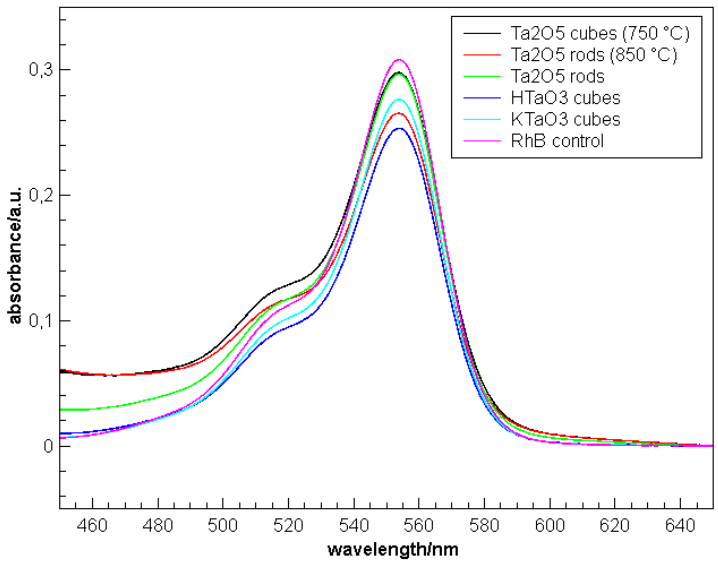

Figure A.6.: UV-VIS spectra of the samples with RhB after stirring in the dark for 18 min and centrifugation of the nanoparticles

Table A.4.: Measurement and refinement parameters of the X-ray diffraction pattern of the acid treated (2 M HCl) cube-shape nanoparticles and the heat treated rods and cube-shaped nanoparticles.

	Pristine	HCl treated	1023 K	1123 K
Diffractometer	Siemens D5000			
Sample preparation	Fine powder fixed between two stripes of Scotch tape			
Measuring mode	Transmission			
Wavelength	1.540596			
Measuring range	$10 \leq 2\Theta/^\circ \geq 90$, $0.71 \leq Q/Å^{-1} \geq 5.77$			
Temperature/K	298K			
Profile Fit	Rietveld refinement with reported crystal structure models			
Background	Chebyshev			
Profile function	Fundamental Parameters Approach			
Total No. Parameters Background	27/20	27/20	25/20	25/20
R_{exp}	1.97	1.98	2.03	2.12
R_{wp}	5.57	5.37	5.75	10.78
GoF	2.83	2.72	2.83	5.09
DW	0.30	0.31	0.33	0.16
$H_2Ta_2O_6 \cdot H_2O$-*cF*104				
Spacegroup	*Fd-3m*			
Cell parameter/Å	10.6324(2)	10.6014(2)		
Crystallite size/nm	68(1)	71(1)		
Fraction/wt%	100	100		
Biso	3(fixed)			
site occupation factor 16*d*	0.488(8)	0.000(7)		
site occupation factor 8b	0.00(3)	0.45(3)		
approx. composition	$K_{0.97}H_{1.03}Ta_2O_6$	$H_2Ta_2O_6 \cdot 0.45H_2O$		
Ta_2O_5-*oP*14				
Spacegroup			*Pccm*	
Cell parameters/Å			a=3.6380(3) b=6.2670(6) c=7.7824(5)	a=3.6565(4) b=6.2108(8) c=7.7758(8)
Crystallite size/nm			33(1)(ab) 49(1)(c)	20(1)(ab) 57(1)(c)
Fraction/wt%			100	100
Biso			3.09(6)	3.64(9)
Preferred Orientation			1.052(5) /(020)	1.086(6) /(020)

Table A.5.: Measurement and refinement parameters of the X-ray diffraction patterns of heat treated mTa_2O_5 for 6 h at 923 K

	mTa_2O_5 (6 h at 923 K)
Diffractometer	Siemens D5000, Cu-anode, Ge(111) monochromator
Sample preparation	Fine powder between two Scotch® stripes
Measuring mode	Transmission
Wavelength/Å	1.540596
Measuring range	10≤2Θ/° ≥95, 0.64≤QÅ≥5.54
Refinement range	10≤2Θ/° ≥95, 0.64≤QÅ≥5.54
Temperature/K	298
Profile Fit	Rietveld refinement with reported crystal structure models
Background	Chebyshev
Profile function	Fundamental Parameters Approach
Program	TOPAS Academic V5
Total No. Parameters /Background	23/16
R_{wp}	7.27
GoF	2.94
DW	0.23
Ta_2O_5-*oP*14	
Spacegroup	*Pccm*
Cell parameter/Å	a=3.656(1) b=6.229(2) c=7.780(2)
Crystallite size max/nm	23(1)
Crystallite size expected/nm	1.39(1)
Biso	2.3(1)
Preferred Orientation	-/-

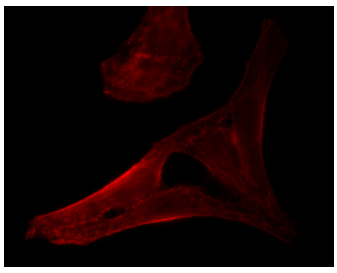

Figure A.7.: Confocal laser scanning microscope image of HeLa cells stained with Alexa Fluor® 555 Phalloidin without nanoparticles.

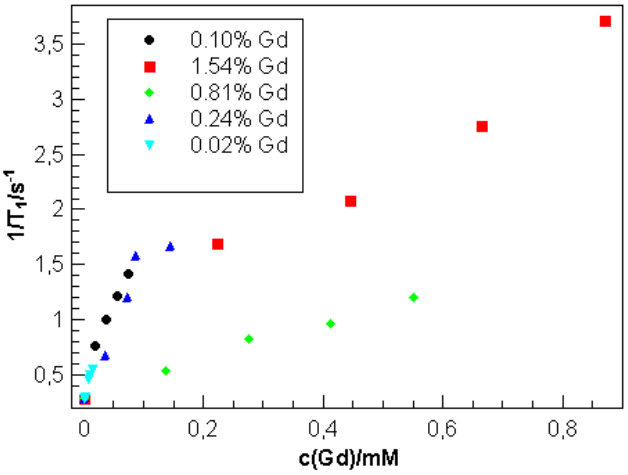

Figure A.8.: T_1 relaxivity plots for mTa_2O_5:Gd nanoparticles with different Gd concentrations.

A.2. List of publications

1. **D. Gömpel**, M. N. Tahir, M. Panthöfer, E. Mugnaioli, R. Brandscheid, U. Kolb and W. Tremel, "Facile hydrothermal synthesis of crystalline Ta_2O_5 nanorods, $MTaO_3$ (M = H, Na, K, Rb) nanoparticles and their photocatalytic behaviour" *J. Mater. Chem. A*, **2014**, 2, 8033-8040

2. **D. Gömpel**, M. N. Tahir, R. Ragg, K. Herget and W. Tremel "Synthesis of Vanadium oxide rods, sheets and sea-urchin like particles and their catalytic behaviour" *in preparation*

3. **D. Gömpel**, M. N. Tahir, M. Klünker, M. Panthöfer and W. Tremel "Synthesis of mesopourous Tantalum oxide nanoparticles" *in preparation*

Bibliography

[1] Tetley, T. D. Health effects of nanomaterials. *Biochem. Soc. Trans.* **2007**, *35*, 527–531.

[2] Parlett, C. M. a.; Wilson, K.; Lee, A. F. Hierarchical porous materials: catalytic applications. *Chem. Soc. Rev.* **2013**, *42*, 3876–93.

[3] Astruc, D. Palladium nanoparticles as efficient green homogeneous and heterogeneous carbon-carbon coupling precatalysts: a unifying view. *Inorg. Chem.* **2007**, *46*, 1884–94.

[4] Hötzer, B.; Medintz, I. L.; Hildebrandt, N. Fluorescence in nanobiotechnology: sophisticated fluorophores for novel applications. *Small* **2012**, *8*, 2297–326.

[5] Baron, R.; Willner, B.; Willner, I. Biomolecule-nanoparticle hybrids as functional units for nanobiotechnology. *Chem. Commun. (Camb).* **2007**, 323–32.

[6] Goesmann, H.; Feldmann, C. Nanoparticulate functional materials. *Angew. Chem. Int. Ed. Engl.* **2010**, *49*, 1362–95.

[7] Ling, D.; Hyeon, T. Chemical design of biocompatible iron oxide nanoparticles for medical applications. *Small* **2013**, *9*, 1450–66.

[8] Kelkar, S. S.; Reineke, T. M. Theranostics: combining imaging and therapy. *Bioconjug. Chem.* **2011**, *22*, 1879–903.

[9] Armand, M.; Tarascon, J.-M. Building better batteries. *Nature* **2008**, *451*, 652–7.

[10] Reddy, M. V.; Subba Rao, G. V.; Chowdari, B. V. R. Metal oxides and oxysalts as anode materials for Li ion batteries. *Chem. Rev.* **2013**, *113*, 5364–457.

[11] Roduner, E. Size matters: why nanomaterials are different. *Chem. Soc. Rev.* **2006**, *35*, 583–592.

[12] De, S.; Dutta, S.; Patra, A. K.; Bhaumik, A.; Saha, B. Self-assembly of mesoporous TiO2 nanospheres via aspartic acid templating pathway and its catalytic application for 5-hydroxymethyl-furfural synthesis. *J. Mater. Chem.* **2011**, *21*, 17505–17510.

[13] Jun, Y.-w.; Choi, J.-s.; Cheon, J. Shape control of semiconductor and metal oxide nanocrystals through nonhydrolytic colloidal routes. *Angew. Chem. Int. Ed. Engl.* **2006**, *45*, 3414–39.

[14] Schladt, T. D. Design of Multifunctional Magnetic Nanomaterials for Biomedical Applications. Ph.D. thesis, Johannes Gutenberg-Universität, Mainz, 2010.

[15] Nguyen, T.-D. From formation mechanisms to synthetic methods toward shape-controlled oxide nanoparticles. *Nanoscale* **2013**, *5*, 9455–82.

[16] Bodnarchuk, M. I.; Kovalenko, M. V.; Groiss, H.; Resel, R.; Reissner, M.; Hesser, G.; Lechner, R. T.; Steiner, W.; Schäffler, F.; Heiss, W. Exchange-coupled bimagnetic wüstite/metal ferrite core/shell nanocrystals: size, shape, and compositional control. *Small* **2009**, *5*, 2247–52.

[17] Cuenya, B. R. Synthesis and catalytic properties of metal nanoparticles: Size, shape, support, composition, and oxidation state effects. *Thin Solid Films* **2010**, *518*, 3127–3150.

[18] Polarz, S. Shape Matters: Anisotropy of the Morphology of Inorganic Colloidal Particles - Synthesis and Function. *Adv. Funct. Mater.* **2011**, *21*, 3214–3230.

[19] Xia, Y.; Xiong, Y.; Lim, B.; Skrabalak, S. E. Shape-controlled synthesis of metal nanocrystals: simple chemistry meets complex physics? *Angew. Chem. Int. Ed. Engl.* **2009**, *48*, 60–103.

[20] Nguyen, T.; Dinh, C.; Do, T. Shape-and size-controlled synthesis of monoclinic ErOOH and cubic Er2O3 from micro-to nanostructures and their upconversion luminescence. *ACS Nano* **2010**, *4*, 2263–2273.

[21] Zheng, X.; Kuang, Q.; Yan, K.; Qiu, Y.; Qiu, J.; Yang, S. Mesoporous TiO2 single crystals: facile shape-, size-, and phase-controlled growth and efficient photocatalytic performance. *ACS Appl. Mater. Interfaces* **2013**, *5*, 11249–57.

[22] International Union of Pure and Applied Chemistry, Recommendations for the characterization of porous solids. *Pure Appl. Chem.* **1994**, *66*, 1739–1758.

[23] Perego, C.; Millini, R. Porous materials in catalysis: challenges for mesoporous materials. *Chem. Soc. Rev.* **2013**, *42*, 3956–76.

[24] Ren, Y.; Ma, Z.; Bruce, P. G. Ordered mesoporous metal oxides: synthesis and applications. *Chem. Soc. Rev.* **2012**, *41*, 4909–27.

[25] Rao, Y.; Antonelli, D. M. Mesoporous transition metal oxides: characterization and applications in heterogeneous catalysis. *J. Mater. Chem.* **2009**, *19*, 1937–44.

[26] Gu, D.; Schüth, F. Synthesis of non-siliceous mesoporous oxides. *Chem. Soc. Rev.* **2014**, *43*, 313–44.

[27] Schüth, F. Non-siliceous Mesostructured and Mesoporous Materials. *Chem. Mater.* **2001**, *13*, 3184–3195.

[28] Narayanan, R.; El-Sayed, M. a. Catalysis with transition metal nanoparticles in colloidal solution: Nanoparticle shape dependence and stability. *J. Phys. Chem. B* **2005**, *109*, 12663–12676.

[29] Tao, A. R.; Habas, S.; Yang, P. Shape control of colloidal metal nanocrystals. *Small* **2008**, *4*, 310–325.

[30] Zhou, K.; Li, Y. Catalysis based on nanocrystals with well-defined facets. *Angew. Chemie - Int. Ed.* **2012**, *51*, 602–613.

[31] Li, Y.; Shen, W. Morphology-dependent nanocatalysts: Rod-shaped oxides. *Chem. Soc. Rev.* **2014**, *43*, 1543–1574.

[32] Lee, J. E.; Lee, N.; Kim, T.; Kim, J.; Hyeon, T. Multifunctional mesoporous silica nanocomposite nanoparticles for theranostic applications. *Acc. Chem. Res.* **2011**, *44*, 893–902.

[33] Lim, E.-k.; Kim, T.; Paik, S.; Haam, S.; Huh, Y.-m.; Lee, K. Nanomaterials for Theranostics: Recent Advances and Future Challenges. *Chem. Rev.* **2014**, *115*, 327–394.

[34] Janib, S. M.; Moses, A. S.; MacKay, J. A. Imaging and drug delivery using theranostic nanoparticles. *Adv. Drug Deliv. Rev.* **2010**, *62*, 1052–63.

[35] Whitesides, G. M. The ‘ right ’ size in nanobiotechnology. *Nat. Biotechnol.* **2003**, *21*, 1161–1165.

[36] Zhao, M.-X.; Huang, H.-F.; Xia, Q.; Ji, L.-N.; Mao, Z.-W. γ-Cyclodextrin–folate complex-functionalized quantum dots for tumor-targeting and site-specific labeling. *J. Mater. Chem.* **2011**, *21*, 10290–7.

[37] Reddy, S. T.; Swartz, M. a.; Hubbell, J. a. Targeting dendritic cells with biomaterials: developing the next generation of vaccines. *Trends Immunol.* **2006**, *27*, 573–9.

[38] Reddy, G. R.; Bhojani, M. S.; McConville, P.; Moody, J.; Moffat, B. a.; Hall, D. E.; Kim, G.; Koo, Y.-E. L.; Woolliscroft, M. J.; Sugai, J. V.; Johnson, T. D.; Philbert, M. a.; Kopelman, R.; Rehemtulla, A.; Ross, B. D. Vascular targeted nanoparticles for imaging and treatment of brain tumors. *Clin. Cancer Res.* **2006**, *12*, 6677–86.

[39] Xiao, Q.; Bu, W.; Ren, Q.; Zhang, S.; Xing, H.; Chen, F.; Li, M.; Zheng, X.; Hua, Y.; Zhou, L.; Peng, W.; Qu, H.; Wang, Z.; Zhao, K.; Shi, J. Radiopaque fluorescence-transparent TaOx decorated upconversion nanophosphors for in vivo CT/MR/UCL trimodal imaging. *Biomaterials* **2012**, *33*, 7530–9.

[40] Huang, W.-Y.; Davis, J. J. Multimodality and nanoparticles in medical imaging. *Dalton Trans.* **2011**, *40*, 6087–6103.

[41] Na, H. B.; Song, I. C.; Hyeon, T. Inorganic nanoparticles for MRI contrast agents. *Adv. Mater.* **2009**, *21*, 2133–2148.

[42] Na, H. B.; Hyeon, T. Nanostructured T1 MRI contrast agents. *J. Mater. Chem.* **2009**, *19*, 6267–6273.

[43] Lusic, H.; Grinstaff, M. W. X-ray-computed tomography contrast agents. *Chem. Rev.* **2013**, *113*, 1641–66.

[44] Liu, Y.; Ai, K.; Lu, L. Nanoparticulate X-ray computed tomography contrast agents: from design validation to in vivo applications. *Acc. Chem. Res.* **2012**, *45*, 1817–27.

[45] Goesmann, H.; Feldmann, C. Nanopartikuläre Funktionsmaterialien. *Angew. Chemie* **2010**, *122*, 1402–1437.

[46] Park, J.; Joo, J.; Kwon, S. G. S.; Jang, Y.; Hyeon, T. Synthesis of monodisperse spherical nanocrystals. *Angew. Chemie Int. Ed.* **2007**, *46*, 4630–60.

[47] Schladt, T. D.; Schneider, K.; Schild, H.; Tremel, W. Synthesis and bio-functionalization of magnetic nanoparticles for medical diagnosis and treatment. *Dalton Trans.* **2011**, *40*, 6315–43.

[48] Tretyakov, Y. D.; Goodilin, E. a. Key trends in basic and application-oriented research on nanomaterials. *Russ. Chem. Rev.* **2009**, *78*, 801–820.

[49] Thanh, N. T. K.; Maclean, N.; Mahiddine, S. Mechanisms of nucleation and growth of nanoparticles in solution. *Chem. Rev.* **2014**, *114*, 7610–30.

[50] Dinegar, R. H.; LaMer, V. K. Theory, Production and Mechanism of Formatio of Monodispersed Hydrosols. *J. Am. Chem. Soc.* **1950**, *72*, 4847–4854.

[51] Kwon, S. G.; Hyeon, T. Formation mechanisms of uniform nanocrystals via hot-injection and heat-up methods. *Small* **2011**, *7*, 2685–702.

[52] Rao, C. N. R.; Vivekchand, S. R. C.; Biswas, K.; Govindaraj, a. Synthesis of inorganic nanomaterials. *Dalton Trans.* **2007**, 3728–49.

[53] Ramadoss, A.; Krishnamoorthy, K.; Kim, S. J. Facile synthesis of hafnium oxide nanoparticles via precipitation method. *Mater. Lett.* **2012**, *75*, 215–217.

[54] Tang, J.; Fabbri, J.; Robinson, R. Solid-Solution Nanoparticles: Use of a Non-hydrolytic Sol-Gel Synthesis To Prepare HfO2 and Hf x Zr1-x O2 Nanocrystals. *Chem. Mater.* **2004**, 1336–1342.

[55] Sanchez-Dominguez, M.; Boutonnet, M.; Solans, C. A novel approach to metal and metal oxide nanoparticle synthesis: the oil-in-water microemulsion reaction method. *J. Nanoparticle Res.* **2009**, *11*, 1823–1829.

[56] Lopez-Quintela, M. Synthesis of nanomaterials in microemulsions: formation mechanisms and growth control. *Curr. Opin. Colloid Interface Sci.* **2003**, *8*, 137–144.

[57] Lu, A.-H.; Salabas, E. L.; Schüth, F. Magnetic nanoparticles: synthesis, protection, functionalization, and application. *Angew. Chem. Int. Ed. Engl.* **2007**, *46*, 1222–44.

[58] Ganguli, A. K.; Ganguly, A.; Vaidya, S. Microemulsion-based synthesis of nanocrystalline materials. *Chem. Soc. Rev.* **2010**, *39*, 474–85.

[59] Kuiry, S. C.; Patil, S. D.; Deshpande, S.; Seal, S. Spontaneous self-assembly of cerium oxide nanoparticles to nanorods through supraaggregate formation. *J. Phys. Chem. B* **2005**, *109*, 6936–6939.

[60] Eastoe, J.; Hollamby, M. J.; Hudson, L. Recent advances in nanoparticle synthesis with reversed micelles. *Adv. Colloid Interface Sci.* **2006**, *128-130*, 5–15.

[61] Oh, M. H.; Lee, N.; Kim, H.; Park, S. P.; Piao, Y.; Lee, J.; Jun, S. W.; Moon, W. K.; Choi, S. H.; Hyeon, T. Large-scale synthesis of bioinert tantalum oxide nanoparticles for X-ray computed tomography imaging and bimodal image-guided sentinel lymph node mapping. *J. Am. Chem. Soc.* **2011**, *133*, 5508–15.

[62] Wu, M.; Lin, G.; Chen, D.; Wang, G. Sol-hydrothermal synthesis and hydrothermally structural evolution of nanocrystal titanium dioxide. *Chem. Mater.* **2002**, *14*, 1974–1980.

[63] Hyeon, T.; Lee, S.; Park, J. Synthesis of highly crystalline and monodisperse maghemite nanocrystallites without a size-selection process. *J. Am. Chem. Soc.* **2001**, 12798–12801.

[64] Park, J.-G. J. J.-H.; An, K.; Hwang, Y.; Noh, H.-J.; Kim, J.-Y.; Hwang, N.-M.; Hyeon, T. Ultra-large-scale syntheses of monodisperse nanocrystals. *Nat. Mater.* **2004**, *3*, 891–5.

[65] Hatakeyama, M.; Kishi, H.; Kita, Y.; Imai, K.; Nishio, K.; Karasawa, S.; Masaike, Y.; Sakamoto, S.; Sandhu, A.; Tanimoto, A.; Gomi, T.; Kohda, E.; Abe, M.; Handa, H. A two-step ligand exchange reaction generates highly water-dispersed magnetic nanoparticles for biomedical applications. *J. Mater. Chem.* **2011**, *21*, 5959–5966.

[66] Schladt, T. D.; Graf, T.; Tremel, W. Synthesis and Characterization of Monodisperse Manganese Oxide NanoparticlesEvaluation of the Nucleation and Growth Mechanism. *Chem. Mater.* **2009**, *21*, 3183–3190.

[67] Sun, S.; Zeng, H.; Robinson, D. B.; Raoux, S.; Rice, P. M.; Wang, S. X.; Li, G. Monodisperse MFe2O4 (M = Fe, Co, Mn) nanoparticles. *J. Am. Chem. Soc.* **2004**, *126*, 273–9.

[68] Zhang, T.; Ge, J.; Hu, Y.; Yin, Y. A general approach for transferring hydrophobic nanocrystals into water. *Nano Lett.* **2007**, *7*, 3203–7.

[69] Cansell, F.; Chevalier, B.; Demourgues, A. Supercritical fluid processing: a new route for materials synthesis. *J. Mater. Chem.* **1999**, 67–75.

[70] Niederberger, M. Nonaqueous sol-gel routes to metal oxide nanoparticles. *Acc. Chem. Res.* **2007**, *40*, 793–800.

[71] Niederberger, M.; Bartl, M. H.; Stucky, G. D. Benzyl alcohol and transition metal chlorides as a versatile reaction system for the nonaqueous and low-temperature synthesis of crystalline nano-objects with controlled dimensionality. *J. Am. Chem. Soc.* **2002**, *124*, 13642–3.

[72] Pinna, N.; Karmaoui, M.; Willinger, M.-G. The "benzyl alcohol route": An elegant approach towards doped and multimetal oxide nanocrystals. *J. Sol-Gel Sci. Technol.* **2010**, *57*, 323–329.

[73] Pucci, A.; Clavel, G.; Willinger, M. G.; Zitoun, D.; Pinna, N. Transition metal-moped zrO2 and hfO2 nanocrystals. *J. Phys. Chem. C* **2009**, *113*, 12048–12058.

[74] Wu, Z.; Li, Q.; Feng, D.; Webley, P. A.; Zhao, D. Ordered mesoporous crystalline gamma-Al2O3 with variable architecture and porosity from a single hard template. *J. Am. Chem. Soc.* **2010**, *132*, 12042–50.

[75] Chen, D.; Cao, L.; Huang, F.; Imperia, P.; Cheng, Y.-B.; Caruso, R. a. Synthesis of monodisperse mesoporous titania beads with controllable diameter, high surface areas, and variable pore diameters (14-23 nm). *J. Am. Chem. Soc.* **2010**, *132*, 4438–44.

[76] Li, M.; Xue, J. Ordered mesoporous carbon nanoparticles with well-controlled morphologies from sphere to rod via a soft-template route. *J. Colloid Interface Sci.* **2012**, *377*, 169–75.

[77] Slowing, I. I.; Vivero-Escoto, J. L.; Trewyn, B. G.; Lin, V. S.-Y. Mesoporous silica nanoparticles: structural design and applications. *J. Mater. Chem.* **2010**, *20*, 7924–7937.

[78] Liu, H.; Du, X.; Xing, X.; Wang, G.; Qiao, S. Z. Highly ordered mesoporous Cr2O3 materials with enhanced performance for gas sensors and lithium ion batteries. *Chem. Commun. (Camb).* **2012**, *48*, 865–7.

[79] Lee, J.-H. Gas sensors using hierarchical and hollow oxide nanostructures: Overview. *Sensors Actuators B Chem.* **2009**, *140*, 319–336.

[80] Möller, K.; Bein, T. Mesoporosity–a new dimension for zeolites. *Chem. Soc. Rev.* **2013**, *42*, 3689–707.

[81] Cotí, K. K.; Belowich, M. E.; Liong, M.; Ambrogio, M. W.; Lau, Y. a.; Khatib, H. a.; Zink, J. I.; Khashab, N. M.; Stoddart, J. F. Mechanised nanoparticles for drug delivery. *Nanoscale* **2009**, *1*, 16–39.

[82] Kresge, C.; Leonowicz, M.; Roth, W. Ordered mesoporous molecular sieves synthesized by a liquid-crystal template mechanism. *Nature* **1992**, *359*, 710–712.

[83] Beck, J.; Vartuli, J.; Roth, W.; Leonowicz, M.; Kresge, C.; Schmitt, K. D.; Chu, C. T.-W.; Olson, D. H.; Sheppard, E. W.; McCullen, S. B.; Higgins, J. B.; Schlenker, J. L. A new family of mesoporous molecular sieves prepared with liquid crystal templates. *J. Am. Chem. Soc.* **1992**, *114*, 10834–10843.

[84] Schüth, F. Endo- und Exotemplate zur Erzeugung von anorganischen Materialien mit großer spezifischer Oberfläche. *Angew. Chemie* **2003**, *115*, 3730–3750.

[85] Antonelli, D.; Ying, J. Synthesis and characterization of hexagonally packed mesoporous tantalum oxide molecular sieves. *Chem. Mater.* **1996**, 874–881.

[86] Alexaki, N.; Stergiopoulos, T.; Kontos, A.; Tsoukleris, D.; Katsoulidis, A.; Pomonis, P.; LeClere, D.; Skeldon, P.; Thompson, G.; Falaras, P. Mesoporous titania nanocrystals prepared using hexadecylamine surfactant template: Crystallization progress monitoring, morphological characterization and application in dye-sensitized solar cells. *Microporous Mesoporous Mater.* **2009**, *124*, 52–58.

[87] Peng, T.; Zhao, D.; Dai, K.; Shi, W.; Hirao, K. Synthesis of titanium dioxide nanoparticles with mesoporous anatase wall and high photocatalytic activity. *J. Phys. Chem. B* **2005**, *109*, 4947–52.

[88] Deng, Y.; Wei, J.; Sun, Z.; Zhao, D. Large-pore ordered mesoporous materials templated from non-Pluronic amphiphilic block copolymers. *Chem. Soc. Rev.* **2013**, *42*, 4054–70.

[89] An, K.; Musselwhite, N.; Kennedy, G.; Pushkarev, V. V.; Baker, L. R.; Somorjai, G. a. Preparation of mesoporous oxides and their support effects on Pt nanoparticle catalysts in catalytic hydrogenation of furfural. *J. Colloid Interface Sci.* **2013**, *392*, 122–8.

[90] Ismail, A. a.; Bahnemann, D. W. Mesoporous titania photocatalysts: preparation, characterization and reaction mechanisms. *J. Mater. Chem.* **2011**, *21*, 11686–11707.

[91] Guo, L.; Ida, S.; Daio, T.; Hagiwara, H.; Ishihara, T. In situ carbonization of a soft-template to directly synthesize crystalline mesoporous metal oxides with high surface areas. *New J. Chem.* **2014**, *38*, 5846–5855.

[92] Li, W.; Zhao, D. An overview of the synthesis of ordered mesoporous materials. *Chem. Commun. (Camb).* **2013**, *49*, 943–6.

[93] Meynen, V.; Cool, P.; Vansant, E. Verified syntheses of mesoporous materials. *Microporous Mesoporous Mater.* **2009**, *125*, 170–223.

[94] Wan, Y.; Zhao, D. On the controllable soft-templating approach to mesoporous silicates. *Chem. Rev.* **2007**, *107*, 2821–60.

[95] Tsung, C.-K.; Fan, J.; Zheng, N.; Shi, Q.; Forman, A.; Wang, J.; Stucky, G. A General Route to Diverse Mesoporous Metal Oxide Submicrospheres with Highly Crystalline Frameworks. *Angew. Chemie* **2008**, *120*, 8810–8814.

[96] Brinker, C. J.; Lu, Y.; Sellinger, A.; Fan, H. Evaporation-Induced Self-Assembly: Nanostructures Made Easy. *Adv. Mater.* **1999**, *11*, 579–585.

[97] Luo, W.; Li, Y.; Dong, J.; Wei, J.; Xu, J.; Deng, Y.; Zhao, D. A resol-assisted co-assembly approach to crystalline mesoporous niobia spheres for electrochemical biosensing. *Angew. Chem. Int. Ed. Engl.* **2013**, *52*, 10505–10.

[98] Li, W.; Yue, Q.; Deng, Y.; Zhao, D. Ordered mesoporous materials based on interfacial assembly and engineering. *Adv. Mater.* **2013**, *25*, 5129–52.

[99] Antonelli, D.; Ying, J. Synthesis of hexagonally packed mesoporous TiO2 by a modified sol–gel method. *Angew. Chemie Int. Ed.* **1995**, *34*, 2014–2017.

[100] Nowak, I.; Jaroniec, M. “Hard” vs. “Soft” Templating Synthesis of Mesoporous Nb2O5 Catalysts for Oxidation Reactions. *Top. Catal.* **2008**, *49*, 193–203.

[101] Jiao, K.; Zhang, B.; Yue, B.; Ren, Y.; Liu, S.; Yan, S.; Dickinson, C.; Zhou, W.; He, H. Growth of porous single-crystal Cr2O3 in a 3-D mesopore system. *Chem. Commun. (Camb).* **2005**, 5618–20.

[102] Dong, A.; Ren, N.; Tang, Y.; Wang, Y. General synthesis of mesoporous spheres of metal oxides and phosphates. *J. Am. Chem. Soc.* **2003**, *125*, 4976–4977.

[103] Roggenbuck, J.; Koch, G.; Tiemann, M. Synthesis of Mesoporous Magnesium Oxide by CMK-3 Carbon Structure Replication. *Chem. Mater.* **2006**, *18*, 4151–4156.

[104] Lai, X.; Li, X.; Geng, W.; Tu, J.; Li, J.; Qiu, S. Ordered mesoporous copper oxide with crystalline walls. *Angew. Chem. Int. Ed. Engl.* **2007**, *46*, 738–41.

[105] Liu, Q.; Wang, A.; Wang, X.; Zhang, T. Ordered Crystalline Alumina Molecular Sieves Synthesized via a Nanocasting Route. *Chem. Mater.* **2006**, *18*, 5153–5155.

[106] Zhang, Z.; Gekhtman, D. Processing and characterization of single-crystalline ultrafine bismuth nanowires. *Chem. Mater.* **1999**, 1659–1665.

[107] Ugarte, D.; Chatelain, A.; Heer, W. D. Nanocapillarity and chemistry in carbon nanotubes. *Science (80-.).* **1996**, 13–15.

[108] Pham-Huu, C.; Keller, N.; Estournes, C.; Ehret, G.; Greneche, J. M.; Ledoux, M. J. Microstructural investigation and magnetic properties of CoFe2O4 nanowires synthesized inside carbon nanotubes. *Phys. Chem. Chem. Phys.* **2003**, *5*, 3716–3723.

[109] Yu, C.; Fan, J.; Tian, B.; Zhao, D.; Stucky, G. HighYield Synthesis of Periodic Mesoporous Silica Rods and Their Replication to Mesoporous Carbon Rods. *Adv. Mater.* **2002**, *14*, 1742–1745.

[110] Jiao, F.; Harrison, A.; Jumas, J.-C.; Chadwick, A. V.; Kockelmann, W.; Bruce, P. G. Ordered mesoporous Fe2O3 with crystalline walls. *J. Am. Chem. Soc.* **2006**, *128*, 5468–74.

[111] Lee, J.; Orilall, M. C.; Warren, S. C.; Kamperman, M.; DiSalvo, F. J.; Wiesner, U. Direct access to thermally stable and highly crystalline mesoporous transition-metal oxides with uniform pores. *Nat. Mater.* **2008**, *7*, 222–8.

[112] Soler-Illia, G. J. d. A. A.; Sanchez, C.; Lebeau, B.; Patarin, J. Chemical Strategies To Design Textured Materials: from Microporous and Mesoporous Oxides to Nanonetworks and Hierarchical Structures. *Chem. Rev.* **2002**, *102*, 4093–4138.

[113] André, R.; Natálio, F.; Humanes, M.; Leppin, J.; Heinze, K.; Wever, R.; Schröder, H. C.; Müller, W. E. G.; Tremel, W. V2O5 nanowires with an intrinsic peroxidase-like activity. *Adv. Funct. Mater.* **2011**, *21*, 501–509.

[114] Chen, X.; Wang, F.; Xu, J. Preparation of VO2(B) nanoflake with glycerol as reductant agent and its catalytic application in the aerobic oxidation of benzene to phenol. *Top. Catal.* **2011**, *54*, 1016–1023.

[115] Kim, T.; Wachs, I. E. CH3OH oxidation over well-defined supported V2O5/Al2O3 catalysts: Influence of vanadium oxide loading and surface vanadium-oxygen functionalities. *J. Catal.* **2008**, *255*, 197–205.

[116] Lamarque-Forget, S.; Pelletier, O.; Dozov, I.; Davidson, P.; Martinot-Lagarde, P.; Livage, J. Electrooptic effects in the nematic and isotropic phases of aqueous V2O5 suspensions. *Adv. Mater.* **2000**, *12*, 1267–1270.

[117] Li, W.; Ji, S.; Li, Y.; Huang, A.; Luo, H.; Jin, P. Synthesis of VO2 nanoparticles by a hydrothermal-assisted homogeneous precipitation approach for thermochromic applications. *RSC Adv.* **2014**, *4*, 13026–13033.

[118] Kim, H.; Hong, J.; Park, K.-Y.; Kim, H.; Kim, S.-W.; Kang, K. Aqueous Rechargeable Li and Na Ion Batteries. *Chem. Rev.* **2014**, *114*, 11788–11827.

[119] Tang, Y.; Rui, X.; Zhang, Y.; Lim, T. M.; Dong, Z.; Hng, H. H.; Chen, X.; Yan, Q.; Chen, Z. Vanadium pentoxide cathode materials for high-performance lithium-ion batteries enabled by a hierarchical nanoflower structure via an electrochemical process. *J. Mater. Chem. A* **2013**, *1*, 82–88.

[120] Yang, S.; Gong, Y.; Liu, Z.; Zhan, L.; Hashim, D. P.; Ma, L.; Vajtai, R.; Ajayan, P. M. Bottom-up approach toward single-crystalline VO2-graphene ribbons as cathodes for ultrafast lithium storage. *Nano Lett.* **2013**, *13*, 1596–601.

[121] Fu, H.; Jiang, X.; Yang, X.; Yu, A.; Su, D.; Wang, G. Glycothermal synthesis of assembled vanadium oxide nanostructures for gas sensing. *J. Nanoparticle Res.* **2012**, *14*, 871–885.

[122] Huang, Z.; Zeng, H.; Xue, L.; Zhou, X.; Zhao, Y.; Lai, Q. Synthesis of vanadium oxide, V6O13 hollow-flowers materials and their application in electrochemical supercapacitors. *J. Alloys Compd.* **2011**, *509*, 10080–10085.

[123] Hu, Y.-S.; Liu, X.; Müller, J.-O.; Schlögl, R.; Maier, J.; Su, D. Entwicklung von nanostrukturiertem V 2 O 5 mithilfe von Röhre-in-Röhre-Kohlenstoffstrukturen als Nanoreaktoren und Netzwerke mit effizienter Ionen- und Elektronenleitfähigkeit: Synthese und Elektrode. *Angew. Chemie* **2009**, *121*, 216–220.

[124] Wei, H.; Wang, E. Nanomaterials with enzyme-like characteristics (nanozymes): next-generation artificial enzymes. *Chem. Soc. Rev.* **2013**, *42*, 6060–6093.

[125] Lin, Y.; Ren, J.; Qu, X. Catalytically Active Nanomaterials : A Promising Candidate for Artificial Enzymes. *Acc. Chem. Res.* **2013**, *47*, 1097–1105.

[126] Andre, R. Bioinspired Composite Materials and Biomimetic Catalysis. Ph.D. thesis, Johannes Gutenberg-Universität, 2012.

[127] Gao, L.; Zhuang, J.; Nie, L.; Zhang, J.; Zhang, Y.; Gu, N.; Wang, T.; Feng, J.; Yang, D.; Perrett, S.; Yan, X. Intrinsic peroxidase-like activity of ferromagnetic nanoparticles. *Nat. Nanotechnol.* **2007**, *2*, 577–583.

[128] Lin, Y.; Li, Z.; Chen, Z.; Ren, J.; Qu, X. Mesoporous silica-encapsulated gold nanoparticles as artificial enzymes for self-activated cascade catalysis. *Biomaterials* **2013**, *34*, 2600–2610.

[129] Butler, a. Vanadium haloperoxidases. *Curr. Opin. Chem. Biol.* **1998**, *2*, 279–285.

[130] Rehder, D. Structure and function of vanadium compounds in living organisms. *Biometals* **1992**, *5*, 3–12.

[131] Rehder, D. Vanadium nitrogenase. *J. Inorg. Biochem.* **2000**, *80*, 133–136.

[132] Robson, R. L.; Eady, R. R.; Richardson, T. H.; Miller, R. W.; Hawkins, M.; Postgate, J. R. The alternative nitrogenase of Azotobacter chroococcum is a vanadium enzyme. *Nature* **1986**, *322*, 388–390.

[133] Wang, Y.; Zhang, Z.; Zhu, Y.; Li, Z.; Vajtai, R.; Ci, L.; Ajayan, P. M. Nanostructured VO Photocatalysts for Hydrogen Production. *ACS Na* **2008**, *2*, 1492–1496.

[134] An, K.; Somorjai, G. a. Nanocatalysis I : Synthesis of Metal and Bimetallic Nanoparticles and Porous Oxides and Their Catalytic Reaction Studies. *Catal. Letters* **2015**, 233–248.

[135] Han, S., Raja, R., Somorjai, G. A., Eds. *Nanotechnology in Catalysis*; Nanostructure Science and Technology; Springer New York: New York, NY, 2007; Vol. 3.

[136] Suib, S. L., Ed. *New and Future Developments in Catalysis - Catalysis by Nanoparticles*; Elsevier, 2013.

[137] Koper, M. T. M. Structure sensitivity and nanoscale effects in electrocatalysis. *Nanoscale* **2011**, *3*, 2054–2073.

[138] Nguyen, T.-D.; Do, T.-O. Solvo-hydrothermal approach for the shape-selective synthesis of vanadium oxide nanocrystals and their characterization. *Langmuir* **2009**, *25*, 5322–32.

[139] Pavasupree, S.; Suzuki, Y.; Kitiyanan, A.; Pivsa-Art, S.; Yoshikawa, S. Synthesis and characterization of vanadium oxides nanorods. *J. Solid State Chem.* **2005**, *178*, 2152–2158.

[140] Ji, S.; Zhao, Y.; Zhang, F.; Jin, P. Direct formation of single crystal VO2(R) nanorods by one-step hydrothermal treatment. *J. Cryst. Growth* **2010**, *312*, 282–286.

[141] Minić, D. M.; Blagojević, V. a. Hydrothermal synthesis and controlled growth of vanadium oxide nanocrystals. *CrystEngComm* **2013**, *15*, 6617–6624.

[142] Demazeau, G. Solvothermal reactions: An original route for the synthesis of novel materials. *J. Mater. Sci.* **2008**, *43*, 2104–2114.

[143] Zhu, Y.; Mei, T.; Wang, Y.; Qian, Y. Formation and morphology control of nanoparticles via solution routes in an autoclave. *J. Mater. Chem.* **2011**, *21*, 11457–11463.

[144] Xiong, S.; Xi, B.; Wang, C.; Zou, G.; Fei, L.; Wang, W.; Qian, Y. Shape-controlled synthesis of 3D and ID structures of CdS in a binary solution with L-cysteine's assistance. *Chem. - A Eur. J.* **2007**, *13*, 3076–3081.

[145] Wang, Y.-T.; Chen, C.-H. Facile growth of thermochromic VO2 nanostructures with greatly varied phases and morphologies. *Inorg. Chem.* **2013**, *52*, 2550–5.

[146] Kam, K. C.; Cheetham, A. K. Thermochromic VO2 nanorods and other vanadium oxides nanostructures. *Mater. Res. Bull.* **2006**, *41*, 1015–1021.

[147] Cheng, X.; Xu, H.; Wang, Z.; Zhu, K.; Li, G.; Jin, S. Synthesis, characterization and formation mechanism of metastable phase VO2(A) nanorods. *Mater. Res. Bull.* **2013**, *48*, 3383–3388.

[148] Corr, S. a.; Grossman, M.; Shi, Y.; Heier, K. R.; Stucky, G. D.; Seshadri, R. VO2(B) nanorods: solvothermal preparation, electrical properties, and conversion to rutile VO2 and V2O3. *J. Mater. Chem.* **2009**, *19*, 4362–7.

[149] Zhang, Y.; Huang, Y.; Zhang, J.; Wu, W.; Niu, F.; Zhong, Y.; Liu, X.; Liu, X.; Huang, C. Facile synthesis, phase transition, optical switching and oxidation resistance properties of belt-like VO2(A) and VO2(M) with a rectangular cross section. *Mater. Res. Bull.* **2012**, *47*, 1978–1986.

[150] An, Q.; Wei, Q.; Mai, L.; Fei, J.; Xu, X.; Zhao, Y.; Yan, M.; Zhang, P.; Huang, S. Supercritically exfoliated ultrathin vanadium pentoxide nanosheets with high rate capability for lithium batteries. *Phys. Chem. Chem. Phys.* **2013**, *15*, 16828–33.

[151] Pang, H.; Dong, Y.; Ting, S. L.; Lu, J.; Li, C. M.; Kim, D.-H.; Chen, P. 2D single- or double-layered vanadium oxide nanosheet assembled 3D microflowers: controlled synthesis, growth mechanism, and applications. *Nanoscale* **2013**, *5*, 7790–4.

[152] Li, G.; Chao, K.; Zhang, C.; Zhang, Q.; Peng, H.; Chen, K. Synthesis of urchin-like VO2 nanostructures composed of radially aligned nanobelts and their disassembly. *Inorg. Chem.* **2009**, *48*, 1168–72.

[153] Pan, A.; Wu, H. B.; Yu, L.; Zhu, T.; Lou, X. W. D. Synthesis of hierarchical three-dimensional vanadium oxide microstructures as high-capacity cathode materials for lithium-ion batteries. *ACS Appl. Mater. Interfaces* **2012**, *4*, 3874–9.

[154] Xu, Y.; Zheng, L.; Wu, C.; Qi, F.; Xie, Y. New-phased metastable V(2) O(3) porous urchinlike micronanostructures: facile synthesis and application in aqueous lithium ion batteries. *Chemistry* **2011**, *17*, 384–91.

[155] EVA. 2004.

[156] Everse, J.; Johnson, M. C.; Marini, M. A. Peroxidase activities of hemoglobin and hemoglobin deriatives. *Methods Enzymol.* **1994**, *231*, 547–561.

[157] Ma, J.; Wu, Q.; Chen, Y. An oxides-hydrothermal approach from bulky V2O5 powder to V3O7 · H2O nanoribbons or V3O7 nanoflowers in various ethanol/water mixed solvent. *Mater. Res. Bull.* **2009**, *44*, 1142–1147.

[158] Li, G.; Liu, Y.; Liu, C. Solvothermal synthesis of gamma aluminas and their structural evolution. *Microporous Mesoporous Mater.* **2013**, *167*, 137–145.

[159] Garnweitner, G.; Niederberger, M. Nonaqueous and Surfactant-Free Synthesis Routes to Metal Oxide Nanoparticles. *J. Am. Ceram. Soc.* **2006**, *89*, 1801–1808.

[160] Xu, Y.; Han, X.; Zheng, L.; Wei, S.; Xie, Y. First investigation on charge-discharge reaction mechanism of aqueous lithium ion batteries: a new anode material of Ag2V4O11 nanobelts. *Dalt. Trans.* **2011**, *40*, 10751–10751.

[161] Kera, Y.; Hirota, K. Infrared Spectroscopic Study of Oxygen Species in Vanadium Pentoxide with Reference to Its Activity in Catalytic Oxidation. *J. Phys. Chem.* **1969**, *79*, 3973–3981.

[162] Nakamoto, K.; McCarthy, P. J.; Ruby, A.; Martell, A. E. Infrared Spectra of Metal Chelate Compounds. II Infrared Spectra of Acetylacetonates of Trivalent Metals. *J. Am. Chem. Soc.* **1952**, *83*, 1066–1069.

[163] Lee, S.-H.; Cheong, H. M.; Je Seong, M.; Liu, P.; Tracy, C. E.; Mascarenhas, A.; Pitts, J. R.; Deb, S. K. Microstructure study of amorphous vanadium oxide thin films using raman spectroscopy. *J. Appl. Phys.* **2002**, *92*, 1893–1897.

[164] Pradhan, M.; Roy, A.; Sinha, A. K.; Sahoo, R.; Deb, D.; Pal, T. Solid-state transformation of single precursor vanadium complex nanostructures to V 2 O 5 and VO 2 : catalytic activity of V 2 O 5 for oxidative coupling of 2-naphthol. *Dalt. Trans.* **2015**, *44*, 1889–1899.

[165] Mjejri, I.; Etteyeb, N.; Sediri, F. Hydrothermal synthesis of mesoporous rod-like nanocrystalline vanadium oxide hydrate V3O7 · H2O from hydroquinone and V2O5. *Mater. Res. Bull.* **2013**, *48*, 3335–3341.

[166] Frost, R. L.; Erickson, K. L.; Weier, M. L.; Carmody, O. Raman and infrared spectroscopy of selected vanadates. *Spectrochim. Acta, Part A* **2005**, *61A*, 829–834.

[167] Mendialdua, J.; Casanova, R.; Barbaux, Y. XPS studies of V205 , V6013 , VO 2 and V203. *J. Electron Spectros. Relat. Phenomena* **1995**, *71*, 249–261.

[168] Childs, B. R. E.; Bardsley, W. G. benzthiazoline-6-sulphonic acid) as Chromogen. *Biochem. J.* **1975**, *145*, 93–103.

[169] Susannab, L.; Chen, W.-j.; Jjakac, A.; Espenson, J. H. Spectroscopic Parameters, Electrode Potentials, Acid Ionization Constants and Electron Exchange Rates of the 2,2´-Azinobis(3-ethylbenzothiazoline-6-sulfonate) Radicals and Ions. *J. Phys. Chem.* **1993**, *97*, 6710–6714.

[170] Leidich, P. Synthesis of 1D Semiconductors for Application in Dye-Sensitized Solar Cells Dissertation. Ph.D. thesis, Johannes Gutenberg-Univerisität, 2014.

[171] Valenzuela, C. D.; Carriedo, G. a.; Valenzuela, M. L.; Zúñiga, L.; O'Dwyer, C. Solid state pathways to complex shape evolution and tunable porosity during metallic crystal growth. *Sci. Rep.* **2013**, *3*, 2642–2650.

[172] Guyton, D.; Hambrecht, F. Capacitor electrode stimulates nerve or muscle without oxidation-reduction reactions. *Science (80-.).* **1973**, *181*, 5–7.

[173] Chueh, Y.-L.; Chou, L.-J.; Wang, Z. L. SiO(2)/Ta(2)O(5) core-shell nanowires and nanotubes. *Angew. Chem. Int. Ed. Engl.* **2006**, *45*, 7773–8.

[174] Xu, L.; Guan, J.; Gao, L.; Sun, Z. Preparation of heterostructured mesoporous In2O3/Ta2O5 nanocomposites with enhanced photocatalytic activity for hydrogen evolution. *Catal. Commun.* **2011**, *12*, 548–552.

[175] Bouhafs, D.; Moussi, A.; Chikouche, A.; Ruiz, J. Design and simulation of antireflection coating systems for optoelectronic devices: Application to silicon solar cells. *Sol. Energy Mater. Sol. Cells* **1998**, *52*, 79–93.

[176] Britvin, S. N.; Siidra, O. I.; Lotnyk, A.; Krivovichev, S. V.; Depmeier, W. Niobate and Tantalate Pyrochlores: Soft Synthesis by the Fluoride Route. *Eur. J. Inorg. Chem.* **2010**, *2010*, 1082–1088.

[177] Baucke, F. G.; Dorner, S.; Heinzel, V.; Röth, G. Fuel Cell with solid Oxide Proton Conducting Electrolyte. *Mater. Sci. Forum* **1991**, *76*, 287–288.

[178] Lü, X.; Ding, S.; Lin, T.; Mou, X.; Hong, Z.; Huang, F. Ta2O5 nanowires: a novel synthetic method and their solar energy utilization. *Dalton Trans.* **2012**, *41*, 622–7.

[179] Duan, J.; Shi, W.; Xu, L.; Mou, G.; Xin, Q.; Guan, J. Hierarchical nanostructures of fluorinated and naked Ta2O5 single crystalline nanorods: hydrothermal preparation, formation mechanism and photocatalytic activity for H2 production. *Chem. Commun. (Camb).* **2012**, *48*, 7301–3.

[180] Su, Y.; Wang, S.; Meng, Y.; Han, H.; Wang, X. Dual substitutions of single dopant Cr3+ in perovskite NaTaO3: synthesis, structure, and photocatalytic performance. *RSC Adv.* **2012**, *2*, 12932–12939.

[181] Hashizume, T.; Saiki, a.; Terayama, K. Preparation of Pyrochlore Potassium Tantalate Thin Films on Ta/ITO Glass via Mild Hydrothermal Growth. *Mater. Trans.* **2010**, *51*, 261–264.

[182] Huang, L.; Chan, Q.; Zhang, B.; Wu, X.; Gao, P.; Jiao, Z.; Liu, Y. Preparation of Sodium Tantalate with Different tructures and Its Photocatalytic Activity for H2 Evolution from Water Splitting. *Chinese J. Catal.* **2011**, *32*, 1822–1830.

[183] Gao, R.; Zhou, S.; Li, W.; Chen, M.; Wu, L. Facile synthesis of uniform and well-defined single-crystal sodium tantalate cubes and their assembly into oriented two-dimensional nanofilm. *CrystEngComm* **2012**, *14*, 7031.

[184] Kanhere, P.; Tang, Y.; Zheng, J.; Chen, Z. Synthesis, photophysical properties, and photocatalytic applications of Bi doped NaTaO3 and Bi doped Na2Ta2O6 nanoparticles. *J. Phys. Chem. Solids* **2013**, *74*, 1708–1713.

[185] Buha, J.; Arčon, D.; Niederberger, M.; Djerdj, I. Solvothermal and surfactant-free synthesis of crystalline Nb(2)O(5), Ta(2)O(5), HfO(2), and Co-doped HfO(2) nanoparticles. *Phys. Chem. Chem. Phys.* **2010**, *12*, 15537–43.

[186] Wang, J.; Su, S.; Liu, B.; Cao, M.; Hu, C. One-pot, low-temperature synthesis of self-doped NaTaO3 nanoclusters for visible-light-driven photocatalysis. *Chem. Commun. (Camb).* **2013**, *49*, 7830–2.

[187] He, Y.; Zhu, Y. Solvothermal Synthesis of Sodium and Potassium Tantalate Perovskite Nanocubes. *Chem. Lett.* **2004**, *33*, 900–901.

[188] Kominami, H.; Miyakawa, M.; Murakami, S.-y.; Yasuda, T.; Kohno, M.; Onoue, S.-i.; Kera, Y.; Ohtani, B. Solvothermal synthesis of tantalum(V) oxide nanoparticles and their photocatalytic activities in aqueous suspension systems. *Phys. Chem. Chem. Phys.* **2001**, *3*, 2697–2703.

[189] Baruwati, B.; Varma, R. S. Synthesis of Monodispersed Tantalum(V) oxide Nanospheres by an Ethylene Glycol Mediated Route. *Cryst. Growth Des.* **2010**, *10*, 3424–3428.

[190] Vázquez-Cuchillo, O.; Manzo-Robledo, a.; Zanella, R.; Elizondo-Villareal, N.; Cruz-López, a. Characterization of NaTaO3 synthesized by ultrasonic method. *Ultrason. Sonochem.* **2013**, *20*, 498–501.

[191] Shanker, V.; Samal, S. L.; Pradhan, G. K.; Narayana, C.; Ganguli, A. K. Nanocrystalline NaNbO3 and NaTaO3: Rietveld studies, Raman spectroscopy and dielectric properties. *Solid State Sci.* **2009**, *11*, 562–569.

[192] Bonitatibus, P. J.; Torres, A. S.; Goddard, G. D.; FitzGerald, P. F.; Kulkarni, A. M. Synthesis, characterization, and computed tomography imaging of a tantalum oxide nanoparticle imaging agent. *Chem. Commun. (Camb).* **2010**, *46*, 8956–8.

[193] Yokoi, T.; Sakuma, J.; Maeda, K.; Domen, K.; Tatsumi, T.; Kondo, J. N. Preparation of a colloidal array of NaTaO3 nanoparticles via a confined space synthesis route and its photocatalytic application. *Phys. Chem. Chem. Phys.* **2011**, *13*, 2563–70.

[194] Lin, S.; Shi, L.; Yoshida, H.; Li, M.; Zou, X. Synthesis of hollow spherical tantalum oxide nanoparticles and their photocatalytic activity for hydrogen production. *J. Solid State Chem.* **2013**, *199*, 15–20.

[195] Kato, H.; Kudo, A. Water splitting into H2 and O2 on alkali tantalate photocatalysts ATaO3 (A= Li, Na, and K). *J. Phys. Chem. B* **2001**, *3*, 4285–4292.

[196] Kato, H.; Kudo, A. New tantalate photocatalysts for water decomposition into H 2 and O 2. *Chem. Phys. Lett.* **1998**, 487.

[197] Hu, C.-C.; Tsai, C.-C.; Teng, H. Structure Characterization and Tuning of Perovskite-Like NaTaO 3 for Applications in Photoluminescence and Photocatalysis. *J. Am. Ceram. Soc.* **2009**, *92*, 460–466.

[198] Kanhere, P.; Zheng, J.; Chen, Z. Visible light driven photocatalytic hydrogen evolution and photophysical properties of Bi3+ doped NaTaO3. *Int. J. Hydrogen Energy* **2012**, *37*, 4889–4896.

[199] Lee, S.; Teshima, K.; Mizuno, Y.; Yubuta, K.; Shishido, T.; Endo, M.; Oishi, S. Growth of well-developed sodium tantalate crystals from a sodium chloride flux. *CrystEngComm* **2010**, *12*, 2871–2877.

[200] Porob, D. G.; Maggard, P. a. Flux syntheses of La-doped NaTaO3 and its photocatalytic activity. *J. Solid State Chem.* **2006**, *179*, 1727–1732.

[201] Nelson, J. A.; Wagner, M. J. Synthesis of sodium tantalate nanorods by alkalide reduction. *J. Am. Chem. Soc.* **2003**, *125*, 332–3.

[202] Coehlo, A. TOPAS Academic. 2012.

[203] Cheary, R. W.; Coelho, a. A fundamental parameters approach to X-ray line-profile fitting. *J. Appl. Crystallogr.* **1992**, *25*, 109–121.

[204] Nalbandyan, V. B.; Belyaev, I. N.; Rykalova, S. I. Ion Exchange Reactions of Niobic Acid with the Pyrochlore Structure and the Structure of the Exchange Products. *Russ. J. Inorg. Chem.* **1984**, *29*, 996–998.

[205] Cademartiri, L.; Ozin, G. A. *Concepts of Nanochemistry*; Wiley-VCH: Weinheim, 2009.

[206] Schilmann, A.-m. Synthese und Biofunktionalisierung von SiO 2 -Nanopartikeln zur Anwendung in der Krebsimmuntherapie Dissertation. Ph.D. thesis, Johannes Gutenberg-Universität, 2014.

[207] Koll, D.; Andrusenko, I.; Mugnaioli, E.; Birkel, A.; Panthöfer, M.; Kolb, U.; Tremel, W. Snapshots of the Formation of NaTi 3 O 6 (OH) · 2H 2 O Nanowires: A Time-Resolved XRD/HRTEM Study. *Zeitschrift für Anorg. und Allg. Chemie* **2013**, *639*, 2521–2526.

[208] Birkel, A.; Loges, N.; Mugnaioli, E.; Branscheid, R.; Koll, D.; Frank, S.; Panthöfer, M.; Tremel, W. Interaction of alkaline metal cations with oxidic surfaces: effect on the morphology of SnO2 nanoparticles. *Langmuir* **2010**, *26*, 3590–5.

[209] Heiz, U., Landman, U., Eds. *Nanocatalysis*; Nanoscience and Technology; Springer Berlin Heidelberg: Berlin, Heidelberg, 2007.

[210] Corma, A.; Serna, P. Chemoselective hydrogenation of nitro compounds with supported gold catalysts. *Science* **2006**, *313*, 332–4.

[211] Durand, J.; Teuma, E.; Gómez, M. An overview of palladium nanocatalysts: Surface and molecular reactivity. *Eur. J. Inorg. Chem.* **2008**, 3577–3586.

[212] Joo, S. H.; Park, J. Y.; Tsung, C.-K.; Yamada, Y.; Yang, P.; Somorjai, G. a. Thermally stable Pt/mesoporous silica core-shell nanocatalysts for high-temperature reactions. *Nat. Mater.* **2009**, *8*, 126–131.

[213] Tauster, S. Strong metal-support interactions. *Acc. Chem. Res.* **1987**, 389–394.

[214] Tauster, S. J.; Fung, S. C.; Garten, R. L. Strong Metal-Support Interactions . Group 8 Noble Metals Supported on Ti02. *J. Am. Soc.* **1978**, *100*, 170–175.

[215] Gross, E.; Somorjai, G. a. The Impact of Electronic Charge on Catalytic Reactivity and Selectivity of Metal-Oxide Supported Metallic Nanoparticles. *Top. Catal.* **2013**, *56*, 1049–1058.

[216] Liu, J.; Zou, S.; Li, S.; Liao, X.; Hong, Y.; Xiao, L.; Fan, J. A general synthesis of mesoporous metal oxides with well-dispersed metal nanoparticles via a versatile sol–gel process. *J. Mater. Chem. A* **2013**, *1*, 4038–4047.

[217] Tao, C.; Xu, L.; Guan, J. Well-dispersed mesoporous Ta2O5 submicrospheres: Enhanced photocatalytic activity by tuning heating rate at calcination. *Chem. Eng. J.* **2013**, *229*, 371–377.

[218] Sreethawong, T.; Ngamsinlapasathian, S.; Suzuki, Y.; Yoshikawa, S. Nanocrystalline mesoporous Ta2O5-based photocatalysts prepared by surfactant-assisted templating sol–gel process for photocatalytic H2 evolution. *J. Mol. Catal. A Chem.* **2005**, *235*, 1–11.

[219] Poyraz, A. S.; Kuo, C.-H.; Kim, E.; Meng, Y.; Seraji, M. S.; Suib, S. L. Tungsten-Promoted Mesoporous Group 4 (Ti, Zr, and Hf) Transition-Metal Oxides for Room-Temperature Solvent-Free Acetalization and Ketalization Reactions. *Chem. Mater.* **2014**, *26*, 2803–2813.

[220] An, K.; Alayoglu, S.; Musselwhite, N.; Na, K.; Somorjai, G. a. Designed catalysts from Pt nanoparticles supported on macroporous oxides for selective isomerization of n-hexane. *J. Am. Chem. Soc.* **2014**, *136*, 6830–3.

[221] Boettcher, S. W.; Fan, J.; Tsung, C.-K.; Shi, Q.; Stucky, G. D. Harnessing the sol-gel process for the assembly of non-silicate mesostructured oxide materials. *Acc. Chem. Res.* **2007**, *40*, 784–92.

[222] Kondo, J. N.; Domen, K. Crystallization of Mesoporous Metal Oxides. *Chem. Mater.* **2008**, *20*, 835–847.

[223] Kondo, J.; Takahara, Y.; Lee, B.; Lu, D.; Domen, K. Synthesis and property of mesoporous tantalum oxides. *Top. Catal.* **2002**, *19*, 171–177.

[224] Tagusagawa, C.; Takagaki, A.; Iguchi, A.; Takanabe, K.; Kondo, J. N.; Ebitani, K.; Tatsumi, T.; Domen, K. Synthesis and Characterization of Mesoporous TaW Oxides as Strong Solid Acid Catalysts. *Chem. Mater.* **2010**, *22*, 3072–3078.

[225] Sreethawong, T.; Ngamsinlapasathian, S.; Yoshikawa, S. Facile surfactant-aided sol–gel synthesis of mesoporous-assembled Ta2O5 nanoparticles with enhanced photocatalytic H2 production. *J. Mol. Catal. A Chem.* **2013**, *374-375*, 94–101.

[226] Guo, G.; Huang, J. Preparation of mesoporous tantalum oxide and its enhanced photocatalytic activity. *Mater. Lett.* **2011**, *65*, 64–66.

[227] Guo, L.; Hagiwara, H.; Ida, S.; Daio, T.; Ishihara, T. One-pot soft-templating method to synthesize crystalline mesoporous tantalum oxide and its photocatalytic activity for overall water splitting. *ACS Appl. Mater. Interfaces* **2013**, *5*, 11080–6.

[228] Li, Z.; Liu, J.; Li, J.; Shen, J. Template free synthesis of crystallized nanoporous F-Ta2O5 spheres for effective photocatalytic hydrogen production. *Nanoscale* **2012**, *4*, 3867–70.

[229] Takahara, Y.; Kondo, J. N.; Takata, T.; Lu, D.; Domen, K. Mesoporous Tantalum Oxide. 1. Characterization and Photocatalytic Activity for the Overall Water Decomposition. *Chem. Mater.* **2001**, *13*, 1194–1199.

[230] Zhou, C.; Shang, L.; Yu, H.; Bian, T.; Wu, L.-Z.; Tung, C.-H.; Zhang, T. Mesoporous plasmonic Au-loaded Ta2O5 nanocomposites for efficient visible light photocatalysis. *Catal. Today* **2014**, *225*, 158–163.

[231] Huo, Q.; Margolese, D.; Feng, P.; Gier, T.; Sieger, P.; Leon, R.; Petroff, P. M.; Schüth, F.; Stucky, G. D. Generalized syntheses of periodic surfactant/inorganic composite materials. *Nature* **1994**, *368*, 371.

[232] Jin, Z.; Xiao, M.; Bao, Z.; Wang, P.; Wang, J. A general approach to mesoporous metal oxide microspheres loaded with noble metal nanoparticles. *Angew. Chem. Int. Ed. Engl.* **2012**, *51*, 6406–10.

[233] Jin, Z.; Wang, F.; Wang, J. J.; Yu, J. C. Metal Nanocrystal-Embedded Hollow Mesoporous TiO 2 and ZrO 2 Microspheres Prepared with Polystyrene Nanospheres as Carriers and Templates. *Adv. Funct. Mater.* **2013**, *23*, 2137–2144.

[234] Xie, Y.; Ding, K.; Liu, Z.; Tao, R.; Sun, Z.; Zhang, H.; An, G. In situ controllable loading of ultrafine noble metal particles on titania. *J. Am. Chem. Soc.* **2009**, *131*, 6648–9.

[235] Rioux, R. M.; Song, H.; Hoefelmeyer, J. D.; Yang, P.; Somorjai, G. a. High-surface-area catalyst design: Synthesis, characterization, and reaction studies of platinum nanoparticles in mesoporous SBA-15 silica. *J. Phys. Chem. B* **2005**, *109*, 2192–202.

[236] Munnik, P.; de Jongh, P. E.; de Jong, K. P. Recent Developments in the Synthesis of Supported Catalysts. *Chem. Rev.* **2015**, *115*, 6687–6718.

[237] Lee, E.; Chen, J.; Yin, Y.; Campbell, C.; Xia, Y. Pd-Catalyzed Growth of Pt Nanoparticles or Nanowires as Dense Coatings on Polymeric and Ceramic Particulate Supports. *Adv. Mater.* **2006**, *18*, 3271–3274.

[238] Nilsson, E.; Sakamoto, Y.; Palmqvist, A. E. Low-Temperature Synthesis and HRTEM Analysis of Ordered Mesoporous Anatase with Tunable Crystallite Size and Pore Shape. *Chem. Mater.* **2011**, *23*, 2781–2785.

[239] Whitesides, G. M.; Grzybowski, B. Self-assembly at all scales. *Science* **2002**, *295*, 2418–21.

[240] Raveendran, P.; Eswaramoorthy, M.; Bindu, U.; Chatterjee, M.; Hakuta, Y.; Kawanami, H.; Mizukami, F. Template-free formation of meso-structured anatase TiO2 with spherical morphology. *J. Phys. Chem. C* **2008**, *112*, 20007–20011.

[241] Thommes, M. Aspekte der Charakterisierung mesoporöser Materialien durch Gasadsorption.

[242] Poyraz, A. S.; Kuo, C.-H.; Biswas, S.; King'ondu, C. K.; Suib, S. L. A general approach to crystalline and monomodal pore size mesoporous materials. *Nat. Commun.* **2013**, *4*, 2952.

[243] Sreethawong, T.; Ngamsinlapasathian, S.; Lim, S. H.; Yoshikawa, S. Investigation of thermal treatment effect on physicochemical and photocatalytic H2 produc-

tion properties of mesoporous-assembled Nb2O5 nanoparticles synthesized via a surfactant-modified sol–gel method. *Chem. Eng. J.* **2013**, *215-216*, 322–330.

[244] Robben, L.; Ismail, A. A.; Lohmeier, S. J.; Feldhoff, A.; Bahnemann, D. W.; Buhl, J.-C. Facile Synthesis of Highly Ordered Mesoporous and Well Crystalline TiO 2 : Impact of Different Gas Atmosphere and Calcination Temperatures on Structural Properties. *Chem. Mater.* **2012**, *24*, 1268–1275.

[245] Sahoo, J. K.; Tahir, M. N.; Yella, A.; Schladt, T. D.; Pfeiffer, S.; Nakhjavan, B.; Mugnaioli, E.; Kolb, U.; Tremel, W. From Single Molecules to Nanoscopically Structured Materials: Self-Assembly of Metal Chalcogenide/Metal Oxide Nanostructures Based on the Degree of Pearson Hardness. *Chem. Mater.* **2011**, *23*, 3534–3539.

[246] Dong, W.; Li, Y.; Niu, D.; Ma, Z.; Liu, X.; Gu, J.; Zhao, W.; Zheng, Y.; Shi, J. A simple route to prepare monodisperse Au NP-decorated, dye-doped, superparamagnetic nanocomposites for optical, MR, and CT trimodal imaging. *Small* **2013**, *9*, 2500–8.

[247] Kim, J.; Lee, J. E.; Lee, J.; Jang, Y.; Kim, S.-W.; An, K.; Yu, J. H.; Hyeon, T. Generalized fabrication of multifunctional nanoparticle assemblies on silica spheres. *Angew. Chem. Int. Ed. Engl.* **2006**, *45*, 4789–93.

[248] Liz-Marzán, L. M.; Mulvaney, P. The Assembly of Coated Nanocrystals. *J. Phys. Chem. B* **2003**, *107*, 7312–7326.

[249] Agrawal, M.; Pich, A.; Gupta, S.; Zafeiropoulos, N. E.; Simon, P.; Stamm, M. Synthesis of novel tantalum oxide sub-micrometer hollow spheres with tailored shell thickness. *Langmuir* **2008**, *24*, 1013–8.

[250] Kondo, J.; Lu, L.; Takahara, Y. IR Characterization of Mesoporous Tantalum Oxide, Ta-TMS-1. *Bull. Chem. Soc. Jpn.* **2000**, *73*, 1123–1129.

[251] Cauda, V.; Schlossbauer, A.; Kecht, J.; Zürner, A.; Bein, T. Multiple core-shell functionalized colloidal mesoporous silica nanoparticles. *J. Am. Chem. Soc.* **2009**, *131*, 11361–11370.

[252] Wani, A.; Muthuswamy, E.; Savithra, G. H. L.; Mao, G.; Brock, S.; Oupicky, D. Surface functionalization of mesoporous silica nanoparticles controls loading and release behavior of mitoxantrone. *Pharm. Res.* **2012**, *29*, 2407–18.

[253] Tao, A. R.; Habas, S.; Yang, P. Shape Control of Colloidal Metal Nanocrystals. *Small* **2008**, *4*, 310–325.

[254] Tu, H.-L.; Lin, Y.-S.; Lin, H.-Y.; Hung, Y.; Lo, L.-W.; Chen, Y.-F.; Mou, C.-Y. In vitro Studies of Functionalized Mesoporous Silica Nanoparticles for Photodynamic Therapy. *Adv. Mater.* **2009**, *21*, 172–177.

[255] Pârvulescu, V. I.; Pârvulescu, V.; Endruschat, U.; Granger, P.; Richards, R. Mesoporous Pt-SiO2 and Pt-SiO2-Ta2O5 catalysts prepared using Pt colloids as templates. *Chemphyschem* **2007**, *8*, 666–78.

[256] Lee, J. E.; Lee, N.; Kim, H.; Kim, J.; Choi, S. H.; Kim, J. H.; Kim, T.; Song, I. C.; Park, S. P.; Moon, W. K.; Hyeon, T. Uniform mesoporous dye-doped silica nanoparticles decorated with multiple magnetite nanocrystals for simultaneous enhanced magnetic resonance imaging, fluorescence imaging, and drug delivery. *J. Am. Chem. Soc.* **2010**, *132*, 552–7.

[257] Ahrens, E. T.; Bulte, J. W. M. Tracking immune cells in vivo using magnetic resonance imaging. *Nat. Rev. Immunol.* **2013**, *13*, 755–63.

[258] Shin, T.-H.; Choi, Y.; Kim, S.; Cheon, J. Recent advances in magnetic nanoparticle-based multi-modal imaging. *Chem. Soc. Rev.* **2015**, *43*, 8098–8113.

[259] Schick, I. Design of Multifunctional Janus Particles for Biomedical Applications. Ph.D. thesis, Johannes Gutenberg-Universität, 2014.

[260] Le Trequesser, Q.; Seznec, H.; Delville, M.-H. Functionalized nanomaterials: their use as contrast agents in bioimaging: mono- and multimodal approaches. *Nanotechnol. Rev.* **2013**, *2*, 125–169.

[261] Willmann, J. K.; van Bruggen, N.; Dinkelborg, L. M.; Gambhir, S. S. Molecular imaging in drug development. *Nat. Rev. Drug Discov.* **2008**, *7*, 591–607.

[262] Lee, D.-E.; Koo, H.; Sun, I.-C.; Ryu, J. H.; Kim, K.; Kwon, I. C. Multifunctional nanoparticles for multimodal imaging and theragnosis. *Chem. Soc. Rev.* **2012**, *41*, 2656–72.

[263] Mout, R.; Moyano, D. F.; Rana, S.; Rotello, V. M. Surface functionalization of nanoparticles for nanomedicine. *Chem. Soc. Rev.* **2012**, *41*, 2539–44.

[264] Xing, H.; Bu, W.; Zhang, S.; Zheng, X.; Li, M.; Chen, F.; He, Q.; Zhou, L.; Peng, W.; Hua, Y.; Shi, J. Multifunctional nanoprobes for upconversion fluorescence, MR and CT trimodal imaging. *Biomaterials* **2012**, *33*, 1079–89.

[265] Lee, N.; Choi, S. H.; Hyeon, T. Nano-sized CT contrast agents. *Adv. Mater.* **2013**, *25*, 2641–60.

[266] Yu, S. B.; Watson, a. D. Metal-Based X-ray Contrast Media. *Chem. Rev.* **1999**, *99*, 2353–78.

[267] Krause, W. Delivery of diagnostic agents in computed tomography. *Adv. Drug Deliv. Rev.* **1999**, *37*, 159–173.

[268] De La Vega, J. C.; Häfeli, U. O. Utilization of nanoparticles as X-ray contrast agents for diagnostic imaging applications. *Contrast Media Mol. Imaging* **2015**, *10*, 81–95.

[269] Kim, D.; Park, S.; Lee, J. H.; Jeong, Y. Y.; Jon, S. Antibiofouling polymer-coated gold nanoparticles as a contrast agent for in vivo X-ray computed tomography imaging. *J. Am. Chem. Soc.* **2007**, *129*, 7661–7665.

[270] Popovtzer, R.; Agrawal, A.; Kotov, N. a.; Popovtzer, A.; Balter, J.; Carey, T. E.; Kopelman, R. Targeted gold nanoparticles enable molecular CT imaging of cancer. *Nano Lett.* **2008**, *8*, 4593–4596.

[271] Liu, Y.; Ai, K.; Liu, J.; Yuan, Q.; He, Y.; Lu, L. A high-performance ytterbium-based nanoparticulate contrast agent for in vivo X-ray computed tomography imaging. *Angew. Chem. Int. Ed. Engl.* **2012**, *51*, 1437–42.

[272] Liu, J.; Zheng, X.; Yan, L.; Zhou, L.; Tian, G.; Yin, W.; Wang, L.; Liu, Y.; Hu, Z.; Gu, Z.; Chen, C.; Zhao, Y. Bismuth Sulfide Nanorods as a Precision Nanomedicine for in Vivo Multimodal Imaging-Guided Photothermal Therapy of Tumor. *ACS Nano* **2015**, *9*, 696–707.

[273] Rabin, O.; Manuel Perez, J.; Grimm, J.; Wojtkiewicz, G.; Weissleder, R. An X-ray computed tomography imaging agent based on long-circulating bismuth sulphide nanoparticles. *Nat. Mater.* **2006**, *5*, 118–122.

[274] Kinsella, J. M.; Jimenez, R. E.; Karmali, P. P.; Rush, A. M.; Kotamraju, V. R.; Gianneschi, N. C.; Ruoslahti, E.; Stupack, D.; Sailor, M. J. X-ray computed

tomography imaging of breast cancer by using targeted peptide-labeled bismuth sulfide nanoparticles. *Angew. Chem. Int. Ed. Engl.* **2011**, *50*, 12308–12311.

[275] Freedman, J. D.; Lusic, H.; Snyder, B. D.; Grinstaff, M. W. Tantalum Oxide Nanoparticles for the Imaging of Articular Cartilage Using X-Ray Computed Tomography: Visualization of Ex Vivo/In Vivo Murine Tibia and Ex Vivo Human Index Finger Cartilage. *Angew. Chem. Int. Ed. Engl.* **2014**, 1–6.

[276] Torres, A. S.; Bonitatibus, P. J.; Colborn, R. E.; Goddard, G. D.; FitzGerald, P. F.; Lee, B. D.; Marino, M. E. Biological performance of a size-fractionated core-shell tantalum oxide nanoparticle x-ray contrast agent. *Invest. Radiol.* **2012**, *47*, 578–87.

[277] Bonitatibus, P. J.; Torres, A. S.; Kandapallil, B.; Lee, B. D.; Goddard, G. D.; Colborn, R. E.; Marino, M. E. Preclinical assessment of a zwitterionic tantalum oxide nanoparticle X-ray contrast agent. *ACS Nano* **2012**, *6*, 6650665–8.

[278] Lee, N.; Cho, H. R.; Oh, M. H.; Lee, S. H.; Kim, K.; Kim, B. H.; Shin, K.; Ahn, T.-y.; Choi, J. W.; Kim, Y.-w.; Choi, S. H.; Hyeon, T. Multifunctional Fe3 O4 /TaOx Core/Shell Nanoparticles for Simultaneous Magnetic Resonance Imaging and X-Ray Computer Tomography. *J. Am. Chem. Soc.* **2012**, *134*, 10309–10312.

[279] Jun, Y. W.; Seo, J. W.; Cheon, J. Nanoscaling laws of magnetic nanoparticles and their applicabilities in biomedical sciences. *Acc. Chem. Res.* **2008**, *41*, 179–189.

[280] Jun, Y.-W.; Huh, Y.-M.; Choi, J.-S.; Lee, J.-H.; Song, H.-T.; Kim, S.; Yoon, S.; Kim, K.-S.; Shin, J.-S.; Suh, J.-S.; Cheon, J. Nanoscale size effect of magnetic nanocrystals and their utilization for cancer diagnosis via magnetic resonance imaging. *J. Am. Chem. Soc.* **2005**, *127*, 5732–5733.

[281] Lee, J.-H.; Huh, Y.-M.; Jun, Y.-w.; Seo, J.-w.; Jang, J.-t.; Song, H.-T.; Kim, S.; Cho, E.-J.; Yoon, H.-G.; Suh, J.-S.; Cheon, J. Artificially engineered magnetic nanoparticles for ultra-sensitive molecular imaging. *Nat. Med.* **2007**, *13*, 95–99.

[282] Schladt, T. D. et al. Au@MnO nanoflowers: hybrid nanocomposites for selective dual functionalization and imaging. *Angew. Chem. Int. Ed. Engl.* **2010**, *49*, 3976–3980.

[283] Werner, E. J.; Datta, A.; Jocher, C. J.; Raymond, K. N. High-relaxivity MRI contrast agents: Where coordination chemistry meets medical imaging. *Angew. Chemie - Int. Ed.* **2008**, *47*, 8568–8580.

[284] Peters, J. a.; Djanashvili, K. Lanthanide Loaded Zeolites, Clays, and Mesoporous Silica Materials as MRI Probes. *Eur. J. Inorg. Chem.* **2012**, *2012*, 1961–1974.

[285] Boros, E.; Gale, E. M.; Caravan, P. MR imaging probes: design and applications. *Dalt. Trans.* **2015**, *44*, 4804–4818.

[286] Botta, M.; Tei, L. Relaxivity Enhancement in Macromolecular and Nanosized GdIII-Based MRI Contrast Agents. *Eur. J. Inorg. Chem.* **2012**, *2012*, 1945–1960.

[287] Maldiney, T.; Doan, B.-T.; Alloyeau, D.; Bessodes, M.; Scherman, D.; Richard, C. Gadolinium-Doped Persistent Nanophosphors as Versatile Tool for Multimodal In Vivo Imaging. *Adv. Funct. Mater.* **2015**, *25*, 331–338.

[288] Chai, W.; Wang, S.; Zhao, H.; Liu, G.; Fischer, K.; Li, H.; Wu, L.; Schmidt, M. Hybrid assemblies based on a gadolinium-containing polyoxometalate and a cationic polymer with spermine side chains for enhanced MRI contrast agents. *Chemistry* **2013**, *19*, 13317–21.

[289] Caravan, P.; Ellison, J. J.; McMurry, T. J.; Lauffer, R. B. Gadolinium(III) Chelates as MRI Contrast Agents: Structure, Dynamics, and Applications. *Chem. Rev.* **1999**, *99*, 2293–2352.

[290] Schladt, T. D.; Koll, K.; Prüfer, S.; Bauer, H.; Natalio, F.; Dumele, O.; Raidoo, R.; Weber, S.; Wolfrum, U.; Schreiber, L. M.; Radsak, M. P.; Schild, H.; Tremel, W. Multifunctional superparamagnetic MnO@SiO2 core/shell nanoparticles and their application for optical and magnetic resonance imaging. *J. Mater. Chem.* **2012**, *22*, 9253–9262.

[291] Buonsanti, R.; Milliron, D. J. Chemistry of Doped Colloidal Nanocrystals. *Chem. Mater.* **2013**, *25*, 1305–1317.

[292] Cheon, J.; Lee, J.-H. Synergistically integrated nanoparticles as multimodal probes for nanobiotechnology. *Acc. Chem. Res.* **2008**, *41*, 1630–40.

[293] Thanh, N. T.; a.W. Green, L. Functionalisation of nanoparticles for biomedical applications. *Nano Today* **2010**, *5*, 213–230.

[294] Karakoti, A. S.; Das, S.; Thevuthasan, S.; Seal, S. PEGylated inorganic nanoparticles. *Angew. Chem. Int. Ed. Engl.* **2011**, *50*, 1980–94.

[295] Stark, W. J. Nanopartikel in biologischen Systemen. *Angew. Chemie* **2011**, *123*, 1276–1293.

[296] Cauda, V.; Argyo, C.; Bein, T. Impact of different PEGylation patterns on the long-term bio-stability of colloidal mesoporous silica nanoparticles. *J. Mater. Chem.* **2010**, *20*, 8693–8699.

[297] Johnston, A. P.; Such, G. K.; Ng, S. L.; Caruso, F. Challenges facing colloidal delivery systems: From synthesis to the clinic. *Curr. Opin. Colloid Interface Sci.* **2011**, *16*, 171–181.

[298] Selvan, S. T.; Tan, T. T. Y.; Yi, D. K.; Jana, N. R. Functional and multifunctional nanoparticles for bioimaging and biosensing. *Langmuir* **2010**, *26*, 11631–41.

[299] Lee, J.-H.; Jun, Y.-W.; Yeon, S.-I.; Shin, J.-S.; Cheon, J. Dual-mode nanoparticle probes for high-performance magnetic resonance and fluorescence imaging of neuroblastoma. *Angew. Chem. Int. Ed. Engl.* **2006**, *45*, 8160–2.

[300] Debbage, P.; Jaschke, W. Molecular imaging with nanoparticles: giant roles for dwarf actors. *Histochem. Cell Biol.* **2008**, *130*, 845–75.

[301] Lux, F.; Roux, S.; Perriat, P.; Tillement, O. Biomedical Applications of Nanomaterials Containing Gadolinium. *Curr. Inorg. Chem.* **2011**, *1*, 117–129.

[302] Vallet-Regí, M.; Balas, F.; Arcos, D. Mesoporöse Materialien für den Wirkstofftransport. *Angew. Chemie* **2007**, *119*, 7692–7703.

[303] Sarparanta, M.; Bimbo, L. M.; Rytkönen, J.; Mäkilä, E.; Laaksonen, T. J.; Laaksonen, P.; Nyman, M.; Salonen, J.; Linder, M. B.; Hirvonen, J.; Santos, H. a.; Airaksinen, A. J. Intravenous delivery of hydrophobin-functionalized porous silicon nanoparticles: stability, plasma protein adsorption and biodistribution. *Mol. Pharm.* **2012**, *9*, 654–63.

[304] De Jong, W. H.; Borm, P. J. a. Drug delivery and nanoparticles:applications and hazards. *Int. J. Nanomedicine* **2008**, *3*, 133–49.

[305] Schäfer, J.; Sitterberg, J.; Ehrhardt, C.; Kumar, M. R.; Bakowsky, U. A New Drug Vehicle - Lipid Coated Biodegradable Nanoparticles. *Adv. Sci. Technol.* **2008**, *57*, 148–153.

[306] Tarn, D.; Ashley, C. E.; Xue, M.; Carnes, E. C.; Zink, J. I.; Brinker, C. J. Mesoporous silica nanoparticle nanocarriers: biofunctionality and biocompatibility. *Acc. Chem. Res.* **2013**, *46*, 792–801.

[307] Sapsford, K. E.; Algar, W. R.; Berti, L.; Gemmill, K. B.; Casey, B. J.; Oh, E.; Stewart, M. H.; Medintz, I. L. Functionalizing nanoparticles with biological molecules: developing chemistries that facilitate nanotechnology. *Chem. Rev.* **2013**, *113*, 1904–2074.

[308] Blum, A. P.; Kammeyer, J. K.; Rush, A. M.; Callmann, C. E.; Hahn, M. E.; Gianneschi, N. C. Stimuli-Responsive Nanomaterials for Biomedical Applications. *J. Am. Chem. Soc.* **2015**, *137*, 2140–2154.

[309] Arruebo, M. Drug delivery from structured porous inorganic materials. *Wiley Interdiscip. Rev. Nanomed. Nanobiotechnol.* **2012**, *4*, 16–30.

[310] Johnson, N. J. J.; Oakden, W.; Stanisz, G. J.; Prosser, R. S.; Veggel, F. C. J. M. V. Size-Tunable , Ultrasmall NaGdF 4 Nanoparticles : Insights into Their T 1 MRI Contrast Enhancement. *Chem. Mater.* **2011**, *23*, 3714–3722.

[311] Bridot, J.-L.; a. C. Faure,; Laurent, S.; Riviere, C.; Billotey, C.; Hiba, B.; Janier, M.; Josserand, V.; Coll, J.-L.; VanderElst, L.; Muller, R.; Roux, S.; Perriat, P.; Tillement, O. Hybrid Gd oxide nanoparticle multimodal contrast agents for in vivo imaging. *J. Am. Chem. Soc.* **2007**, *129*, 5076–5084.

[312] Sethi, R.; Ananta, J. S.; Karmonik, C.; Zhong, M.; Fung, S. H.; Liu, X.; Li, K.; Ferrari, M.; Wilson, L. J.; Decuzzi, P. Enhanced MRI relaxivity of Gd3+-based contrast agents geometrically confined within porous nanoconstructs. *Contrast Media Mol. Imaging* **2012**, *7*, 501–508.

[313] Aaron, A. J.; Bumb, A.; Brechbiel, M. W. Macromolecules, dendrimers, and nanomaterials in magnetic resonance imaging: The interplay between size, function, and pharmacokinetics. *Chem. Rev.* **2010**, *110*, 2921–2959.